A genetic screen identifies new steps in oocyte maturation that enhance proteostasis in the immortal germ lineage

Madhuja Samaddar*[,1], Jérôme Goudeau*[,1], Melissa Sanchez[2], David H. Hall[3], K. Adam Bohnert[1,#], Maria Ingaramo[1] and Cynthia Kenyon[1,†]

[1]Calico Life Sciences LLC, South San Francisco, CA 94080, USA.

[2]Department of Molecular and Cellular Biology, University of California, Berkeley, CA 94720, USA.

[3]Dominick P. Purpura Department of Neuroscience, Albert Einstein College of Medicine, New York, NY 01461, USA.

[#]Present address: Department of Biological Sciences, Louisiana State University, Baton Rouge, LA 70803, USA.

* These authors contributed equally

[†] Correspondence to: cynthia@calicolabs.com

Abstract

Somatic cells age and die, but the germ-cell lineage is immortal. In *C. elegans*, germline immortality involves proteostasis renewal at the beginning of each new generation, when oocyte-maturation signals from sperm trigger the clearance of carbonylated proteins and protein aggregates. Here, we explore the cell biology of this proteostasis renewal in the context of a whole-genome RNAi screen. Oocyte maturation signals are known to trigger protein-aggregate removal via lysosome acidification. Our findings suggest that lysosomes are acidified as a consequence of changes in ER activity that permit assembly of the lysosomal V-ATPase, which in turn allows lysosomes to clear the aggregates via microautophagy. We define two functions for mitochondria, both of which appear to be independent of ATP generation. Many genes from the screen also regulate lysosome acidification and age-dependent protein aggregation in the soma, suggesting a fundamental mechanistic link between proteostasis renewal in the germline and somatic longevity.

55 **Introduction**

56 The germ cells of an organism not only give rise to the rich diversity of somatic lineages, they
57 also generate new germ cells that, by seeding subsequent generations, confer species
58 immortality. This sequential rejuvenation of youthfulness is one of the most interesting mysteries
59 in biology. How is it achieved? Not surprisingly, a process so crucial to the survival of the
60 species involves multiple levels of quality control. At one level, an entire oocyte can be
61 eliminated via apoptosis; for example, following DNA damage (Hunter, 2017; Luo et al., 2010;
62 Qiao et al., 2018; Schumacher et al., 2001). Oocytes can also eliminate defective organelles or
63 age-related molecular damage. For example, in mice, mitochondria containing defective DNA
64 are eliminated during oogenesis (Fan et al., 2008), and in yeast, nuclear senescence factors
65 and protein aggregates are extruded during meiosis (King et al., 2019; Ünal et al., 2011).
66 Mechanisms likely exist to counteract protein aggregation in *Drosophila* as well: relative to the
67 soma, the eggs of *Drosophila* exhibit enhanced proteasome activity and resistance to protein
68 aggregation (Fredriksson et al., 2012). Autophagy, a process known to eliminate damaged
69 organelles and macromolecules, may play a role as well, as it is required for the survival of the
70 mouse germ lineage (Gawriluk et al., 2011).
71 The nematode *C. elegans* is a valuable organism for studies of germline quality control. The
72 animal is transparent and genetically accessible, allowing one to analyze the effects of
73 perturbations over time in living animals using fluorescent reporters. *C. elegans* is a
74 hermaphrodite, producing both sperm and oocytes in each of two symmetrical gonadal arms.
75 Germ cells originate in stem-cell niches located at the distal ends of each arm and pass through
76 successive stages of meiosis as they move proximally towards the spermatheca, where
77 fertilization occurs (Crittenden et al., 1994; Hubbard and Greenstein, 2005; McCarter et al.,
78 1999). (Figure 1A). In 2010, Goudeau and Aguilaniu discovered that carbonylated proteins,
79 known to accumulate during aging, are present throughout the distal germline, but are
80 eliminated in proximal oocytes (Goudeau and Aguilaniu, 2010). Mutant worms that lack sperm

81 and develop as females retain carbonylated proteins throughout the entire germline, indicating
82 that sperm play a role in their elimination. In addition to carbonylated proteins, protein
83 aggregates also accumulate in the proximal oocytes of females but not in those of
84 hermaphrodites (Bohnert and Kenyon, 2017). Signals from sperm trigger the elimination of
85 protein aggregates in a process that is coupled to the broader choreography of oocyte
86 maturation, which involves dramatic changes in organelle morphology and function (Bluemink et
87 al., 1983; Carroll et al., 1996; Charbonneau and Grey, 1984; FitzHarris et al., 2007; Kobayashi
88 et al., 1991; Maller et al., 1977; Mehlmann et al., 1995; Wasserman et al., 1982; Yamashita,
89 2018). In *C. elegans,* oocyte maturation is triggered by actin-like major sperm proteins (MSPs)
90 released from sperm (Kosinki et al., 2005; Miller et al., 2003, 2001), and involves changes in
91 chromosome and nuclear dynamics linked to progression through meiosis, up-regulation of
92 translation, and changes in ER, lysosomal and mitochondrial function (Bohnert and Kenyon,
93 2017; Huelgas-Morales and Greenstein, 2018; Langerak et al., 2019). The shift in lysosomal
94 physiology that occurs during oocyte maturation is crucial for aggregate removal: the sperm-
95 derived signals trigger the acidification of lysosomes, which in turn engulf the aggregates by a
96 process that resembles microautophagy morphologically (Bohnert and Kenyon, 2017).
97 Lysosomal acidification also triggers a conversion in mitochondrial dynamics from what appears
98 to be a poised state, characterized by a high membrane potential, to an active state, in which
99 the potential is reduced. Conditions that prevent this mitochondrial membrane-potential shift,
100 such as inactivation of mitochondrial ATP synthase, prevent aggregate removal. However, how
101 lysosomes become acidified in response to sperm signals, how mitochondria contribute to
102 aggregate removal, and whether other organelles also play a role in aggregate clearance are
103 important outstanding questions.
104 To better understand mechanisms of proteostasis enhancement in the *C. elegans* germ
105 lineage, we combined cell biological approaches with a confocal-microscopy based genome-
106 wide RNAi screen for gene knockdowns that cause protein aggregates to accumulate even in

107 the presence of sperm. Our findings deepen our understanding of many aspects of protein
108 aggregation and clearance within the germline. Specifically, we find that (i) protein aggregates
109 accumulate in young, newly formed oocytes in the absence of sperm—their formation is an
110 integral part of oocyte development, rather than a consequence of prolonged oocyte
111 quiescence; (ii) inhibiting processes required for changes in ER morphogenesis and function
112 during oocyte maturation, including protein synthesis and actin dynamics, prevents lysosome
113 acidification by preventing the assembly of the V-ATPase lysosomal proton pump; (iii)
114 mitochondria elaborate an energy-independent checkpoint that gates protein-aggregate
115 removal; (iv) ESCRT vesicle-transport proteins are required for aggregate removal, consistent
116 with protein aggregates being removed via microautophagy; and, unexpectedly (v) as with
117 proteasome inhibition, inhibiting TRiC-complex chaperonins or HSP70 chaperones promotes
118 protein aggregation indirectly, by acting upstream in the pathway to block lysosome
119 acidification. Finally, we show that inhibiting lysosomal V-ATPase, vesicle-transport or
120 proteasome function also accelerates age-dependent protein aggregation in the soma, thus
121 bridging mechanisms that enhance proteostasis in the immortal germ lineage to those that
122 maintain proteostasis in the aging soma.
123
124
125
126
127
128
129
130
131

Results

A genome-wide RNAi screen identifies 84 genes that influence oocyte protein aggregation.

To undertake an unbiased genome-wide RNAi screen for components of the germline proteostasis network, we utilized the Ahringer RNAi feeding library (Kamath et al., 2003), which targets ~87% of annotated *C. elegans* genes, to identify gene inhibitions that cause proteins to aggregate even in the presence of sperm; that is, in hermaphrodites. A germline-specific GFP::RHO-1 translational fusion was selected as the reporter for the screen, as it forms dense patchy aggregates in female oocytes (Bohnert and Kenyon, 2017) and in unfertilized oocytes of aging hermaphrodites, which deplete their stores of sperm (David et al., 2010). Oocytes are formed in young adults, so RNAi was initiated at the beginning of the last larval stage (L4) to reduce the chance of missing genes with essential roles during development (Figure 1B). The animals were examined manually by confocal microscopy on day 2 of adulthood for the presence of GFP::RHO-1 aggregates in proximal oocytes (Figure 1A, 1B and S1A). The primary screen identified 367 genes whose knockdown led to GFP::RHO-1 aggregation in at least 50% of the animals. To eliminate false positives, the candidates were subjected to three independent rounds of validation using a similar workflow, with at least two independent rounds from two experimentalists (Figure 1C). We note that false negatives could result from failure of an RNAi bacterial strain to grow adequately, from insufficient or excessive gene inhibition, or because of functional redundancy.

The resulting set of 88 genes represented diverse cellular processes (Table S1), with highly enriched gene ontology (GO) categories including translation, RNA processing and cytoskeletal organization (Figure S1C). In addition, ATP-hydrolysis-coupled proton transport and lysosome acidification were both highly enriched, in agreement with our previous findings (Bohnert and Kenyon, 2017). We sorted the candidates according to relative representation in major biological processes (Figure 1D), after discarding candidates with known roles in male gonad and germ cell development (*fkh-6, spe-15*), in regulation of our proteostasis marker RHO-1 (*cyk-*

158 *4*), or with potential off-target effects (*adr-1* and *dhs-5*) (Table S1). Protein synthesis and
159 degradation, RNA processing, protein folding, and lysosome acidification were strongly
160 represented biological processes, as were genes involved in cytoskeletal organization, including
161 four of the five *C. elegans* actin genes. Among organelle systems, multiple candidates were
162 associated with ER homeostasis (*hsp-4, spcs-1 and srpa-68*) and vesicle-mediated transport
163 (*copb-2, sec-24.1, sar-1, rab-11.1* and *E03H4.8*). We also identified genes that could not be
164 classified into any of the highly-enriched biological-process categories and were designated
165 'orphans' (Table S1 and Fig. 1D).
166 We subjected representative candidates from each group, as well as all the orphans, to an
167 orthogonal screening approach, this time utilizing a different aggregation reporter, a germline-
168 specific NMY-2::GFP fusion protein (Bohnert and Kenyon, 2017) that forms distinctive punctate
169 aggregates in the absence of sperm (Figure 1C and Table S1). Out of the 55 candidates tested,
170 53 RNAi knockdowns also caused NMY-2::GFP protein-aggregate accumulation (Figure S1B).
171 Thus, these genes are likely to have a general effect on protein-aggregate clearance rather than
172 a specific effect on GFP::RHO-1.
173
174 *Aggregates form in young proximal oocytes.*
175 We classified the RNAi phenotypes as strong, intermediate or subtle based on the
176 degree of GFP::RHO-1 aggregation (Table S1). Typically, the phenotypically strong
177 knockdowns led to sterility, whereas the subtle knockdowns generally did not, though some
178 reduced the brood size. In principle, one could imagine that aggregates accumulate in oocytes
179 from sterile hermaphrodites because oocytes that would normally undergo ovulation and pass
180 into the uterus do not, and instead simply "age in place". Likewise, aggregates could
181 accumulate in normal female oocytes because in the absence of sperm, they proceed much
182 more slowly through the spermatheca and into the uterus (McCarter et al., 1999). As a
183 consequence, proximal oocytes of females are technically older than those of age-matched

184 hermaphrodites (Kim et al., 2013). This oocyte-age discrepancy raises the question of whether
185 aggregates accumulate only during long-term oocyte quiescence, or whether they are present in
186 newly formed female oocytes. To address this question, we collected age-matched late L4
187 ('Christmas-tree' stage) females and hermaphrodites and followed the hermaphrodites until their
188 first oocytes were cellularized. We found that age-matched first-proximal oocytes of young
189 females often contained protein aggregates (Figure 1E and S4). Therefore, protein-aggregate
190 accumulation does not require prolonged oocyte quiescence; instead, it appears to be part of
191 the normal developmental sequence of oocytes that are not exposed to sperm.
192
193
194
195
196
197
198
199
200
201
202
203
204
205
206
207
208
209
210
211
212
213

Figure 1

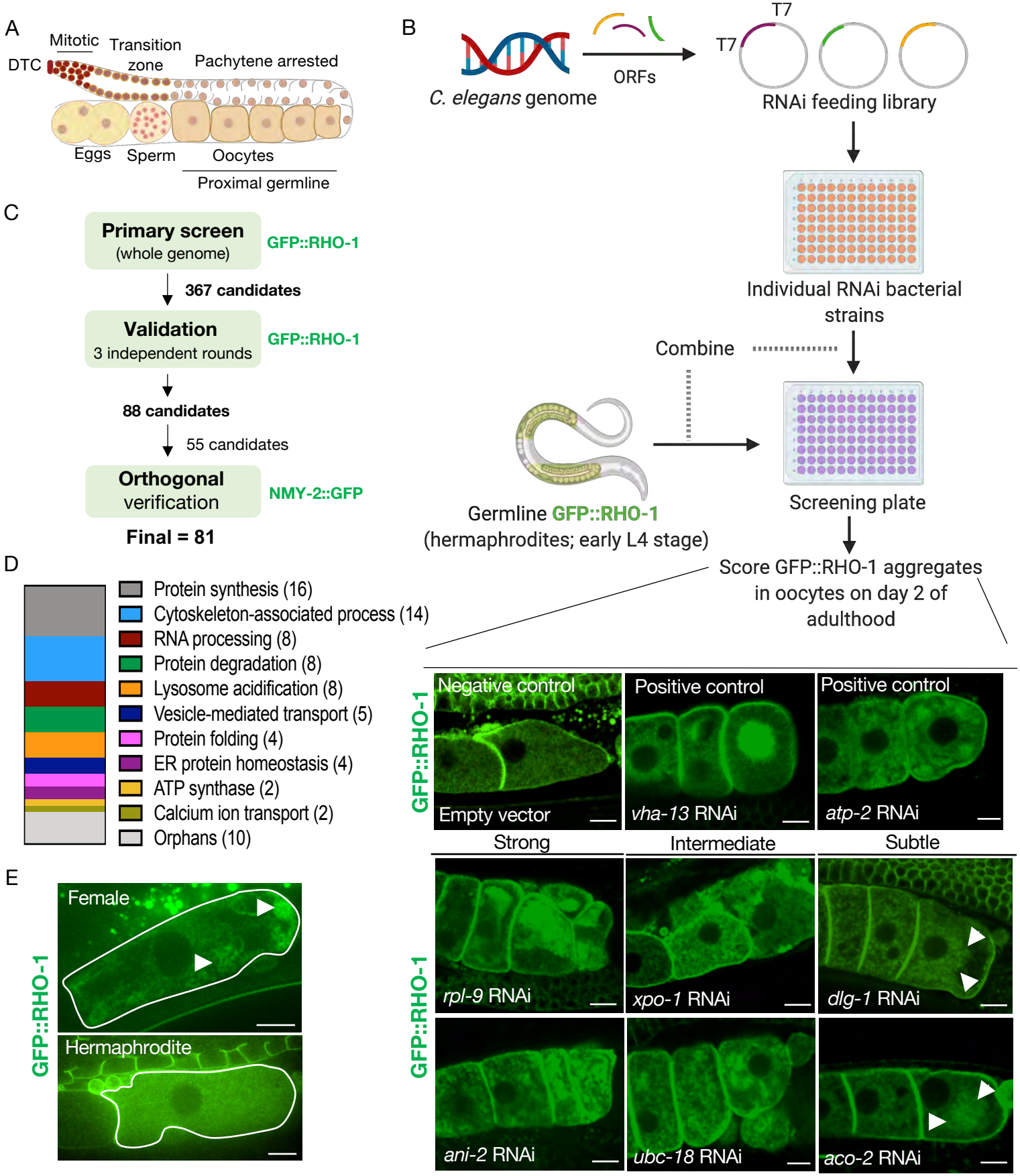
A
Mitotic
Transition zone
DTC
Pachytene arrested
Eggs
Sperm
Oocytes
Proximal germline
B
C. elegans genome
ORFs
T7
T7
RNAi feeding library
Individual RNAi bacterial strains
Combine
Germline GFP::RHO-1 (hermaphrodites; early L4 stage)
Screening plate
Score GFP::RHO-1 aggregates in oocytes on day 2 of adulthood
C
Primary screen (whole genome)
GFP::RHO-1
367 candidates
Validation 3 independent rounds
GFP::RHO-1
88 candidates
55 candidates
Orthogonal verification
NMY-2::GFP
Final = 81
D
Protein synthesis (16)
Cytoskeleton-associated process (14)
RNA processing (8)
Protein degradation (8)
Lysosome acidification (8)
Vesicle-mediated transport (5)
Protein folding (4)
ER protein homeostasis (4)
ATP synthase (2)
Calcium ion transport (2)
Orphans (10)
GFP::RHO-1
Negative control
Empty vector
Positive control
vha-13 RNAi
Positive control
atp-2 RNAi
Strong
Intermediate
Subtle
rpl-9 RNAi
xpo-1 RNAi
dlg-1 RNAi
ani-2 RNAi
ubc-18 RNAi
aco-2 RNAi
E
GFP::RHO-1
Female
Hermaphrodite

Figure 1. **Identification of genes that prevent protein aggregation in maturing *C. elegans* oocytes.** (A) Diagram of the *C. elegans* germline (B) Genome-wide RNAi-screen workflow. High resolution images from the validation rounds are represented here. Scale bars, 10 μm; white arrows, GFP::RHO-1 aggregates in subtle hits. (C) Schematic representing the procedure used for candidate validation and orthogonal verification using two independent germline-specific reporters. 45 candidates representing the major GO categories and all 10 orphans were subjected to orthogonal verification. (D) Common biological process GO categories enriched in the screen. Genes that were not members of these enriched categories were classified as orphans. (E) Very early oocytes of females and hermaphrodites (CF4557 and CF4552 strains, respectively). GFP::RHO-1 aggregates often appear in newly-formed female oocytes. Scale bars, 10 μm; white arrows, GFP::RHO-1 aggregates.

214 *The endoplasmic reticulum influences protein aggregation*

215 Many genes we identified were associated with the ER, so we explored ER biology in
216 more detail. The ER undergoes a major morphological rearrangement in response to oocyte
217 maturation signals (Langerak et al., 2019). We visualized the ER in *C. elegans* oocytes using a
218 germline-specific mCherry::SP12 reporter (Joseph-Strauss et al., 2012). SP12 is a signal-
219 peptidase subunit (Poteryaev et al., 2005) and *spcs-1*, which encodes SP12, was identified in
220 our screen. In hermaphrodite oocytes, the ER assumed a fine network appearance, whereas in
221 female oocytes, the ER formed bright, distinctive patches (Figure 2A, 2C and S2A). We also
222 examined ER morphology in the first, newly-formed female oocytes, using the L4 staging
223 procedure described above. Pristine female oocytes also exhibited ER patches, indicating that
224 the altered ER architecture is an intrinsic property of female oocytes and not a consequence of
225 prolonged quiescence (Figure 2B and S2B). The fluorescent signal from the female ER was
226 further enhanced as oocytes aged, possibly due to continued ER biogenesis coupled with
227 oocyte compression caused by their packing within the gonad (Figure S2A). Using two
228 fluorescent reporters, we visualized both the ER and GFP::RHO-1 simultaneously (Figure 2B,
229 S2C, S3 and S4), and found that in female oocytes, the ER and GFP::RHO-1 aggregates
230 segregated spatially into mutually-exclusive regions (Figure 2B, S2C and S4).
231 We also examined oocytes from young, age-matched hermaphrodites and females by
232 transmission electron microscopy (TEM). The ER in pristine oocytes from both sexes appeared
233 to be associated with ribosomes, indicative of active (or poised) protein synthesis, yet the
234 female ER was distinctively clustered into parallel stacks (Figure 2D and S5).
235 To test whether the stacked ER architecture of female oocytes could be reversed by sperm, we
236 visualized fluorescently-tagged ER and NMY-2::GFP aggregates simultaneously over time in
237 female oocytes after mating. The presence of sperm triggered distinctive remodeling of the ER
238 architecture and the clearance of aggregates, although with different kinetics (Figure 2E and
239 S6A). The earliest changes in the ER were detected approximately 10 minutes after mating, and

240 the morphology was significantly altered by 30 minutes (Figure 2E). In contrast, the clearance of
241 NMY-2 aggregates started a few minutes later, with aggregate clearance in the most proximal
242 oocytes typically occurring between 20 to 30 minutes after mating (Figure S6A, S6B and S7A).
243 Next, we investigated whether the genes identified in our RNAi screen might contribute to
244 proteostasis by influencing a process associated with ER architecture. To this end, we
245 subjected mCherry::SP12-germline-labeled hermaphrodites to 35 RNAi treatments representing
246 the various biological process categories as well as the individual orphans. This subset of RNAi
247 clones, which we termed the “assay pool”, was used for all subsequent large-scale phenotypic
248 analyses (Table 1). We visualized oocyte ER morphology in young adults subjected to the gene
249 knockdowns (Figure S7B and Table 1). Genes involved in cytoskeletal organization, protein
250 synthesis and protein folding were required for maintaining normal ER morphology and led to an
251 altered ER architecture when knocked down. Genes involved in RNA processing, protein
252 degradation and trafficking comprised a mixed class, with some knockdowns appearing to affect
253 ER morphology. We note that our analysis does not distinguish between genes with direct
254 effects on ER morphogenesis, like the actin cytoskeleton (Poteryaev et al., 2005), and genes
255 with indirect effects, like the proteasome, which is required for the degradation of GLD-1
256 (Bohnert and Kenyon, 2017; Goudeau et al., 2020; Spike et al., 2018), a translational repressor
257 involved in oocyte cell fate determination (Francis et al., 1995; Jones et al., 1996). Notably,
258 disrupting the mitochondrial ATP synthase, the V-ATPase complex or ER function itself did not
259 visibly alter the ER network, suggesting that these gene functions were not required for the
260 sperm-induced ER morphology change, or more generally for ER morphogenesis.
261
262
263
264
265

Figure 2

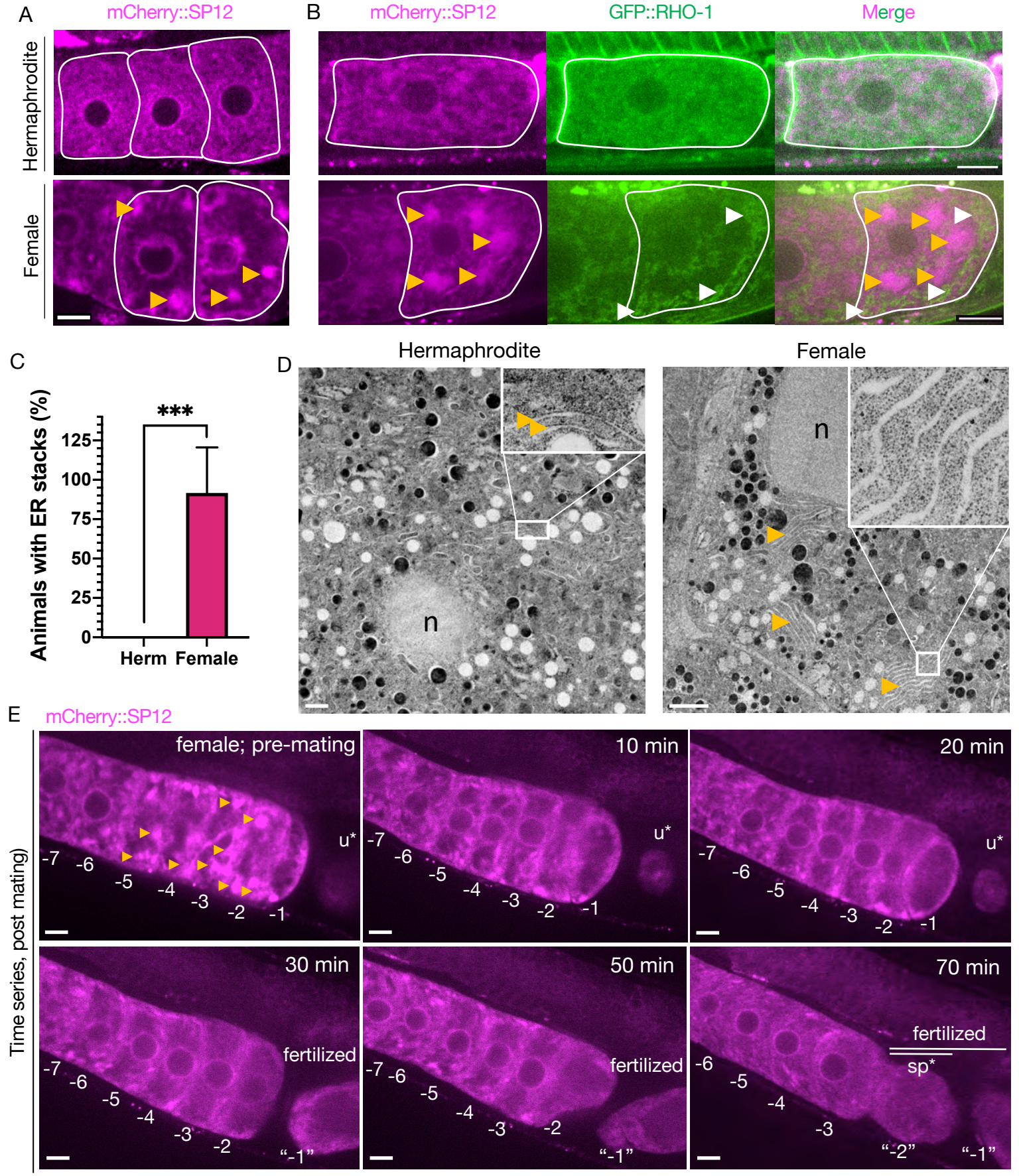
A
mCherry::SP12
Hermaphrodite
Female
B
mCherry::SP12
GFP::RHO-1
Merge
C
Animals with ER stacks (%)
***
125
100
75
50
25
0
Herm
Female
D
Hermaphrodite
Female
n
n
E
mCherry::SP12
Time series, post mating)
female; pre-mating
10 min
20 min
30 min
50 min
70 min
u*
-7
-6
-5
-4
-3
-2
-1
fertilized
"-1"
sp*
"-2"

Figure 2. ER morphology is regulated by sperm and correlates with protein aggregation.

(A) ER morphology in the germline of hermaphrodite (OCF15) and female (CF4542) animals, visualized using a mCherry::SP12 reporter. Orange arrows, ER patches. Scale bar, 10 μm. (B) GFP::RHO-1 localization in newly-formed oocytes from hermaphrodites (CF4552) and females (CF4557) also expressing mCherry::SP12. White arrows, GFP::RHO-1 aggregates. Scale bars, 10 μm. (C) Percentage of animals with ER patches in oocytes. n=12; mean +/- s.d., ***P $\leq$ 0.001 (Mann-Whitney test). (D)

Transmission electron micrographs from hermaphrodite (N2E) and female (CF4101) oocytes. At least 8 females and 8 hermaphrodites were subjected to TEM. Orange arrows, ER. Left panel, magnification 1,400X, scale bar, 1 μm; inset: magnification 13,000X, scale bar, 100 nm. Right panel, magnification 1,200X, scale bar, 2 μm; inset: magnification 18,500X, scale bar, 100 nm. (E) Reversal of ER patches (orange arrows) in female oocytes upon mating with CB1490 males. Female oocytes were imaged before and after mating at the indicated time points. Each oocyte is numbered according to its initial position relative to the spermatheca, and original numbers are maintained after fertilization. The figure shows a single representative animal, from 7 independent experiments. u*, unfertilized oocyte/debris in uterus in a different focal plane; sp*, an oocyte passing through spermatheca during fertilization. Scale bars, 10 μm.

Biological process	RNAi target	Gene code	Normal ER architecture	GFP::VHA-13 puncta	Lysosome acidification	Reduction in ΔΨ
Protein degradation	*pbs-7*	F39H11.5	No	No	No	No
	rpn-6.1	F57B9.10	Mixed	No	No	No
Protein synthesis (Translation)	*rps-20*	Y105E8A.16	No	No	No	No
	rpl-3	F13B10.2	No	No	No	No
Protein folding (Chaperones)	*cct-1*	T05C12.7	No	Reduced	No	No
	cct-5	C07G2.3	No	Reduced	No	No
Cytoskeleton-associated process	*act-1*	T04C12.6	No	No	No	No
	pat-3	ZK1058.2	No	No	No	No
	ani-2	K10B2.5	No	No	No	No
ER protein homeostasis	*hsp-4*	F43E2.8	Yes	No	No	No
	spcs-1	C34B2.10	Yes	No	No	No
	srpa-68	F55C5.8	Yes	No	No	No
Vesicle-mediated transport (Trafficking)	*copb-2*	F38E11.5	No	No	No	No
	sec-24.1	F12F6.6	Inconclusive	No	No	No
	sar-1	ZK180.4	Mixed	No	No	No
Lysosome acidification (V-ATPase)	*vha-13*	Y49A3A.2	Yes	No signal	No	No
	vha-12	F20B6.2	Yes	No	No	No
	vha-2	R10E11.2	Yes	No	No	No
ATP synthase	*atp-3*	F27C1.7	Yes	Yes	Yes	No
	atp-2	C34E10.6	Yes	Yes	Yes	No
RNA processing	*ess-2*	F42H10.7	No	Reduced	No	No
	cgh-1	C07H6.5	Mixed	No	No	No
	let-711	F57B9.2	Mixed	Reduced	No	No
Calcium ion transport	*itr-1*	F33D4.2	No	Reduced	No	No
	sca-1	K11D9.2	Yes	Reduced	No	No
Orphans	*kin-2*	R07E4.6	Mixed	No	No	No
	ttr-14	T05A10.3	Mixed	No	No	No
	par-5	M117.2	Yes	No	No	No
	xpo-1	ZK742.1	Yes	No	No	No
	srab-17	T11A5.2	Yes	Reduced	No	No
	rmd-2	C27H6.4	Yes	No	No	No
	dlg-1	C25F6.2a.1	No	No	No	No
	lgc-46	Y71D11A.5	Yes	Reduced	No	No
	aco-2	F54H12.1	Yes	No	No	No
	imb-1	F28B3.8	Inconclusive	No	No	No
ESCRT subunits*	*vps-20*	Y65B4A.3	Not tested	Yes	Yes	Not tested
	vps-28	Y87G2A.10	Not tested	Yes	Yes	Not tested
	vps-37	CD4.4	Not tested	Yes	Yes	Not tested
	vps-54	T21C9.2	Not tested	Yes	Yes	Not tested

Table 1. Functional gene categories from the proteostasis screen.

List of representative genes from each functional category that were selected for the assay pool and their effects on ER morphology, lysosome acidification, GFP::VHA-13 localization, and mitochondrial membrane potential. The ESCRT complex subunits (*) were not derived from the original screen but from subsequent candidate testing.

266 *Sperm signals initiate V-ATPase assembly, enabling lysosomal acidification*

267 Signals from sperm elicit the lysosomal acidification required for the clearance of protein
268 aggregates, and inhibiting the V-ATPase, which acidifies lysosomes, causes proteins to
269 aggregate in hermaphrodite oocytes (Bohnert and Kenyon, 2017). However, the mechanism by
270 which lysosome acidification occurs in response to signals from sperm is not known (Goudeau
271 et al., 2020; Spike et al., 2018). To address this question with minimal physiological disruption,
272 we first attempted to fluorescently tag endogenously-expressed V-ATPase subunits using
273 CRISPR/Cas9. We picked four different subunits, two from the membrane-embedded V_0 domain
274 (VHA-4 and VHA-7) and two from the peripheral V_1 domain (VHA-11 and VHA-13) (Table S2).
275 Unexpectedly, although each one of these tagged proteins was visible in somatic tissues, we
276 were unable to detect any fluorescence in the germline in either intact animals (Figure S8) or in
277 their dissected gonads (Figure S9A). Germline fluorescence was also undetectable when
278 imaging with a more sensitive wide-field system, or following photobleaching of the strong
279 intestinal signal, which we reasoned might mask a faint signal from the germline (data not
280 shown). Endogenous genes tagged with fluorescent proteins can be silenced in the germline by
281 the process of epigenetic RNAe (Shirayama et al., 2012); however, this explanation seems
282 unlikely since, unlike V-ATPase RNAi-treated animals, these animals produced viable embryos.
283 We also considered the possibility that these V-ATPase proteins did not act cell-autonomously
284 in the gonad, though V-ATPase mRNAs previously had been identified as direct targets of the
285 germline-specific GLD-1 translational regulator (Wright et al., 2011). To investigate cell
286 autonomy, we carried out tissue-specific RNAi experiments using sterility as a phenotypic
287 readout. Three hermaphrodite strains [wild-type, globally RNAi-defective *rde-1(mkc36)* mutants
288 DCL565, and germline-only RNAi-sensitive DCL569 animals (Zou et al., 2019)] were subjected
289 to RNAi from hatching (empty vector, *vha-12* and *vha-13*). Both wild-type and germline-RNAi-
290 permissive DCL569 animals exhibited sterility when fed *vha-12* and *vha-13* RNAi bacteria
291 (Figure S9B), whereas the whole-body RNAi-defective *rde-1* mutant did not. Thus, these V-

292 ATPase subunits are expressed and required in the germline, despite our inability to detect
293 them when tagged endogenously.
294 As a next-best approach for visualizing germline V-ATPase subunits, we obtained a Mos1-
295 mediated Single Copy Insertion (MosSCI) strain of GFP::VHA-13 driven by the germline-specific
296 *pie-1* promoter. This strain expressed GFP::VHA-13 in a genetically-stable fashion, though
297 presumably at elevated levels. In these animals, we observed a striking, sperm-dependent
298 pattern: GFP::VHA-13 formed distinct foci in hermaphrodite oocytes (Figure 3A and S10A) that
299 co-localized with foci of LysoTracker, a dye that stains acidic lysosomes (Figure 3B and S11A).
300 In contrast, the proximal oocytes of females exhibited diffuse GFP::VHA-13 fluorescent signal
301 (Figure 3A and S10B), with a slight enrichment in the perinuclear region. Female oocytes
302 demonstrated very weak LysoTracker staining (Bohnert and Kenyon, 2017), and there was no
303 significant overlap in the two signals (Figure 3B and S11B). To better control for effects of
304 overexpression, we lowered the level of GFP::VHA-13 expression by serially diluting *gfp* RNAi
305 bacteria. Even at the limit of fluorescence detection, hermaphrodites still exhibited GFP::VHA-13
306 foci, and females exhibited a diffuse distribution (Figure S9C). Thus, the germline harbors a
307 mechanism by which VHA-13 is localized to discrete, acidic cellular locations, indicative of
308 lysosomes, only in the presence of sperm. Notably, knocking down the *vha-12* gene, which
309 encodes another peripheral V-ATPase V_1-domain subunit, also prevented GFP::VHA-13 foci
310 formation in hermaphrodite oocytes (Figure S9D), suggesting a coordinated assembly pathway.
311 We asked whether sperm signals regulate V-ATPase localization in two ways. First, we
312 examined older, sperm-depleted hermaphrodites (day-5), and observed diffuse V-ATPase
313 localization, similar to that of females (Figure S10C). Second, we mated GFP::VHA-13-
314 expressing females with males and monitored their proximal oocytes. The diffuse fluorescent
315 signal began to change approximately 10 minutes after mating, organizing into distinct foci
316 within 20 to 30 minutes (Figure 3C and 3D). This change coincided with release from arrest and
317 oocyte maturation, ultimately leading to ovulation and fertilization. The time scales of ER

remodeling and GFP::VHA-13 relocalization (Figure 2E) were strikingly similar, suggesting a possible causal relationship. Together these findings suggest that sperm signals lead to lysosome acidification by initiating the recruitment of V-ATPase subunits to the surface of the lysosome and enabling proton-pump assembly.

Figure 3

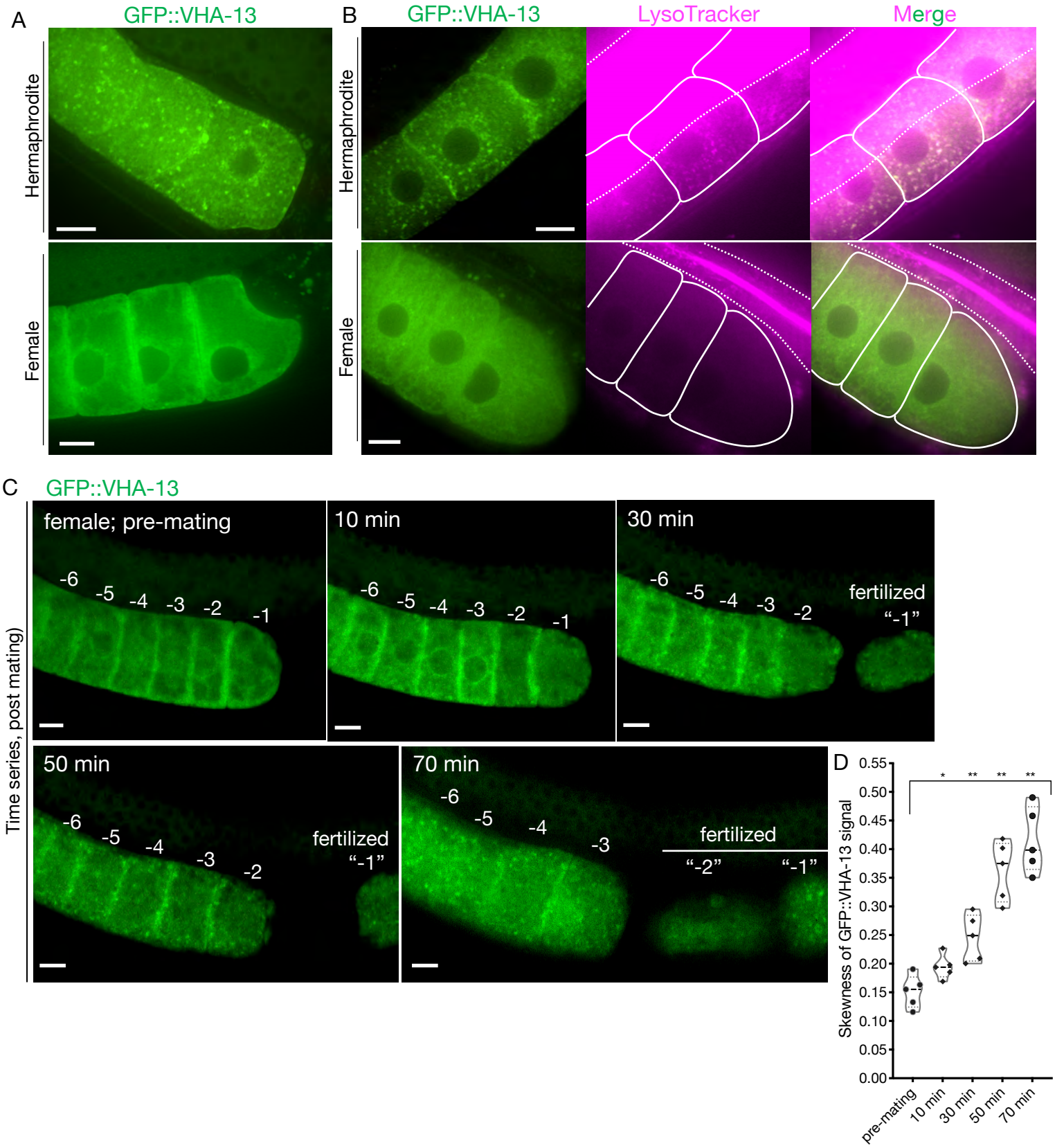
A
GFP::VHA-13
Hermaphrodite
Female
B
GFP::VHA-13
LysoTracker
Merge
Hermaphrodite
Female
C
GFP::VHA-13
Time series, post mating)
female; pre-mating
-6
-5
-4
-3
-2
-1
10 min
30 min
fertilized
"-1"
50 min
70 min
fertilized
"-2"
"-1"
D
Skewness of GFP::VHA-13 signal
0.55
0.50
0.45
0.40
0.35
0.30
0.25
0.20
0.15
0.10
0.05
0.00
*
**
**
**
pre-mating
10 min
30 min
50 min
70 min

Figure 3. Sperm-dependent lysosomal localization of VHA-13.

(A) Distribution of GFP::VHA-13 in proximal oocytes of hermaphrodites (PHX1414) and females (CF4599). (B) LysoTracker-stained oocytes from GFP::VHA-13-expressing hermaphrodites and females, for visualization of acidic lysosomes. The two signals colocalize in hermaphrodite oocytes. Dotted line; intestinal boundary, and solid line; oocytes. (C) Sperm signal-induced GFP::VHA-13 redistribution in female oocytes (CF4599). Oocytes were imaged before and after mating with CB1490 males. The GFP::VHA-13 signal shifts from diffuse to punctate following mating. Each oocyte is numbered according to its initial position relative to the spermatheca, and original numbers are maintained after fertilization. A representative individual is shown, from 5 independent mating experiments. (D) Increase in signal skewness (inhomogeneity) of GFP::VHA-13 as a function of time following mating. Mann-Whitney test was used to determine statistical significance; and *$P \leq 0.05$ and **$P \leq 0.01$. Scale bars, 10 μm (A-C).

351 *Most of the genes identified disrupt VHA-13 localization and lysosome acidification.*

352 To ask which gene inhibitions blocked lysosome acidification, we subjected
353 LysoTracker-stained hermaphrodites to knockdowns of the 'assay-pool' genes (Table 1). In wild-
354 type hermaphrodites, lysosomes are acidified only in proximal oocytes (Bohnert and Kenyon,
355 2017). Therefore, to internally control for variations in dye uptake, we analyzed the ratios of
356 staining intensities between proximal oocytes and distal germline regions. LysoTracker staining
357 of hermaphrodites, females and animals subjected to empty-vector RNAi, were used as
358 controls, and the simultaneous presence of GFP::RHO-1 aggregates confirmed successful gene
359 knockdown. Unexpectedly, we found that the great majority of gene inhibitions prevented
360 lysosome acidification (Figure 4A and S12A). The ATP synthase genes *atp-2* and *atp-3* were
361 the only exceptions, consistent with previous observations suggesting that mitochondrial ATP
362 synthase activity acts downstream of lysosome acidification to prevent protein aggregation
363 (Bohnert and Kenyon, 2017).

364 Next, we asked whether reduced lysosomal acidification in the RNAi-treated hermaphrodites
365 might be caused by an inability to localize the V-ATPase subunits to lysosomes, as occurs in
366 females. To test this, we subjected GFP::VHA-13-expressing animals to assay-pool RNAi and
367 screened for the presence of GFP::VHA-13 puncta (Figure S12C). The extent of puncta
368 formation was quantified by measuring the skewness (non-homogeneity) of the GFP::VHA-13
369 signal at multiple locations within the most proximal oocyte. Hermaphrodites and the empty-
370 vector RNAi-treated animals demonstrated significantly higher skewness values than did female
371 oocytes, which exhibited diffuse GFP::VHA-13 localization (Figure 4B). All of the knockdowns
372 that blocked lysosome acidification showed reduced GFP::VHA-13 skewness, albeit to varying
373 degrees. While most knockdowns resulted in a marked reduction in GFP::VHA-13 skewness,
374 similar to the female, knockdown in some genes involved in protein folding (*cct-1, cct-5*), RNA
375 processing (*ess-2, let-711*) and calcium ion transport (*itr-1, sca-1*) demonstrated intermediate
376 values of skewness, indicative of at least a partial reduction of GFP::VHA-13 puncta (Figure

377 4B). Similarly, the orphan-gene inhibitions demonstrated reduced GFP skewness, with several
378 candidates showing only intermediate effects (*kin-2, par-5, xpo-1, rmd-2, lgc-46, aco2, imb-1*)
379 (Figure S12B). As anticipated, neither of the two ATP synthase gene knockdowns affected
380 GFP::VHA-13 puncta formation (Figure 4B). Together these data support the model that the
381 failure of the gene knockdowns to acidify lysosomes is due, at least in part, to a failure to
382 assemble the lysosomal V-ATPase.
383
384
385
386
387
388
389
390
391
392
393
394
395
396
397
398
399
400
401
402
403
404
405
406
407
408

Figure 4

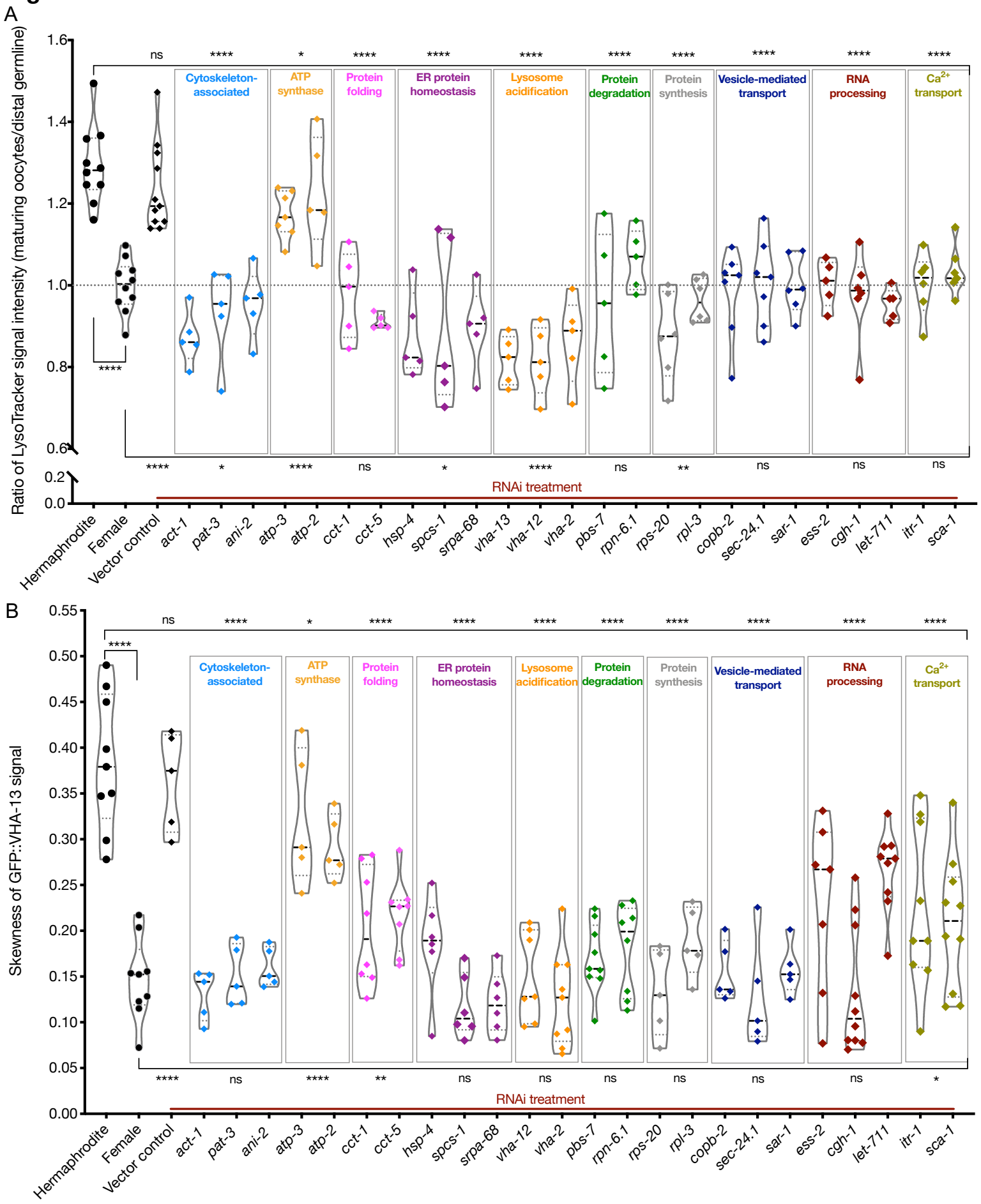
A
Ratio of LysoTracker signal intensity (maturing oocytes/distal germline)
1.6
1.4
1.2
1.0
0.8
0.6
0.2
0.0
ns
****
*
Cytoskeleton-associated
ATP synthase
Protein folding
ER protein homeostasis
Lysosome acidification
Protein degradation
Protein synthesis
Vesicle-mediated transport
RNA processing
Ca2+ transport
**
RNAi treatment
Hermaphrodite
Female
Vector control
act-1
pat-3
ani-2
atp-3
atp-2
cct-1
cct-5
hsp-4
spcs-1
srpa-68
vha-13
vha-12
vha-2
pbs-7
rpn-6.1
rps-20
rpl-3
copb-2
sec-24.1
sar-1
ess-2
cgh-1
let-711
itr-1
sca-1
B
Skewness of GFP::VHA-13 signal
0.55
0.50
0.45
0.40
0.35
0.30
0.25
0.20
0.15
0.10
0.05
0.00

Figure 4. Lysosome acidification and GFP::VHA-13 localization following knockdown of genes identified by the screen.

(A) LysoTracker staining in hermaphrodites (SA115) subjected to RNAi. The LysoTracker signal is represented as the ratio of proximal oocyte to distal germline staining. Staining ratios obtained from hermaphrodite (N2E) and female (CF4101) animals were used as controls (~1.3 and ~1.0, respectively). Each data point represents the average of values from three different locations in the most proximal oocyte from a single animal. The presence of GFP::RHO-1 aggregates in the same animals confirmed successful gene knockdown (not shown). (B) Analysis of GFP::VHA-13 localization, assessed by the degree of GFP skewness (inhomogeneity) in hermaphrodites (PHX1414) subjected to RNAi, and compared to control hermaphrodites and females (PHX1414 and CF4599). Each data point represents the average of ten skewness values from different regions within the first three proximal oocytes of a single animal. The presence of aggregates in GFP::RHO-1 animals (SA115) treated in parallel was used as a control to verify successful gene knockdown (not shown). For (A) and (B), Mann-Whitney test was used to determine the statistical significance. The top and bottom rows of significance indicators in each experiment compare the mean values from each process category to hermaphrodite and female animals, respectively. P values: $P > 0.05$ = n.s., *$P \leq 0.05$, **$P \leq 0.01$ and ****$P \leq 0.0001$.

409 *Two distinct, mysterious roles for mitochondria in protein aggregation.*

410 Mitochondria undergo a morphological and metabolic shift in response to signals from
411 sperm, a shift that is required for aggregate removal (Bohnert and Kenyon, 2017). Unfertilized
412 female oocytes exhibit a high mitochondrial membrane potential (ΔΨ) relative to hermaphrodite
413 oocytes or to female oocytes exposed to sperm by mating. Loss of the mitochondrial ATP
414 synthase, which discharges the proton gradient during the generation of ATP, elevates the ΔΨ
415 in hermaphrodites and causes protein aggregates to accumulate (Bohnert and Kenyon, 2017).
416 As expected, subunits from the mitochondrial ATP synthase complex (*atp-2, atp-3*) emerged
417 from the screen. Previously, we found that lysosomal V-ATPase activity was required for the
418 shift in mitochondrial membrane potential (Bohnert and Kenyon, 2017). To test the prediction
419 that our screen hits, which all inhibited lysosome acidification, would also block the ΔΨ switch,
420 we stained hermaphrodites with the dye DiOC6(3), whose signal is sensitive to ΔΨ. Again, to
421 control for dye uptake, we measured the ratio of DiOC6(3) staining intensities between proximal
422 oocytes and the distal syncytial germline. As predicted, all of the knockdowns prevented the ΔΨ
423 decrease in proximal hermaphrodite oocytes. Unexpectedly, in many cases the mitochondria
424 exhibited ΔΨ ratios even higher than those of females (Figure 5A and S13A), suggesting that
425 the female oocyte ΔΨ is not the default state, but potentially an optimal point within a broader
426 range of possibilities.

427 The observation that gene knockdowns from all the functional categories caused a relatively
428 high oocyte ΔΨ value prompted us to question whether a high mitochondrial membrane
429 potential might be necessary for protein aggregate accumulation. To test this, we asked whether
430 exposing females expressing germline GFP::RHO-1 to conditions that lower ΔΨ; namely, to
431 electron-transport chain (ETC) RNAi knockdowns, might reduce protein aggregation. However,
432 neither *cyc-1* nor *nuo-2* RNAi prevented females from accumulating aggregates, even though
433 ΔΨ was reduced (Figure 5B, S13B and S13C). Thus, a high mitochondrial membrane potential
434 is not a prerequisite for protein aggregation.

435 RNAi-inhibition of ATP synthase has been shown to reduce ATP levels in worms, as does RNAi
436 inhibition of electron transport (Dillin et al., 2002; Lee et al., 2003). To ask whether inhibiting
437 ATP synthase was likely to cause protein aggregation in hermaphrodites by limiting ATP levels,
438 we analyzed hermaphrodites subjected to ETC RNAi. The treatments reduced oocyte ATP
439 levels (S14A-C), and reduced body size and growth rate (Figure 5B), two known correlates of
440 reduced ATP levels. However, these perturbations did not cause protein aggregation in
441 hermaphrodite oocytes (Figure 5B). This finding suggests the interesting hypothesis that loss of
442 ATP synthase causes aggregates to accumulate in hermaphrodites not because it limits ATP
443 levels, but for a different reason (see Discussion).
444 Given the striking change in mitochondrial dynamics that takes place during oocyte maturation,
445 we were surprised that in our screen we recovered only one additional gene encoding a
446 mitochondrial-localized protein, *aco-2* (Krebs-cycle aconitase). We tested several additional
447 Krebs-cycle gene knockdowns (*pdha-1, idhg-1, ogdh-1, sucl-1,* and *sdhd-1*), and found that α-
448 ketoglutarate dehydrogenase (*ogdh-1*) and succinate dehydrogenase (*sdhd-1*) RNAi also led to
449 oocyte GFP::RHO-1 aggregation (Figure S13D). Notably, unlike ATP-synthase inhibition, *aco-2*
450 inhibition prevented lysosome acidification (Figure S12A), indicating that the Krebs cycle and
451 ATP synthase likely have distinct roles in the protein-aggregation pathway.
452
453
454 *ESCRT-complex genes are required for the clearance of protein aggregates.*
455 The direct mechanism by which protein aggregates are removed during oocyte
456 maturation is not known with certainty, although morphologically, the process resembles
457 lysosomal microautophagy (Bohnert and Kenyon, 2017). Microautophagy has not been
458 described previously in *C. elegans*; however, orthologs of genes encoding components of the
459 ESCRT machinery, which mediates microautophagy in yeast and mammals, are present (Sahu
460 et al., 2011; Williams and Urbé, 2007). We identified two ESCRT subunits (*vps-37* and *vps-54*)

461 in our primary screen, but they did not pass our initial validation cutoff (Table S3). To explore
462 the possibility that these were false negatives, we retested these RNAi clones along with RNAi
463 clones inhibiting additional ESCRT subunits (*tsg-101*, *vps-20* and *vps-28*). In these experiments,
464 the ESCRT subunits *vps-20*, *vps-28*, *vps-37*, and *vps-54* tested positive with subtle aggregation
465 phenotypes (although not observed in all animals tested) (Figure S15A), supporting the model
466 that aggregates are removed via microautophagy. Importantly, the degree of GFP::VHA-13
467 localization to puncta in these knockdowns was comparable to that of hermaphrodites (Figure
468 S15B, S15C), and they also permitted acidification of oocyte lysosomes (Figure 5C, S15C).
469 Taken together, these findings suggest that the ESCRT machinery operates downstream of V-
470 ATPase assembly and lysosome acidification to prevent aggregate accumulation.
471
472
473
474
475
476
477
478
479
480
481
482
483
484
485
486
487
488
489
490
491

Figure 5

A

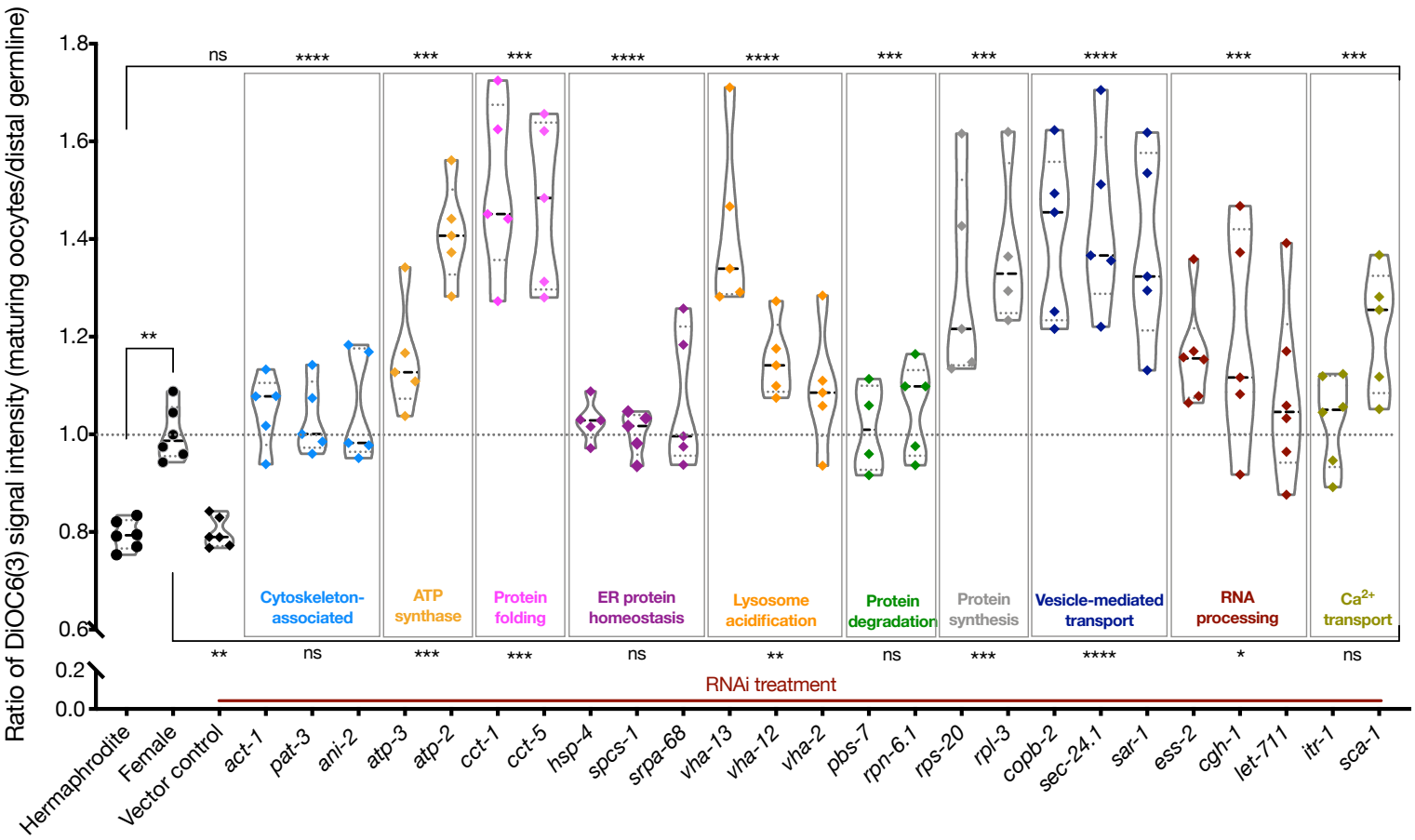
Ratio of DiOC6(3) signal intensity (maturing oocytes/distal germline)
1.8
1.6
1.4
1.2
1.0
0.8
0.6
0.2
0.0
ns
****
***
***
****
****
***
***
****
***
***
**
Cytoskeleton-associated
ATP synthase
Protein folding
ER protein homeostasis
Lysosome acidification
Protein degradation
Protein synthesis
Vesicle-mediated transport
RNA processing
Ca2+ transport
**
ns
***
***
ns
**
ns
***
****
*
ns
RNAi treatment
Hermaphrodite
Female
Vector control
act-1
pat-3
ani-2
atp-3
atp-2
cct-1
cct-5
hsp-4
spcs-1
srpa-68
vha-13
vha-12
vha-2
pbs-7
rpn-6.1
rps-20
rpl-3
copb-2
sec-24.1
sar-1
ess-2
cgh-1
let-711
itr-1
sca-1

B

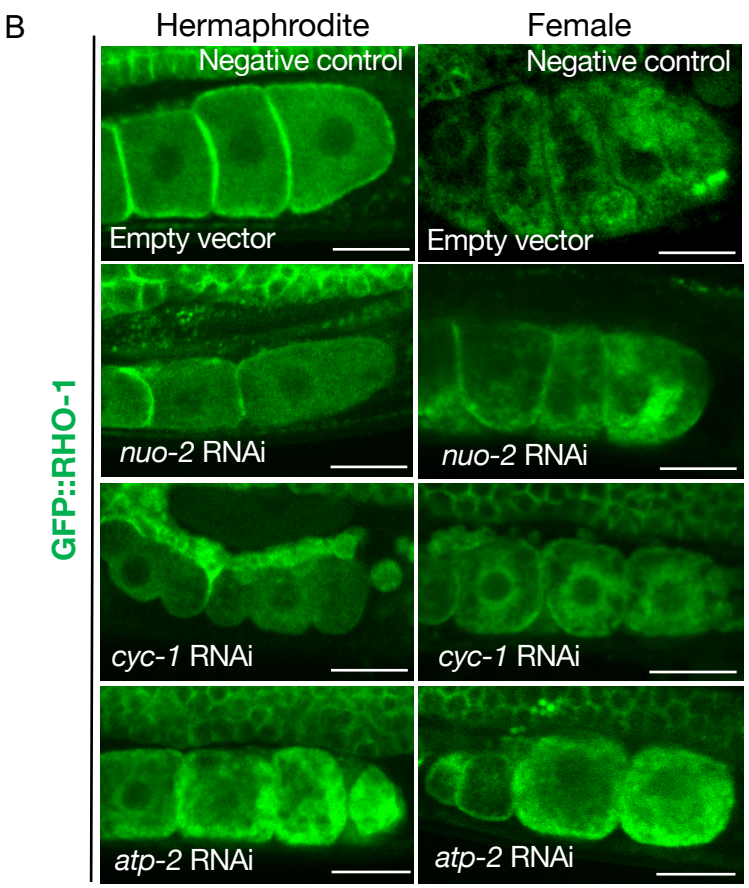
Hermaphrodite
Female
GFP::RHO-1
Negative control
Negative control
Empty vector
Empty vector
nuo-2 RNAi
nuo-2 RNAi
cyc-1 RNAi
cyc-1 RNAi
atp-2 RNAi
atp-2 RNAi

C

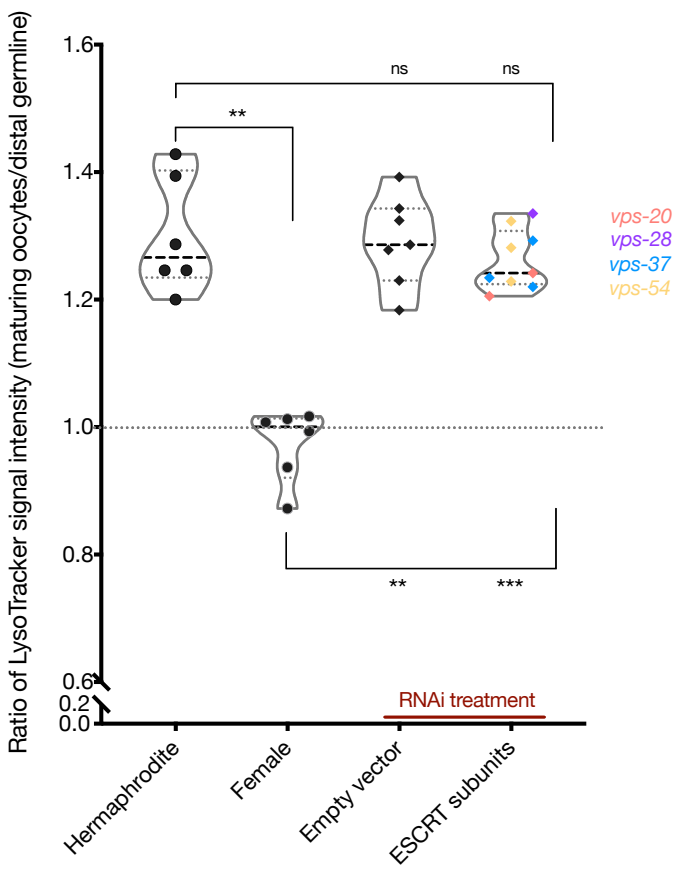
Ratio of LysoTracker signal intensity (maturing oocytes/distal germline)
1.6
1.4
1.2
1.0
0.8
0.6
0.2
0.0
ns
ns
**
**
***
vps-20
vps-28
vps-37
vps-54
RNAi treatment
Hermaphrodite
Female
Empty vector
ESCRT subunits

Figure 5. Analysis of mitochondrial membrane potential and ESCRT-complex subunits

(A) Analysis of oocyte ΔΨ using DiOC6(3) staining in RNAi-treated hermaphrodites (OCF15), represented as the ratio of proximal oocyte to distal germline staining. Staining ratios obtained from N2E hermaphrodites (~0.8) and CF4101 females (~1) were used as controls for comparison. Each data point represents the average of values from three different locations in the most proximal oocyte of a single animal. When applicable, alteration in ER morphology was used as a control to determine successful gene knockdown in the same animals. The presence of GFP::RHO-1 aggregates in SA115 animals treated in parallel, was also used as an RNAi control (not shown). (B) Visualization of GFP::RHO-1 aggregates in oocytes of hermaphrodites (SA115) and females (CF4115) subjected to disruption of mitochondrial electron transport chain genes. Successful ETC disruption was confirmed by smaller body sizes (visible in the images), and severely reduced brood sizes, similar to ATP synthase subunit knockdowns. Scale bars, 25 μm. (C) LysoTracker staining in hermaphrodites (SA115) subjected to ESCRT-complex RNAi, represented as the ratio of proximal oocyte to distal germline staining, and compared to hermaphrodites (N2E) and females (CF4101). Only animals exhibiting GFP::RHO-1 aggregates upon RNAi treatment (confirming knockdown; shown in Fig. S15A), were included in the quantification. For (A) and (C), Mann-Whitney test was used to determine the statistical significance. The top and bottom rows of significance indicators in each experiment compare the mean values from each process category to hermaphrodite and female animals respectively. P values: $P > 0.05$ = n.s., *$P \leq 0.05$, **$P \leq 0.01$, ***$P \leq 0.001$ and ****$P \leq 0.0001$.

492 *Mechanisms enhancing germline proteostasis also operate in the soma.*

493 Widespread proteostasis collapse is an inherent part of aging in *C. elegans* (Ben-Zvi et
494 al., 2009; David et al., 2010; Taylor and Dillin, 2011; Walther et al., 2015), and mechanisms that
495 extend lifespan invariably enhance cellular proteostasis. Understanding how the immortal germ
496 lineage maintains cellular quality and proteostasis across the generations could suggest new
497 ways to enhance proteostasis in the soma and delay organismal aging. Our lab and others have
498 shown that many endogenous proteins become insoluble with age and can form visible
499 aggregates when overexpressed with fluorescent tags (David et al., 2010; Huang et al., 2019;
500 Reis-Rodrigues et al., 2012; Roux et al., 2016). To visualize age-related protein aggregation, we
501 monitored the casein kinase subunit KIN-19, which forms insoluble aggregates in an age-
502 dependent manner in wild-type somatic tissues (David et al., 2010). To do this, we fluorescently-
503 tagged the endogenous *kin-19* gene specifically in the soma using split-wrmScarlet (Goudeau et
504 al., 2021) (Table S2). To avoid interference from the bright intestinal autofluorescence, we
505 examined KIN-19::split-wrmScarlet in the head. The signal was mainly diffuse in young day-1
506 adults but began to exhibit a striking punctate appearance as early as day-4 of adulthood
507 (Figure 6A, 6B, S16A-C). To the best of our knowledge, this tool is the first used to visualize
508 age-dependent aggregation of an endogenously-expressed protein in *C. elegans*.

509 To ask whether the germline-proteostasis genes we identified in our screen might also affect
510 somatic protein aggregation, we screened our germline-aggregation 'assay pool' for gene
511 knockdowns that caused KIN-19 to aggregate prematurely in head tissues. We found that
512 multiple RNAi knockdowns that impaired lysosomal acidification in the germline induced
513 premature KIN-19::split-wrmScarlet aggregation in the soma, most notably RNAi of genes
514 encoding lysosomal V-ATPase subunits (*vha-12*, *vha-13*, *vha-16* and *vha-19*), but also genes
515 that, in the germline, were required for V-ATPase assembly (the actin gene *act-5* and the
516 vesicle-mediated ER-to-Golgi transport gene *copb-2*) (Figure 6C,D). We were not able to
517 visualize lysosome acidification in the head using LysoTracker, but these knockdowns did affect

518 lysosome acidification in the intestine, where the RNAi treatment led to fewer discrete acidic
519 lysosome-related organelles (LROs) thereby reducing the skewness of the LysoTracker signal
520 (Figure 6E and S17). We also recovered the proteasome subunits *pbs-7* and *rpn-6.1*, indicating
521 a direct or indirect role for proteasome function to maintain KIN-19 solubility in the aging soma
522 (Figure 6C and 6D).
523 We also tested a second somatic-aggregation reporter, the polyQ protein, Q35::YFP
524 expressed in body-wall muscles (Morley et al., 2002). Similar to KIN-19::split-wrmScarlet, *vha-*
525 *12* and *vha-19* knockdowns accelerated the timing of age-related Q35::YFP aggregation, as did
526 *copb-2* and *rpn-6.1* RNAi (Figure S18). Interestingly, a few additional genes were identified that
527 were not hits in the KIN-19::split-wrmScarlet screen. These included the cytosolic chaperones
528 *cct-1* and *cct-5*, another trafficking component *rab-11.1* and three orphans with diverse cellular
529 function, *imb-1, itr-1* and *let-711* (Figure S18 and Table S1). Further, knocking down one of the
530 four ESCRT complex subunits we tested, *vps-37*, also led to Q35::YFP aggregation (Figure
531 S18). In contrast, none of the ESCRT gene knockdowns accelerated the KIN-19::split-
532 wrmScarlet somatic aggregation, even in animals exposed to RNAi from the first larval stage,
533 despite significant decrease in mRNA levels in the two subunits measured (Figure S19A-C).
534 Together these findings suggest that lysosomal microautophagy may prevent the accumulation
535 of Q35::YFP aggregates, but future studies will be required for certainty.
536
537
538
539
540
541
542
543
544

Figure 6

A Endogenous KIN-19::split-wrmScarlet$_{11}$ + somatic split-wrmScarlet$_{1-10}$

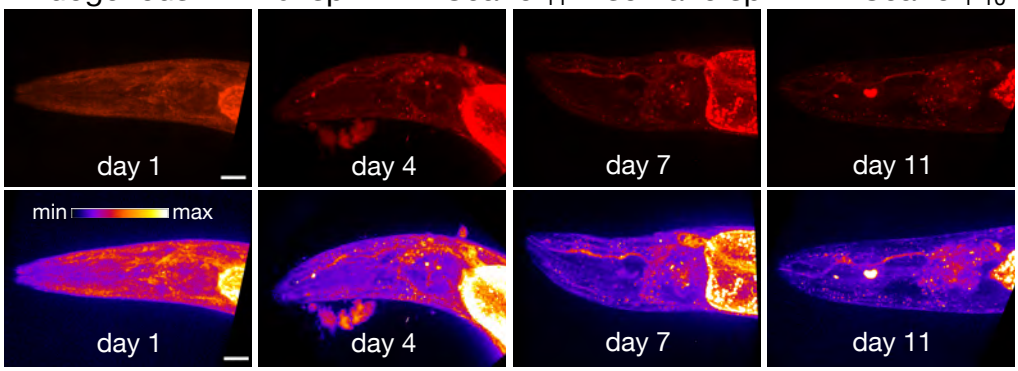

B

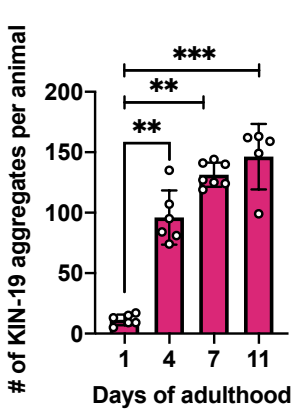

C

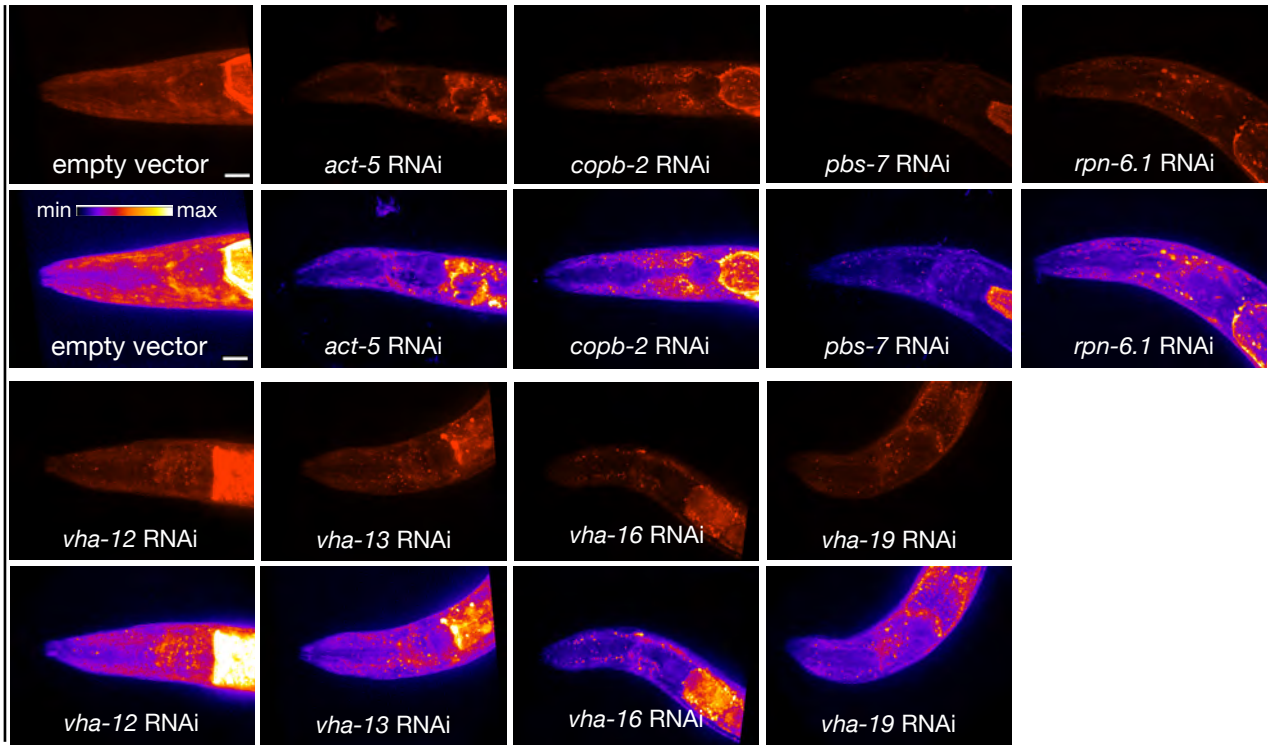

D

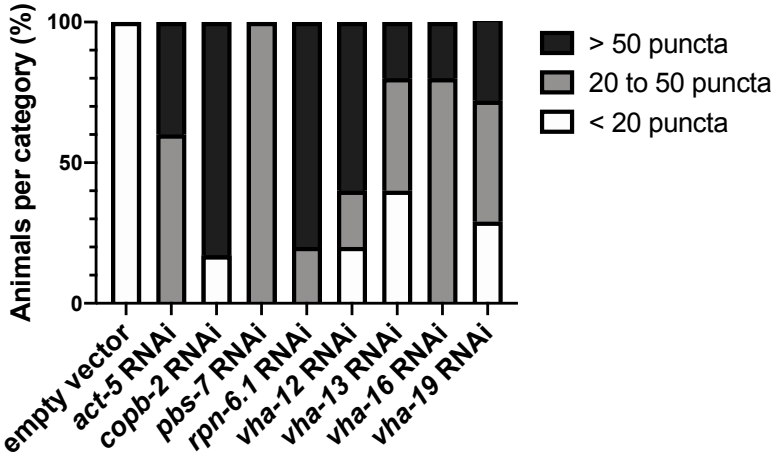

E

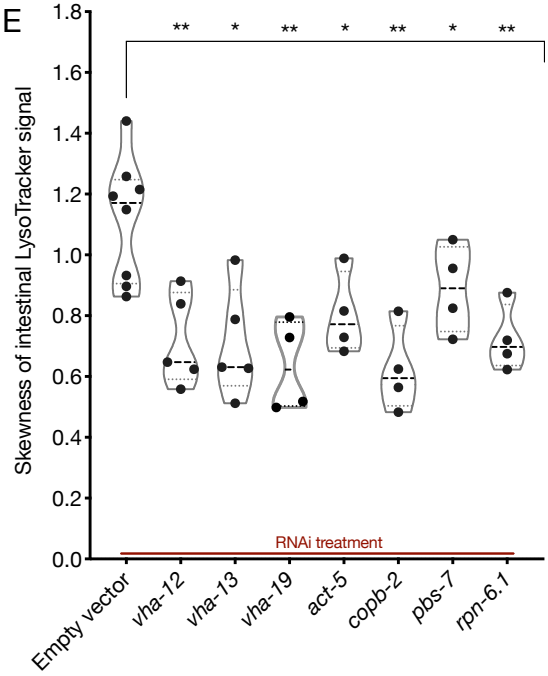

Figure 6. Analysis of protein aggregation and lysosome acidification in somatic tissues.

(A) Representative images of CF4609 animals expressing KIN-19::split-wrmScarlet$_{11}$ and somatic split-wrmScarlet$_{1-10}$ at day-1, 4, 7 and 11 of adulthood. Maximum intensity projections of 3D stacks are shown in red (upper panels), and also using an intensity scale (lower panels). Scale bars, 10 μm. (B) Quantification of KIN-19::split-wrmScarlet aggregates per animal in the head region. The bright fluorescent signal in the pharyngeal region was not included in the quantification. Mann-Whitney test was used to determine the statistical significance. P values: **$P \leq 0.01$ and ***$P \leq 0.001$. (C) Representative images of CF4609 animals expressing KIN-19::split-wrmScarlet$_{11}$ and somatic split-wrmScarlet$_{1-10}$ subjected to RNAi or empty-vector negative control; imaged for presence of KIN-19 aggregates at day-2 of adulthood. Scale bars, 10 μm. (D) Quantification of fluorescent KIN-19::split-wrmScarlet puncta (only from the head region) in CF4609 animals subjected to RNAi or empty-vector control. (E) Skewness of the intestinal LysoTracker signal in SA115 animals subjected to RNAi (shown in Figure S17). Each data point represents the average of six independent skewness values from the anterior intestinal region, near the pharyngeal bulb, in a single animal. The simultaneous presence of GFP::RHO-1 aggregates in oocytes, was used as a control for successful gene knockdown in each animal (not shown). Mann-Whitney test was used to determine the statistical significance. P values: *$P \leq 0.05$ and **$P \leq 0.01$.

545 **Discussion**

546 Sperm-derived signals that trigger oocyte maturation in *C. elegans* initiate a global change in
547 oocyte structure and function, including the rapid removal of protein aggregates. A key step in
548 aggregate removal is the acidification of lysosomes, which subsequently engulf the aggregates
549 (Bohnert and Kenyon, 2017). In addition, mitochondria, which undergo morphological and
550 metabolic changes in response to maturation signals, appear to play an important regulatory
551 role, as inhibition of mitochondrial ATP synthase prevents the downshift in mitochondrial
552 membrane potential normally triggered by sperm, and causes aggregates to form even when
553 sperm are present (Bohnert and Kenyon, 2017). In this study, we identified a key role for a third
554 organelle, the ER, in proteostasis renewal, and, using genetic and cell biological approaches,
555 we deepened our understanding of all three organelles, the ER, lysosomes and mitochondria, in
556 oocyte protein-quality control.

557

558 *Limits of our genetic screen*

559 To identify additional genes and processes involved in protein-aggregate metabolism in
560 oocytes, we carried out a genome-wide screen for RNA-inhibitions that cause proteins to
561 aggregate even in the presence of sperm; namely, in hermaphrodites. We expected to identify
562 genes and processes that are directly involved in the sperm-dependent proteostasis switch, as
563 well as genes that function more indirectly in protein homeostasis and cellular quality control.
564 Many of the genes we recovered affected large multiprotein complexes, such as the ribosome
565 and proteasome, making a compelling argument for these complexes influencing protein
566 aggregation, directly or indirectly. However, we may have missed processes carried out by only
567 one or a few genes if the corresponding RNAi bacteria were missing from the RNAi library or
568 otherwise problematic; or if their inhibition produced milder protein-aggregation phenotypes, like
569 the ESCRT genes that failed our initial, stringent validation tests (Table S3).

570 To place the genes into a proteostasis pathway, we asked which hallmarks of the sperm-
571 triggered aggregate-clearance pathway (lysosome acidification, mitochondrial membrane-
572 potential shift, etc.) were blocked by the knockdowns (Figure 7). An intrinsic limitation of this
573 strategy is that it only identifies the first role of a gene that acts in multiple steps in the process.
574 For example, because inhibiting the proteasome prevents degradation of the proximal-oocyte
575 cell-fate determinant GLD-1 (Bohnert and Kenyon, 2017; Kisielnicka et al., 2018), and inhibiting
576 various other chaperones prevents lysosome acidification, we cannot determine whether these
577 proteins also play a direct role in the process of aggregate clearance itself. Finally, we note that
578 perturbations that prevent sperm from producing the MSP oocyte-maturation signal would also
579 cause protein aggregation in hermaphrodites. The fact that the great majority of the knockdowns
580 did not replicate female oocyte morphology exactly (Figures 5A and S13A) argues against this
581 possibility, but we have not ruled it out definitively.
582
583
584
585
586
587
588
589
590
591
592
593
594
595
596
597
598
599

Figure 7

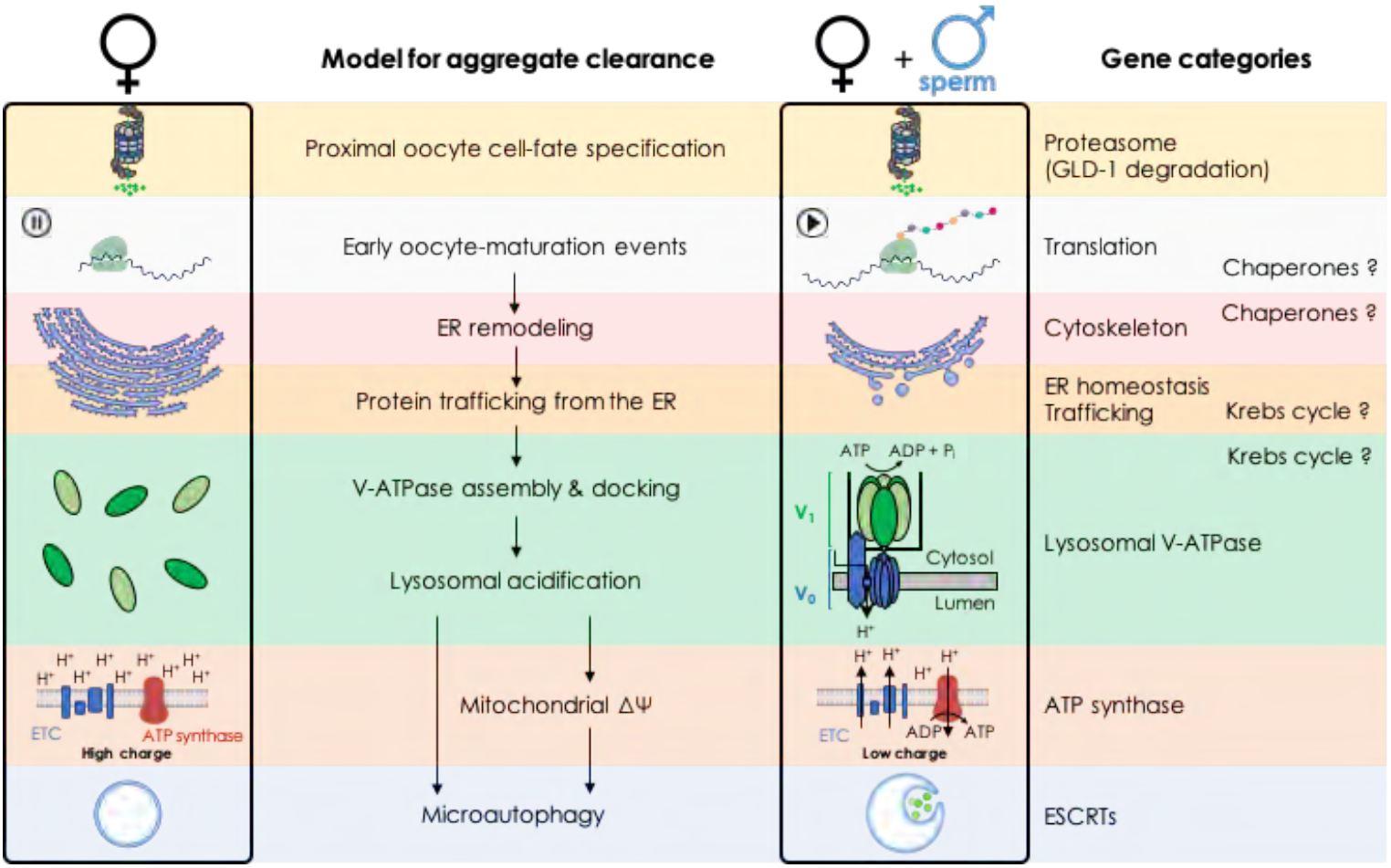
Model for aggregate clearance
Gene categories
sperm
Proximal oocyte cell-fate specification
Proteasome
(GLD-1 degradation)
Early oocyte-maturation events
Translation
Chaperones ?
ER remodeling
Cytoskeleton
Chaperones ?
Protein trafficking from the ER
ER homeostasis
Trafficking
Krebs cycle ?
V-ATPase assembly & docking
Krebs cycle ?
Lysosomal acidification
ATP
ADP + Pi
V1
V0
Cytosol
Lumen
Lysosomal V-ATPase
Mitochondrial ΔΨ
ETC
ATP synthase
High charge
ADP
ATP
Low charge
ATP synthase
Microautophagy
ESCRTs

Figure 7.

Model: Biological processes implicated in the clearance of protein aggregates during oocyte maturation.

600 *A role for the endoplasmic reticulum*

601 Many of the genes we identified affected the endoplasmic reticulum (Figure 7; Table 1). All of
602 these gene inhibitions prevented lysosome acidification, arguing that ER function influences
603 aggregate formation indirectly, acting at a relatively early step in the proteostasis pathway
604 (though ER function could be required again, at later stages, as well). Using transmission
605 electron microscopy and fluorescent reporters, we validated and extended previous
606 observations of ER reorganization during *C. elegans* oocyte maturation (Langerak et al., 2019).
607 We found that the ER assumes a stacked arrangement, spatially distinct from GFP::RHO-1
608 protein aggregates, in the proximal oocytes of females. Importantly, we found that neither the
609 ER stacking, nor protein-aggregate accumulation, were a consequence of long-term oocyte
610 quiescence ("oocyte aging"), as both were present as soon as female oocytes appeared during
611 development. When oocyte maturation was triggered by mating, the ER underwent a rapid
612 reorganization that preceded aggregate removal, consistent with a model that ER activity might
613 be a precondition for aggregate clearance.

614 The ER-gene inhibitions fell into two classes. First was a set of genes with known ER functions
615 that did not appear to affect ER morphology: *hsp-4* (BIP), *spcs-1* (signal peptidase complex
616 subunit), and *srpa-68* (signal recognition particle). This finding argues that ER reorganization
617 does not require ER function itself. The second class did affect ER morphology, generally
618 causing the ER from hermaphrodites to exhibit a bright patchy appearance characteristic of
619 (though not necessarily identical to) that seen in female oocytes. Some of these gene
620 knockdowns, such as that of *itr-1,* which encodes the channel that releases calcium stored in
621 the ER, likely cause hermaphrodites to adopt a female-specific, stacked ER morphology. In *C.*
622 *elegans*, the major wave of oocyte calcium release occurs after fertilization; this finding
623 suggests that ER-dependent calcium metabolism plays an important earlier role as well. Other
624 RNAi knockdowns may simply disrupt ER morphology more generally and might not identify
625 genes that play an active role in the oocyte proteostasis switch. For example, the actin

626 cytoskeleton is known to influence ER morphogenesis (Poteryaev et al., 2005), and we
627 recovered a number of cytoskeletal gene hits. Notably, TRiC-complex chaperonin genes fell into
628 this class as well. The TRiC-complex chaperonin can counteract protein aggregation directly; for
629 example, by promoting correct protein folding during protein synthesis. However, TRiC is known
630 to assist in folding cytoskeletal components including actin and tubulin (Llorca et al., 2000) and
631 it was interesting to find that the TRiC-complex genes we recovered, *cct-1* and *cct-5,* acted
632 indirectly, by affecting ER morphology and lysosome acidification. As mentioned above, the
633 proteasome, too, affects aggregate clearance indirectly. In general, it might be valuable to assay
634 lysosome acidification when analyzing the functions of these chaperone/chaperonin systems on
635 the accumulation of protein aggregates in other cellular systems, to test for the possibility of
636 indirect effects. That said, it is also possible that TRiC-complex and other chaperones act at
637 multiple points in the proteostasis pathway, with both indirect and direct effects on protein
638 aggregation.
639 Finally, we identified several genes that, to our knowledge, were not previously known to
640 influence ER morphology; namely, *dlg-1*, *kin-2, and ttr-14* (Table 1). How these genes act,
641 directly or indirectly, to influence the ER could be interesting to explore in the future.
642
643 *Regulation of lysosome acidification*
644 Lysosome acidification may be a conserved aspect of oocyte maturation, as it takes place in
645 *Xenopus* as well as *C. elegans* (Bohnert and Kenyon, 2017). A central goal of this study was to
646 better understand how this lysosome acidification is regulated in worms. To this end, we first
647 generated functional, fluorescently-tagged V-ATPase subunits expressed from their own loci.
648 However, for reasons that we do not understand, none of these proteins was visible in the
649 germline. We then obtained a stable, single-copy MosSCI strain in which *gfp::vha-13* was
650 expressed from a germline-specific promoter. In these animals, GFP::VHA-13 was visible, and
651 we observed a striking sperm-dependent localization pattern. In the presence of sperm (in

652 hermaphrodites), GFP::VHA-13 was located on lysosomes; that is, it assumed a punctate
653 appearance that co-localized with LysoTracker signal. In the absence of sperm (in unmated
654 females), the protein was distributed throughout the cytoplasm (Figure 7). The simplest
655 interpretation of these findings is that signals from sperm trigger the localization of GFP::VHA-
656 13 to lysosomes, and that this localization enables lysosome acidification. In principle, additional
657 levels of control, such as translational repression of V-ATPase synthesis, could operate as well,
658 since our overexpressed construct could potentially override negative regulators; though we
659 observed no evidence of this with serially-diluted *gfp* RNAi treatments that progressively
660 reduced visible GFP::VHA-13 protein levels.

661 In yeast, peripheral, cytoplasmic V_1 subunits of the V-ATPase (such as VHA-13) localize
662 to lysosomes when the membrane-localized V_0 sector is trafficked there from the ER, where it is
663 assembled (Graham et al., 1998). Thus, we propose that the extensive rearrangement in ER
664 morphology triggered by sperm in *C. elegans* oocytes is coupled to movement of either pre-
665 existing or newly-synthesized membrane-localized V_0 subunits of the V-ATPase from the ER to
666 lysosomes, where they create docking sites for cytoplasmic, peripheral V_1 subunits. Consistent
667 with this idea, RNAi of the ER genes, as well as each of the three genes required for vesicle
668 trafficking from the ER to lysosomes, prevented GFP::VHA-13 localization to lysosomes, as did
669 inhibiting genes encoding the membrane-localized V-ATPase V_0 subunits. Unfortunately, our
670 efforts to observe the predicted sperm-activated movement of V_0 subunits from the ER to
671 lysosomes were thwarted by our inability to visualize either of two functional wrmScarlet-tagged
672 V_0 subunits, even when overexpressed using MosSCI technology. In the future, immuno-gold
673 EM labeling of endogenous V_0 subunits might enable this model to be tested more directly.
674 We note that an interesting puzzle remains unexplained: If the multi-subunit lysosomal V-
675 ATPase complexes are present in such low amounts in mature oocytes that they cannot be
676 seen when we fluorescently tag the endogenous *vha-13* gene, then why do they appear when
677 the tagged VHA-13 protein is overexpressed? How does the excess GFP::VHA-13 protein dock

678 onto lysosomes? Perhaps the ER supplies lysosomes with alternative docking sites for
679 unassembled V-ATPase subunits, or perhaps the stoichiometry change due to the excess
680 GFP::VHA-13 subunits triggers the production of entirely new V-ATPase complexes that
681 incorporate the overexpressed GFP::VHA-13 subunits. This remains an unexplained but
682 intriguing mystery (Hughes and Gottschling, 2012).
683 The gene knockdowns identified by the screen nearly all failed to acidify lysosomes, reinforcing
684 the central role of acidified lysosomes in clearing oocyte protein aggregates (Figure 7).
685 Moreover, none of the knockdowns that failed to acidify lysosomes exhibited a punctate,
686 lysosomal GFP::VHA-13 pattern (Table 1). This finding suggests that V-ATPase activity may not
687 only be necessary but also sufficient for lysosome acidification; however, this interpretation
688 remains tentative, since we may simply have failed to identify the relevant genes in our screen.
689 Finally, several of the knockdowns from our screen did not appear to affect ER morphology (and
690 have not been reported to affect ER function), but did prevent V-ATPase localization, for
691 example *srab-17*, a chemosensory gene of the serpentine receptor class ab, and *lgc-46,*
692 involved in chloride ion transport (Table 1). How, directly or indirectly, these proteins might
693 influence V-ATPase localization and assembly is an interesting question to pursue in the future.
694
695 *Two Roles for Mitochondria*
696 Like the ER and lysosomes, mitochondria undergo morphological and functional changes during
697 *C. elegans* oocyte maturation. In response to sperm, the mitochondria of proximal oocytes
698 reduce their relatively high membrane potential and shift from a fragmented to a tubular
699 structure. Inhibiting mitochondrial ATP synthase preserves this high membrane potential even
700 when sperm are present and causes aggregates to accumulate. Injecting ADP, whose levels
701 would be expected to rise as maturing oocytes initiate protein synthesis and acidify lysosomes,
702 reduces the mitochondrial membrane potential in female oocytes, in an ATP-synthase
703 dependent fashion. Together these findings suggested the model that in the absence of sperm,

704 mitochondria are held in a quiescent, poised state that relaxes as metabolic activity and ATP
705 synthesis commences (Bohnert and Kenyon, 2017).
706 Whether *C. elegans* oocyte maturation is powered primarily by glycolysis or respiration is
707 unknown; however, in principle, the accumulation of protein aggregates caused by inhibiting
708 mitochondrial ATP synthase could reflect ATP limitation. However, if this were the case, then
709 inhibiting components of the electron transport chain should also cause protein aggregates to
710 accumulate in hermaphrodites, since this, too, limits ATP levels. However, although these
711 knockdowns reduced oocyte ATP levels, body size, growth rates and brood size, this was not
712 the case; ETC knockdowns had no effect on protein aggregation. This unexpected finding
713 suggests that ATP-synthase knockdown prevents aggregate clearance not because of changes
714 in ATP levels, but instead either because a continuously high mitochondrial membrane potential
715 acts like a checkpoint to inhibit aggregate clearance (Figure 7), or because of another, unknown
716 role of ATP synthase in protein homeostasis.
717 Our screen revealed an additional requirement for mitochondria in protein homeostasis;
718 specifically, for Krebs cycle activity. Inhibiting mitochondrial aconitase (*aco-2)* produced a
719 different phenotype from inhibiting ATP synthase; namely, a failure to acidify lysosomes. Why
720 might this be? Again, the explanation seems unlikely to involve energy limitation, since inhibiting
721 ETC components or ATP synthase did not produce this phenotype. One possibility is that
722 inhibiting the Krebs cycle affects lysosome acidification by affecting redox potential, as several
723 Krebs cycle enzymes affecting protein aggregation (*ogdh-1* and *sdhd-1*) encode
724 dehydrogenases that produce the reducing agents NADH and $FADH_2$, and aconitase supplies
725 the substrate for another Krebs cycle dehydrogenase. Alternatively, other metabolites generated
726 via Krebs cycle intermediates could influence the events leading to lysosome acidification. It will
727 be interesting to explore this mechanism in the future.
728
729 *Microautophagy*

730 Previously, we observed lysosomes engulfing protein aggregates in a process reminiscent of
731 microautophagy (Bohnert and Kenyon, 2017). Before these observations, microautophagy had
732 not been described in *C. elegans.* In this study, using a candidate approach, we showed that
733 inhibiting ESCRT-complex members, which are known to mediate microautophagy in other
734 organisms, prevents aggregate accumulation in maturing *C. elegans* oocytes. Moreover, they
735 influence protein aggregation independently of lysosomal acidification, consistent with their
736 having a direct role. These findings strengthen the case that microautophagy is an active
737 proteostasis mechanism in *C. elegans,* and likely the mechanism by which aggregates are
738 cleared in response to oocyte-maturation signals (Figure 7).
739
740 *Implications for somatic proteostasis and aging*
741 Together our findings all point towards lysosomal acidification being a key, determinative event
742 in oocyte protein-aggregate clearance. Moreover, the screen hits that affected the lysosomal V-
743 ATPase and COPII (ER-to-lysosomal vesicle transport) had a striking ability to accelerate age-
744 dependent protein aggregation in somatic cells. Thus, the same mechanisms that enhance
745 oocyte proteostasis in the immortal germline likely enhance somatic proteostasis as well. These
746 findings may have implications for aging and longevity more broadly. In yeast, lysosomal acidity
747 declines with age, and overexpressing the yeast ortholog of the *C. elegans* V-ATPase gene
748 *vha-13* delays this decline and extends replicative lifespan (Hughes and Gottschling, 2012). In
749 worms, lysosome acidification also declines with age, and this decline is delayed in long-lived
750 mutants (Baxi et al., 2017; Sun et al., 2020). Whether increasing V-ATPase function might be
751 sufficient to extend lifespan in *C. elegans* is unclear, but overproduction of the transcription
752 factor HLH-30/TFEB, which augments many lysosomal functions, has been shown to do so
753 (Lapierre et al., 2013; O'Rourke and Ruvkun, 2013), and in mammals, similar perturbations slow
754 the aging of the immune system (Zhang et al., 2019).

755 In summary, a genetic screen for proteostasis enhancers in the immortal germ lineage has
756 revealed a landscape of interconnected processes, spanning protein translation, cytoskeletal
757 dynamics, Krebs cycle activity, ER activation and vesicle transport, that together enable
758 lysosome acidification and clearance of protein aggregates during oocyte maturation.
759 Lysosomal acidification maintains proteostasis in the aging soma as well. In addition to raising
760 many new questions for future investigations, our findings support a growing body of evidence
761 that interventions that rejuvenate lysosomal activity during aging might yield new ways to
762 increase human health and longevity.
763
764

765 **Acknowledgements:**
766 We thank colleagues in the Kenyon lab and at Calico Life Sciences for advice and discussion,
767 and Daniel Gottschling and Calvin Jan for comments on the manuscript. Special thanks to
768 Andrew Dillin (University of California, Berkeley) for sharing his transmission electron
769 microscopy resources, and Peichuan Zhang for help with converting the RNAi collection format.
770 We thank Robert Keyser for help with liquid handling robotics for the primary screen, and Kayley
771 Hake for suggesting skewness as a way to capture aggregate formation in microscopy images.
772 Peichuan Zhang and Rex Kerr helped to analyze somatic KIN-19::split-wrmScarlet aggregation.
773 We thank Di Chen for sharing the DCL565 and DCL569 strains. Some *C. elegans* strains were
774 provided by the CGC, which is funded by NIH Office of Research Infrastructure Programs (P40
775 OD010440). The endogenously tagged V-ATPase *C. elegans* strains were generated by
776 SunyBiotech, China. Some illustrations in Figures 1 and 7 were created with BioRender.com.
777 The study was supported by Calico Life Sciences DHH was supported by NIH OD010943, and
778 MeS was supported by HHMI funding to A. Dillin.
779

780 **Author contributions:**

781 Ma.S and J.G executed all experiments with the exception of the ATP sensor analysis,
782 performed by M.I., and electron microscopy, performed by Me.S, in Andrew Dillin's laboratory.
783 D.H.H provided advice for the TEM experiments and helped in the interpretation of the TEM
784 images. K.A.B provided valuable inputs in the early stages of the project and contributed to the
785 ER and ETC analysis. M.I. provided help and advice for fluorescence microscopy experiments
786 and data analysis. The research and analysis was designed by Ma.S, J.G and C.K, who also
787 prepared the final manuscript.

788

789

790

791

792

793

794

795

796

797

798

799

800

801

802

803

804 **Materials and Methods:**

Key Resources Table				
Reagent type (species) or resource	**Designation**	**Source or reference**	**Identifiers**	**Additional information**
Genes (*Caenorhabditis elegans*)	Multiple			Table S1
Strains, (*Caenorhabditis elegans*)	Multiple			Table S2
Sequence-based reagent	kin-19_F	This paper	PCR Primer	AGGCTCAACAATCGCAATCC
Sequence-based reagent	kin-19_R	This paper	PCR Primer	TTTGAGTGCCCGACATTGGG
Peptide, recombinant protein	Alt-R® S.p. Cas9 Nuclease V3	IDT	1081058	
Commercial assay or kit	LysoTracker Red DND-99	Life Technologies	L7528	
Commercial assay or kit	DiOC6(3)	Invitrogen	D273	
Commercial assay or kit	BioTracker ATP-Red	Sigma Aldrich	SCT045	
Software, algorithm	GraphPad Prism 9.0.1			
Software, algorithm	ImageJ/Fiji			

805 ## *C. elegans* strains and maintenance

806 All strains used in this study are listed in Table S2. Hermaphrodites expressing germline
807 transgenes were maintained at 25°C to delay silencing. Mutants carrying the thermosensitive,
808 feminizing *fem-1(hc17ts*) allele, which causes cells that would normally become sperm instead
809 to become oocytes, were maintained at the permissive temperature of 15°C and moved to 25°C
810 for feminization prior to hatching, or at the L1 stage. Animals were grown under standard
811 laboratory conditions (Brenner, 1974) and maintained on Nematode Growth Medium (NGM)
812 seeded with OP50 bacteria, unless otherwise indicated.
813

814 ## Generation of *C. elegans* strains

815 **a. Strain generation: genetic crosses.**

816 The following *C. elegans* strains were created by standard genetic crosses: CF4542 *fem-*
817 *1(hc17ts) IV; ocfIs2[Ppie-1:mCherry::sp12::pie-1 3'UTR Cbr-unc-119(+)]*, CF4552 *tjIs1[Ppie-*
818 *1::gfp::rho-1 Cbr-unc-119(+)]; ocfIs2 [Ppie-1:mCherry::sp12::pie-1 3'UTR Cbr-unc-119(+)]*,
819 CF4557 *fem-1(hc17ts) IV; tjIs1[Ppie-1::gfp::rho-1 Cbr-unc-119(+)]; ocfIs2 [Ppie-*
820 *1:mCherry::sp12::pie-1 3'UTR Cbr-unc-119(+)]*, CF4559 *zuIs45[Pnmy-2::nmy-2::gfp Cbr-unc-*
821 *119(+)] V; ocfIs2 [Ppie-1:mCherry::sp12::pie-1 3'UTR Cbr-unc-119(+)]*, CF4560 *fem-1(hc17ts)*
822 *IV; zuIs45[Pnmy-2::nmy-2::gfp Cbr-unc-119(+)] V; ocfIs2 [Ppie-1:mCherry::sp12::pie-1 3'UTR*
823 *Cbr-unc-119(+)]* and CF4599 *sybSi35[Ppie-1::gfp::vha-13::vha-13 3'UTR Cbr-unc-119(+)] II;*
824 *unc-119(ed3/+) III; fem-1(hc17ts) IV*.

825 **b. Strain generation: Mos1-mediated single-copy insertion.**

826 The strains PHX1414 *sybSi35[Ppie-1::gfp::vha-13::vha-13 3'UTR Cbr-unc-119(+)] II; unc-*
827 *119(ed3) III* and PHX2690 *sybIs2690[Ppie-1::vha-7::wrmScarlet::vha-7 3'UTR Cbr-unc-119(+)]*
828 *I; unc-119(ed3) III* were generated by SunyBiotech using MosSCI services.
829

830 **c. Strain generation: CRISPR/Cas9-triggered homologous recombination**.

831 Split-wrmScarlet$_{11}$ was introduced at the C-terminus of KIN-19 using CRISPR/Cas9 and single-
832 stranded oligodeoxynucleotide template (ssODN) in the strain CF4582 expressing split-
833 wrmScarlet$_{1-10}$ in somatic tissues (driven by the *eft-3* promoter and *unc-54* 3'UTR), to obtain the
834 strain CF4609. CRISPR insertion of split-wrmScarlet$_{11}$ was performed following published
835 protocols (Goudeau et al., 2021; Paix et al., 2016, 2015). Briefly, ribonucleoprotein complexes
836 (protein Cas9, tracrRNA, crRNA) and ssODN were microinjected into the gonad of young adults
837 using standard methods (Evans, 2006). Injected worms were singled and placed at 25ºC
838 overnight. The crRNA and ssODN template sequences used to generate split-wrmScarlet$_{11}$
839 knock-in at the C terminus of *kin-19* are the following:

840 *ssDNA_kin-19C:*

841 ACAGGGAGCTACCGTTCCATCAGCTGGAGTTCCAGCTGGAGTTGCACCAGGAGGAACTAC
842 TCCACAGGGAGGAGGATCCTACACCGTCGTCGAGCAATACGAGAAGTCCGTCGCCCGTCA
843 CTGCACCGGAGGATAAgacgttttgttgccgtcctgaggctttttaatccaaaaaagcccatgttaaatcatgtactatc

844 *kin-19_C_crRNA:* GGCAACAAAACGTCTTACTG(TGG).

845 KIN-19::split-wrmScarlet$_{11}$ integrants were identified by screening for fluorescent progeny in the
846 progeny of injected worms, and the correct sequence insertion was confirmed by Sanger
847 sequencing (Genewiz).

848 Strains PHX731 *vha-13(syb731[wrmScarlet::vha-13]) V*, PHX1049 *vha-13(syb1049[gfp::vha-*
849 *13]) V*, PHX1198 *ieSi65[sun-1p::TIR1::sun-1 3'UTR + Cbr-unc-119(+)] II; unc-119(ed3) III; vha-*
850 *11(syb1198[vha-11::gfp::degron]/+) IV*, PHX1363 *vha-4(syb1363[wrmScarlet::vha-4]/+) II*, and
851 PHX1317 *vha-7(syb1317[vha-7::wrmScarlet]) IV* were generated by SunyBiotech using CRISPR
852 services for the Kenyon lab.

853

854 **d. Nucleic acid reagents.** Synthetic nucleic acids were purchased from Integrated DNA
855 Technologies (IDT). For split-wrmScarlet$_{11}$ knock-in, a 200-mer HDR template was ordered in
856 ssODN form (synthetic single-stranded oligodeoxynucleotide donors) from IDT.
857

858 ## RNA interference

859 Unless otherwise indicated, RNA interference was initiated in the early L4 larval stage, prior to
860 formation of oocytes but following much of development. One exception was *fem-1* RNAi, which
861 was initiated at hatching to ensure feminization. RNAi-bacterial feeding was initiated and
862 maintained for 36-40 hours prior to imaging to allow sufficient time for knockdown.
863

864 **a. Genome-wide screen**

865 The Ahringer *C. elegans* RNAi collection containing 18,225 bacterial clones, targeting around
866 87% of currently annotated *C. elegans* genes (Source BioScience), was used for screening. A
867 workflow for screening in liquid (Lehner et al., 2006) was modified suitably for our needs. For a
868 single 96-well plate, SA115 (GFP::RHO-1) hermaphrodites were grown on NGM plates seeded
869 with thick OP50 lawns (from 2 medium sized plates) for ~4 days to obtain a high density of
870 healthy and gravid young adults.
871 **Day 1:** Animals were subjected to standard bleaching and the eggs were washed thoroughly
872 and then incubated in M9 buffer overnight at 20°C on a rotating mixer to obtain synchronized
873 L1-arrested animals.
874 **Day 2:** L1 animals were transferred to NGM plates spotted with HT115 bacteria and incubated
875 24-28 hours at 25°C to reach the early L4 stage. The RNAi-library plate was aseptically
876 replicated into deep well plates (96-well, square; Greiner Bio-One) containing 1 mL LB (with 25
877 µg/ml carbenicillin and 12.5 µg/ml tetracycline) per well. Positive (*vha-13* and *atp-2*) and
878 negative (empty L4440 vector) controls were inoculated manually into blank wells if available, or

879 into wells on a separate control plate. The cultures were grown overnight at 37°C with shaking
880 (185 rpm).
881 **Day 3:** Fresh media (1 mL LB with 25 µg/ml carbenicillin) was added to the wells and incubated
882 at 37°C, 155 rpm for 2 hours. Subsequently, 4 mM isopropyl β-d-1-thiogalactopyranoside (IPTG;
883 Promega) was added to each RNAi well for induction of dsRNA synthesis and plates were
884 incubated for 3-4 hours at 30°C and 155 rpm. Synchronized L4 animals were washed off the
885 HT115 plates with M9 and resuspended in NGM broth (with 25 µg/ml carbenicillin and 1 mM
886 IPTG). This worm suspension (20 µL, ~10-15 animals) was added to each well of a Cellvis flat-
887 bottom glass plate with high performance #1.5 cover glass. The deep-well plate with dsRNA-
888 induced RNAi bacteria was centrifuged and the cells were resuspended in the same NGM broth
889 as the worms. 35 µL of each cell suspension was transferred into the corresponding well of the
890 Cellvis plate already seeded with L4 animals for bacterial RNAi feeding. The feeding plate was
891 incubated at 20°C, 155 rpm with adequate humidity in the shaker to prevent worms from settling
892 or drying out.
893 **Day 5:** After checking for the presence of adults with fully developed germlines, 25 mM sodium
894 azide (Sigma-Aldrich) was added to each well and the plate was subjected directly to imaging
895 on a spinning-disk confocal microscope. Typically, ~6 such 96-well plates were handled
896 simultaneously in a given round of screening. The presence of aggregates in 50% or more
897 animals for a specific RNAi condition was considered a hit.
898
899 *Notes:* The ability to automate image acquisition was complicated by a combination of low
900 GFP::RHO-1 reporter expression and the close apposition of gonads with the intestine, an
901 organ with significant autofluorescence. The density of animals and temperature of incubation
902 determine developmental rate and were optimized by multiple pilot trials. Liquid handling was
903 performed using Multidrop Combi from Thermo Scientific (initial inoculation of RNAi bacteria;
904 Day 2) and Agilent Bravo (resuspension and mixing of worms and induced bacteria; Day 3).

905 Following the validation rounds, the identities of the RNAi clones emerging from the screen
906 were verified by sequencing (Quintara Biosciences). Investigators were blinded to identity of
907 RNAi clones, except controls, during screening.
908
909 **b. RNAi feeding on agar plates**
910 Individual cultures were inoculated in tubes containing 1mL LB (with 25 µg/ml carbenicillin and
911 12.5 µg/ml tetracycline) and incubated at 37°C with shaking (200 rpm). The cultures were
912 diluted 1:10 in fresh LB containing only carbenicillin and allowed to grow for a further 2 hours,
913 after which IPTG was added (4 mM) and tubes moved to a 30°C shaker for dsRNA induction (3-
914 4 hours). Induced cultures were spotted on NGM plates containing 50 µg/ml carbenicillin and 2
915 mM IPTG and the bacterial lawn was allowed to grow for 24-36 hours at 30°C, prior to
916 introducing synchronized L4 animals.
917
918 **c. Somatic KIN-19::split-wrmScarlet and polyQ (Q35::YFP) protein-aggregation RNAi**
919 **screens**
920 KIN-19::split-wrmScarlet-expressing CF4609 animals were grown from a synchronized
921 population of L1 animals on HT115 bacteria until they reached the L4 stage and then were
922 transferred to plates seeded with RNAi bacteria until they reached day-2 of adulthood. Animals
923 treated with ESCRT-complex subunits were exposed to RNAi clones from the L1 larval stage
924 (Figure S19). The animals' heads were imaged by confocal microscopy. Z-stacks were analyzed
925 using ImageJ (Fiji); image manipulations consisted of maximum intensity projections of the
926 entire stack. The images of KIN-19::split-wrmScarlet puncta were quantified by the investigator
927 who acquired the images (Figure 6B), as well as by three blinded investigators (Figure S15).
928 AM140 animals expressing the polyQ reporter Q35::YFP in body wall muscles were
929 similarly synchronized and subjected to all assay-pool RNAi starting at the L4 larval stage. The
930 Q35::YFP reporter undergoes age-related aggregation starting on day-3 of adulthood; hence,

931 the animals were imaged on day-2. Germline GFP::RHO-1 aggregation in SA115 animals,
932 performed in parallel, was used as a control for successful gene knockdown. All positives from
933 the initial screen were subjected to a second validation round. The initial screen was performed
934 in liquid media in 96-well plates, and the validation was performed on regular NGM plates at
935 20ºC.
936

937 **Evaluation of screen hits and selection of 'assay pool' genes**

938 The initial whole-genome primary screen yielded 367 candidate genes, whose knockdown
939 starting at the L4 larval stage resulted in GFP::RHO-1-aggregate accumulation within oocytes of
940 young-adult hermaphrodites. False positives were eliminated by three independent rounds of
941 validation, again using the GFP::RHO-1 strain, in which all candidates were subjected to the
942 same workflow as the primary screen. The validation rounds were performed in a blinded
943 fashion by two independent experimentalists and included the positive controls *vha-13* and *atp-*
944 *2* RNAi (Bohnert and Kenyon, 2017). A candidate was considered to be positive if aggregation
945 was observed in >50% animals in at least two out of the three rounds of validation. This led to
946 the confirmation of 88 candidates required for preventing GFP::RHO-1 aggregation in the
947 hermaphrodite germline. Next, we randomly selected 55 candidates (ensuring representation of
948 all the GO categories in Figure 1D, as well as each individual orphan candidate) and subjected
949 them to orthogonal verification using the NMY-2::GFP reporter. If the representative candidates
950 from a particular GO category tested positive in this round of screening, the entire category was
951 considered confirmed. Finally, we discarded candidates that were a) known to be required for
952 male gonad development or spermatogenesis, b) non-specific RNAi targets or c) known targets
953 of the RHO-1 protein; and thereby confirmed 81 verified genes from the screen (Figure 1C).
954 Notably, our analysis did not allow the identification of false negatives and we manually tested
955 some genes that we thought might be involved in the pathway (e.g., TOR pathway genes and
956 ESCRT-complex subunits).

957 For selecting the ‘assay pool’ of genes used in all further phenotypic screens, we picked
958 candidates from each GO category that were associated with consistent GFP::RHO-1
959 aggregation, with intermediate to strong phenotypes. In categories such as translation or protein
960 degradation, we specifically included at least one candidate of small and large ribosomal
961 subunits or structural and regulatory proteasomal subunits, respectively. Similarly, in the actin
962 cytoskeletal category, we ensured that both structural and regulatory genes were included. No
963 other specific criteria were used to avoid any bias in candidate selection. All confirmed orphans
964 were included in the assay pool without any further selection.
965
966
967 **Fluorescence Microscopy**
968 Confocal fluorescence images were acquired on a Nikon Eclipse Ti CSU-X1 equipped with 405,
969 488, 561 and 640 nm lasers. Emission was collected through 455/50, 525/36, 605/70 or 700/75
970 nm filters on an Andor iXon Ultra EMCCD camera, using the NIS-Elements software. Images
971 were visualized using ImageJ Fiji. Maintenance and selection of transgenic worms expressing
972 fluorescent markers were performed using a Leica M165 FC fluorescent stereo microscope
973 equipped with a Sola SE-V light source. Photobleaching and wide-field experiments were
974 performed using a Leica TIRF microscope equipped with an infinity scanner, using 488 nm laser
975 excitation. Emission was collected through a GFP-T filter cube on a Hamamatsu ORCA-Flash4
976 camera.
977
978 **a. Preparing worms for microscopy**
979 Worms imaged in 96-well plates were immobilized by adding sodium azide to the liquid medium
980 at a concentration of 25 mM (except when measuring mitochondrial ΔΨ, where the medium was
981 carefully removed, and animals immobilized with levamisole). For all other experiments, animals

982 were picked from plates and placed in a drop of 2 mM levamisole (Sigma) on a 4% agarose pad
983 resting on a glass slide, and then secured with a coverslip.
984
985 **b. Dye staining**
986 For experiments involving several different RNAi-knockdown conditions, RNAi feeding was set
987 up similar to the screen workflow. The dyes LysoTracker Red DND-99 and DiOC6(3) (2 μM) and
988 BioTracker ATP-Red (8 μM) were added to the liquid NGM prior to resuspension of dsRNA-
989 induced RNAi-bacterial cells. After addition of synchronized L4 animals, feeding and dye uptake
990 were allowed to proceed at 20°C for 36-40 hours. The 96-well feeding plates were protected
991 from light during this time. The plate was centrifuged, bacterial suspensions were carefully
992 washed off, and the animals were resuspended in fresh M9 buffer for imaging. For experiments
993 involving fewer knockdown conditions or pairwise comparisons between hermaphrodites and
994 females, the dye-feeding was performed on NGM Agar plates as described previously (Bohnert
995 and Kenyon, 2017).
996 To analyze lysosome acidification in maturing oocytes, the ratio of signal intensities
997 between proximal oocytes and the distal germline were calculated. In case of intestinal
998 LysoTracker staining, signal intensities were not measured due to highly variable dye uptake
999 and staining; and signal skewness (inhomogeneity) was measured instead. In both cases,
1000 multiple regions of oocytes or the anterior intestine were sampled for intensity or skewness
1001 values, and averaged for a single animal.
1002
1003 **c. Analysis of skewness**
1004 For semi-quantitatively analyzing the presence of GFP::VHA-13 puncta in oocytes and
1005 LysoTracker-stained puncta within the intestine, we measured skewness of the fluorescence
1006 signal. Skewness; that is, degree of symmetry or homogeneity of the signal, indicative of distinct
1007 lysosomal localization, was utilized as an alternative to counting GFP::VHA-13 puncta in

1008 individual oocytes or acidic LysoTracker-stained intestinal granules. Skewness was measured
1009 using the inbuilt function in Fiji (Analyze > Measure > Skewness). A skewness value of zero
1010 represents homogenous signal or lack of distinct puncta. For both GFP::VHA-13 and intestinal
1011 LysoTracker staining, skewness values were measured for multiple different regions and the
1012 mean value was reported for an individual animal.
1013
1014 **d. Imaging oocyte ATP levels using a FRET-based sensor**
1015 The *pie-1* promoter, the AT1.03 ATP-sensor (Imamura et al., 2009) containing two introns
1016 (codon optimized for *C. elegans*), and the *tbb-2* 3'UTR sequences were cloned into pUC57.
1017 Germline gene expression was achieved using a microinjection-based protocol with diluted
1018 transgenic DNA (Kelly et al., 1997). The *Ppie-1::AT1.03::tbb-2* 3'UTR construct (5 ng/μL) was
1019 co-injected with PvuII-digested genomic DNA fragments from *E. coli* (100 ng/μL), and pRF4 (20
1020 ng/μL) was used as a co-injection marker. Young N2E hermaphrodites were placed at 25°C
1021 after injection, and progeny were inspected for sensor expression 48 hours later. Larvae
1022 expressing the sensor were picked and transferred to RNAi feeding plates (clones targeting
1023 ETC genes) and allowed to grow until Day 2 of adulthood before imaging.
1024 Imaging was performed on a wide-field DMI-8 equipped with a spectra-x light source using
1025 427/10 or 510/10 excitation filters and a 40X/0.85 objective. Emission was collected through
1026 475/20 or 540/21 emission filters using an FF444/520/590 dichroic and pco.edge 4.2 camera.
1027 For analysis, FRET-channel images were divided by donor-channel images using ImageJ Fiji
1028 after subtracting a background estimated from non-fluorescent worms and masked using the
1029 fluorescence from the acceptor image.
1030
1031
1032

1033 **Mating experiments**

1034 An individual female animal was immobilized on an agarose pad using 2 mM levamisole, and
1035 the reporter of interest was imaged in the anterior gonad arm. Levamisole was washed off
1036 immediately, and the animal was introduced to an NGM plate containing young CB1490 male
1037 animals in a small spot of OP50 bacteria (5 males:1 female). The interactions were monitored
1038 using a benchtop stereo microscope and when mating occurred, the female was transferred
1039 immediately to the agarose pad and imaged again, ensuring that the same oocytes were
1040 visualized before and after mating. Successful mating events were tracked by gonadal sheath
1041 contractions in response to sperm and subsequently confirmed by successful ovulation.
1042 Changes within individual oocytes upon mating were monitored up to 90 minutes at 10-minute
1043 intervals. An identical procedure was performed for control females, except for exposure to
1044 males. Specific regions within proximal oocytes of control female animals were compared at all
1045 time points to determine the extent of signal intensity change due to photobleaching, with
1046 increasing time (Figure S6B). In addition, regions of the distal germline were also monitored in
1047 mated animals (data not shown) to verify that the disappearance of the signal representing ER
1048 clusters and protein aggregates was not due to photobleaching.

1049

1050

1051 **KIN-19::split-wrmScarlet aggregate accumulation in somatic tissues**

1052 A synchronized population of KIN-19::split-wrmScarlet-expressing CF4609 animals were grown
1053 on OP50 from L1 at 20°C. Worms were transferred every other day to freshly-seeded NGM
1054 plates to remove progeny. Worms were imaged by confocal microscopy at day-1, day-4, day-7
1055 and day-11 of adulthood.

1056

1057

1058 **Transmission electron microscopy**

1059 N2E hermaphrodites and *fem-1(hc17ts)* females were cultured for five generations at 15°C
1060 without starvation or contamination at any point. Animals from 12 small plates of each strain
1061 were bleached, and the synchronized eggs were collected and washed thoroughly in M9 and
1062 strained through 40 µm strainers to remove adult carcasses. Eggs were then resuspended in
1063 fresh M9 and incubated at 25°C overnight on a rotating mixer. Synchronized L1 animals were
1064 moved to NGM plates seeded with OP50 and incubated at 25°C (~50 animals per plate). Newly-
1065 developed day-1 adults were further processed according to standard *C. elegans* TEM
1066 techniques (Hall et al., 2012). Briefly, the animals were loaded into 100 µm-deep specimen
1067 carriers and high-pressure frozen in a Bal-tec HPM (approximately 20 worms per carrier). After
1068 freezing, the carriers were transferred to vials containing Freeze Substitution (FS) media (1%
1069 OsO4 and 0.1% uranyl acetate in acetone), while still submerged in liquid N_2. Frozen samples
1070 were slowly warmed to approximately -15°C while being agitated on a rotating platform (adapted
1071 from (McDonald and Webb, 2011)). Following freeze substitution, samples were infiltrated with
1072 Epon Resin/Acetone series [25% Resin (1hr), 50% Resin (1hr), 75% Resin (overnight), 100%
1073 resin (1hr), 100% resin (1hr) and the resin from last step replaced with fresh resin for
1074 embedding] and subjected to polymerization at 60°C for 48 hours. For staining, thin sections (70
1075 nm thick) were cut on an ultramicrotome, picked up on Formvar-coated 50 mesh grids and post-
1076 stained for 7 min in 2% uranyl acetate (aq), followed by 7 min in lead citrate. Images were
1077 acquired on a Tecnai 12 Transmission Electron Microscope.

1078

1079

1080 **Quantitative real-time PCR**

1081 CF4609 animals treated with *vps-20* RNAi, *vps-54* RNAi or empty-vector control were recovered
1082 after imaging, collected in Eppendorf DNA LoBind tube with 10µL of Cells-to-Ct lysis buffer

1083 supplemented with DNase I (Thermo Fisher Scientific) and placed at -80°C for 30 min. Tubes
1084 were thawed on ice and processed on a bead-beater for 30 sec at 4°C. Worm lysates were
1085 incubated at room temperature for 10 min, and lysis was stopped by adding 2µL of Stop Buffer
1086 from the Cells-to-Ct kit. Samples were then incubated at 95°C, 5 min. cDNAs were synthesized
1087 from RNA templates using a reverse transcription mix following the manufacturers' instructions.
1088 qPCR was carried out on an QuantStudio™ 6 Flex Real-Time PCR System using a SYBR
1089 green-based real-time kit (Kapa Biosystems). The RNA polymerase II subunit *ama-1* was used
1090 as the house-keeping control. The qPCR primers were as follows:
1091 *vps-20* [TCCGATCAGGATAATGCGATTT]/[AGCGCCTGGAATTACCAAA];
1092 *vps-54* [TTCACTCTTCACAGGTGAGTTC]/[CCTGTGATCTACATGATTCTCTCTC];
1093 *ama-1* [GACGAGTCCAACGTACTCTCCAAC]/[TACTTGGGGCTCGATGGGC].
1094
1095
1096 **Data analysis and statistics**
1097 ImageJ Fiji was used to quantify and analyze attributes from image data, and images from a
1098 given experimental set were scaled and processed identically for comparison. Preparation of
1099 graphs and statistical analyses were performed using GraphPad Prism 8. Statistical tests used
1100 to determine significance and p-values are described in the figure legends of each experiment.
1101 Each violin plot representation includes the median and quartiles, and distributions in bar graphs
1102 represent mean +/- standard deviation. Figures displaying numerical values obtained by
1103 analysis of microscopy images of dye-stained worms report the average of multiple independent
1104 values (technical replicates) from individual animals (biological replicates), each of which are
1105 represented as data points. Experiments reporting qualitative phenotypes from microscopy
1106 images were performed at least three times (independently) with 10-15 animals per condition in
1107 each individual experiment (except the primary screen which was done only once but validated

1108 in three independent experiments). For all other cases, sample sizes and replicates are included
1109 in the corresponding figure legends. No statistical methods were used to predetermine sample
1110 sizes. Investigators were blinded to identity of RNAi clones (except for controls) while imaging
1111 multiple knockdown conditions in 96-well plates.
1112
1113
1114
1115 **References:**

1116 Baxi K, Ghavidel A, Waddell B, Harkness TA, de Carvalho CE. 2017. Regulation of
1117 lysosomal function by the daf-16 forkhead transcription factor couples reproduction to
1118 aging in caenorhabditis elegans. *Genetics*. doi:10.1534/genetics.117.204222
1119 Ben-Zvi A, Miller EA, Morimoto RI. 2009. Collapse of proteostasis represents an early
1120 molecular event in Caenorhabditis elegans aging. *Proc Natl Acad Sci U S A*.
1121 doi:10.1073/pnas.0902882106
1122 Bluemink JG, Hage WJ, van den Hoef MH, Dictus WJ. 1983. Freeze-fracture electron
1123 microscopy of membrane changes in progesterone-induced maturing oocytes and
1124 eggs of Xenopus laevis. *Eur J Cell Biol*.
1125 Bohnert KA, Kenyon C. 2017. A lysosomal switch triggers proteostasis renewal in the
1126 immortal C. Elegans germ lineage. *Nature* **551**:629–633. doi:10.1038/nature24620
1127 Brenner S. 1974. The genetics of Caenorhabditis elegans. *Genetics*.
1128 Carroll J, Jones KT, Whittingham DG. 1996. Ca2+ release and the development of Ca2+
1129 release mechanisms during oocyte maturation: A prelude to fertilization. *Rev Reprod*
1130 **1**:137–143. doi:10.1530/ror.0.0010137

1131 Charbonneau M, Grey RD. 1984. The onset of activation responsiveness during maturation
1132 coincides with the formation of the cortical endoplasmic reticulum in oocytes of
1133 Xenopus laevis. *Dev Biol*. doi:10.1016/0012-1606(84)90177-5
1134 Crittenden SL, Troemel ER, Evans TC, Kimble J. 1994. GLP-1 is localized to the mitotic
1135 region of the C. elegans germ line. *Development* **120**:2901–2911.
1136 David DC, Ollikainen N, Trinidad JC, Cary MP, Burlingame AL, Kenyon C. 2010.
1137 Widespread protein aggregation as an inherent part of aging in C. elegans. *PLoS Biol*
1138 **8**:47–48. doi:10.1371/journal.pbio.1000450
1139 Dillin A, Hsu AL, Arantes-Oliveira N, Lehrer-Graiwer J, Hsin H, Fraser AG, Kamath RS,
1140 Ahringer J, Kenyon C. 2002. Rates of behavior and aging specified by mitochondrial
1141 function during development. *Science (80-)*. doi:10.1126/science.1077780
1142 Evans T. 2006. Transformation and microinjection. *WormBook*.
1143 doi:10.1895/wormbook.1.108.1
1144 Fan W, Waymire KG, Narula N, Li P, Rocher C, Coskun PE, Vannan MA, Narula J,
1145 MacGregor GR, Wallace DC. 2008. A mouse model of mitochondrial disease reveals
1146 germline selection against severe mtDNA mutations. *Science (80-)*.
1147 doi:10.1126/science.1147786
1148 FitzHarris G, Marangos P, Carroll J. 2007. Changes in endoplasmic reticulum structure
1149 during mouse oocyte maturation are controlled by the cytoskeleton and cytoplasmic
1150 dynein. *Dev Biol* **305**:133–144. doi:10.1016/j.ydbio.2007.02.006
1151 Francis R, Barton M, Kimble J, Schedl T. 1995. gld-1, a tumor suppressor gene required
1152 for oocyte development in Caenorhabditis elegans. *Genetics* **139**:579–606.
1153 Fredriksson Å, Johansson Krogh E, Hernebring M, Pettersson E, Javadi A, Almstedt A,
1154 Nyström T. 2012. Effects of aging and reproduction on protein quality control in soma
1155 and gametes of Drosophila melanogaster. *Aging Cell*. doi:10.1111/j.1474-
1156 9726.2012.00823.x

1157 Gawriluk TR, Hale AN, Flaws JA, Dillon CP, Green DR, Rucker EB. 2011. Autophagy is a
1158 cell survival program for female germ cells in the murine ovary. *Reproduction*.
1159 doi:10.1530/REP-10-0489
1160 Goudeau J, Aguilaniu H. 2010. Carbonylated proteins are eliminated during reproduction in
1161 C. elegans. *Aging Cell* **9**:991–1003. doi:10.1111/j.1474-9726.2010.00625.x
1162 Goudeau J, Samaddar M, Bohnert KA, Kenyon C. 2020. Addendum: A lysosomal switch
1163 triggers proteostasis renewal in the immortal C. elegans germ lineage. *Nature*
1164 **580**:2020. doi:10.1038/s41586-020-2108-0
1165 Goudeau J, Sharp CS, Paw J, Savy L, Leonetti MD, York AG, Updike DL, Kenyon C,
1166 Ingaramo M. 2021. Split-wrmScarlet and split-sfGFP: Tools for faster, easier
1167 fluorescent l abeling of endogenous proteins in Caenorhabditis elegans . *Genetics*.
1168 doi:10.1093/genetics/iyab014
1169 Graham LA, Hill KJ, Stevens TH. 1998. Assembly of the Yeast Vacuolar H+-ATPase
1170 Occurs in the Endoplasmic Reticulum and Requires a Vma12p/Vma22p Assembly
1171 Complex. *J Cell Biol* **142**:39–49.
1172 Hall DH, Hartwieg E, Nguyen KCQ. 2012. Modern Electron Microscopy Methods for C.
1173 elegansMethods in Cell Biology. Academic Press Inc. pp. 93–149. doi:10.1016/B978-
1174 0-12-394620-1.00004-7
1175 Huang C, Wagner-Valladolid S, Stephens AD, Jung R, Poudel C, Sinnige T, Lechler MC,
1176 Schörit N, Lu M, Laine RF, Michel CH, Vendruscolo M, Kaminski CF, Schierle GSK,
1177 David DC. 2019. Intrinsically aggregation-prone proteins form amyloid-like aggregates
1178 and contribute to tissue aging in caenorhabditis elegans. *Elife*.
1179 doi:10.7554/eLife.43059
1180 Hubbard EJA, Greenstein D. 2005. Introduction to the germ line. *WormBook*.
1181 doi:10.1895/wormbook.1.18.1

1182 Huelgas-Morales G, Greenstein D. 2018. Control of oocyte meiotic maturation in C.
1183 elegans. *Semin Cell Dev Biol*. doi:10.1016/j.semcdb.2017.12.005
1184 Hughes AL, Gottschling DE. 2012. An early age increase in vacuolar pH limits
1185 mitochondrial function and lifespan in yeast. *Nature* **492**:261–265.
1186 doi:10.1038/nature11654
1187 Hunter N. 2017. Oocyte Quality Control: Causes, Mechanisms, and Consequences. *Cold*
1188 *Spring Harb Symp Quant Biol* **82**:235–247. doi:10.1101/sqb.2017.82.035394
1189 Imamura H, Huynh Nhat KP, Togawa H, Saito K, Iino R, Kato-Yamada Y, Nagai T, Noji H.
1190 2009. Visualization of ATP levels inside single living cells with fluorescence resonance
1191 energy transfer-based genetically encoded indicators. *Proc Natl Acad Sci U S A*
1192 **106**:15651–15656. doi:10.1073/pnas.0904764106
1193 Jones AR, Francis R, Schedl T. 1996. GLD-1, a cytoplasmic protein essential for oocyte
1194 differentiation, shows stage- ans sex-specific expression during Caenorhabditis
1195 elegans germline development. *Dev Biol*. doi:10.1006/dbio.1996.0293
1196 Joseph-Strauss D, Gorjánácz M, Santarella-Mellwig R, Voronina E, Audhya A, Cohen-Fix
1197 O. 2012. Sm protein down-regulation leads to defects in nuclear pore complex
1198 disassembly and distribution in C. elegans embryos. *Dev Biol* **365**:445–457.
1199 doi:10.1016/j.ydbio.2012.02.036
1200 Kamath RS, Fraser AG, Dong Y, Poulin G, Durbin R, Gotta M, Kanapin A, Le Bot N,
1201 Moreno S, Sohrmann M, Welchman DP, Zipperien P, Ahringer J. 2003. Systematic
1202 functional analysis of the Caenorhabditis elegans genome using RNAi. *Nature*
1203 **421**:231–237. doi:10.1038/nature01278
1204 Kelly WG, Xu SQ, Montgomery MK, Fire A. 1997. Distinct requirements for somatic and
1205 germline expression of a generally expressed Caenorhabditis elegans gene. *Genetics*
1206 **146**:227–238. doi:10.1093/genetics/146.1.227

1207 Kim S, Spike C, Greenstein D. 2013. Control of oocyte growth and meiotic maturation in
1208 caenorhabditis elegans. *Adv Exp Med Biol* **757**:277–320. doi:10.1007/978-1-4614-
1209 4015-4-10
1210 King GA, Goodman JS, Schick JG, Chetlapalli K, Jorgens DM, McDonald KL, Ünal E.
1211 2019. Meiotic cellular rejuvenation is coupled to nuclear remodeling in budding yeast.
1212 *Elife* **8**. doi:10.7554/eLife.47156
1213 Kisielnicka E, Minasaki R, Eckmann CR. 2018. MAPK signaling couples SCF-mediated
1214 degradation of translational regulators to oocyte meiotic progression. *Proc Natl Acad*
1215 *Sci U S A* **115**:E2772–E2781. doi:10.1073/pnas.1715439115
1216 Kobayashi H, Minshull J, Ford C, Golsteyn R, Poon R, Hunt T. 1991. On the synthesis and
1217 destruction of A- and B-type cyclins during oogenesis and meiotic maturation in
1218 Xenopus laevis. *J Cell Biol*. doi:10.1083/jcb.114.4.755
1219 Kosinki M, McDonald K, Schwartz J, Yamamoto I, Greenstein D. 2005. C. elegans sperm
1220 bud vesicles to deliver a meiotic maturation signal to distant oocytes. *Development*
1221 **132**:3357–3369. doi:10.1242/dev.01916
1222 Langerak S, Trombley A, Patterson JR, Leroux D, Couch A, Wood MP, Schisa JA. 2019.
1223 Remodeling of the endoplasmic reticulum in Caenorhabditis elegans oocytes is
1224 regulated by CGH-1. *Genesis* **57**:1–8. doi:10.1002/dvg.23267
1225 Lapierre LR, De Magalhaes Filho CD, McQuary PR, Chu CC, Visvikis O, Chang JT, Gelino
1226 S, Ong B, Davis AE, Irazoqui JE, Dillin A, Hansen M. 2013. The TFEB orthologue
1227 HLH-30 regulates autophagy and modulates longevity in Caenorhabditis elegans. *Nat*
1228 *Commun* **4**. doi:10.1038/ncomms3267
1229 Lee SS, Lee RYN, Fraser AG, Kamath RS, Ahringer J, Ruvkun G. 2003. A systematic
1230 RNAi screen identifies a critical role for mitochondria in C. elegans longevity. *Nat*
1231 *Genet*. doi:10.1038/ng1056

1232 Lehner B, Tischler J, Fraser AG. 2006. RNAi screens in Caenorhabditis elegans in a 96-
1233 well liquid format and their application to the systematic identification of genetic
1234 interactions. *Nat Protoc* **1**:1617–1620. doi:10.1038/nprot.2006.245
1235 Llorca O, Martín-Benito J, Ritco-Vonsovici M, Grantham J, Hynes GM, Willison KR,
1236 Carrascosa JL, Valpuesta JM. 2000. Eukaryotic chaperonin CCT stabilizes actin and
1237 tubulin folding intermediates in open quasi-native conformations. *EMBO J* **19**:5971–
1238 5979. doi:10.1093/emboj/19.22.5971
1239 Luo S, Kleemann GA, Ashraf JM, Shaw WM, Murphy CT. 2010. TGF-β and Insulin
1240 Signaling Regulate Reproductive Aging via Oocyte and Germline Quality
1241 Maintenance. *Cell* **143**:299–312. doi:10.1016/j.cell.2010.09.013
1242 Maller J, Wu M, Gerhart JC. 1977. Changes in protein phosphorylation accompanying
1243 maturation of Xenopus laevis oocytes. *Dev Biol*. doi:10.1016/0012-1606(77)90093-8
1244 McCarter J, Bartlett B, Dang T, Schedl T. 1999. On the Control of Oocyte Meiotic
1245 Maturation and Ovulation in Caenorhabditis elegans.
1246 McDonald KL, Webb RI. 2011. Freeze substitution in 3 hours or less. *J Microsc* **243**:227–
1247 33. doi:10.1111/j.1365-2818.2011.03526.x
1248 Mehlmann LM, Terasaki M, Jaffe LA, Kline D. 1995. Reorganization of the endoplasmic
1249 reticulum during meiotic maturation of the mouse oocyte.
1250 Miller MA, Nguyen VQ, Lee MH, Kosinski M, Schedl T, Caprioli RM, Greenstein D. 2001. A
1251 sperm cytoskeletal protein that signals oocyte meiotic maturation and ovulation.
1252 *Science (80-)* **291**:2144–2147. doi:10.1126/science.1057586
1253 Miller MA, Ruest PJ, Kosinski M, Hanks SK, Greenstein D. 2003. An Eph receptor sperm-
1254 sensing control mechanism for oocyte meiotic maturation in Caenorhabditis elegans.
1255 *Genes Dev* **17**:187–200. doi:10.1101/gad.1028303
1256 Morley JF, Brignull HR, Weyers JJ, Morimoto RI. 2002. The threshold for polyglutamine-
1257 expansion protein aggregation and cellular toxicity is dynamic and influenced by aging

1258 in Caenorhabditis elegans. *Proc Natl Acad Sci U S A* **99**:10417–10422.
1259 doi:10.1073/pnas.152161099
1260 O'Rourke EJ, Ruvkun G. 2013. MXL-3 and HLH-30 transcriptionally link lipolysis and
1261 autophagy to nutrient availability. *Nat Cell Biol* **15**:668–676. doi:10.1038/ncb2741
1262 Paix A, Folkmann A, Rasoloson D, Seydoux G. 2015. High efficiency, homology-directed
1263 genome editing in Caenorhabditis elegans using CRISPR-Cas9ribonucleoprotein
1264 complexes. *Genetics*. doi:10.1534/genetics.115.179382
1265 Paix A, Schmidt H, Seydoux G. 2016. Cas9-assisted recombineering in C. elegans:
1266 Genome editing using in vivo assembly of linear DNAs. *Nucleic Acids Res* **44**:e128.
1267 doi:10.1093/nar/gkw502
1268 Poteryaev D, Squirrell JM, Campbell JM, White JG, Spang A. 2005. Involvement of the
1269 Actin Cytoskeleton and Homotypic Membrane Fusion in ER Dynamics in
1270 Caenorhabditis elegans □ V. *Mol Biol Cell* **16**:2139–2153. doi:10.1091/mbc.E04
1271 Qiao H, Rao HBDP, Yun Y, Sandhu S, Fong JH, Sapre M, Nguyen M, Tham A, Van BW,
1272 Chng TYH, Lee A, Hunter N. 2018. Impeding DNA Break Repair Enables Oocyte
1273 Quality Control. *Mol Cell* **72**:211-221.e3. doi:10.1016/j.molcel.2018.08.031
1274 Reis-Rodrigues P, Czerwieniec G, Peters TW, Evani US, Alavez S, Gaman EA, Vantipalli
1275 M, Mooney SD, Gibson BW, Lithgow GJ, Hughes RE. 2012. Proteomic analysis of
1276 age-dependent changes in protein solubility identifies genes that modulate lifespan.
1277 *Aging Cell*. doi:10.1111/j.1474-9726.2011.00765.x
1278 Roux AE, Langhans K, Huynh W, Kenyon C. 2016. Reversible Age-Related Phenotypes
1279 Induced during Larval Quiescence in C. Elegans. *Cell Metab*.
1280 doi:10.1016/j.cmet.2016.05.024
1281 Sahu R, Kaushik S, Clement CC, Cannizzo ES, Scharf B, Follenzi A, Potolicchio I, Nieves
1282 E, Cuervo AM, Santambrogio L. 2011. Microautophagy of Cytosolic Proteins by Late
1283 Endosomes. *Dev Cell*. doi:10.1016/j.devcel.2010.12.003

1284 Schumacher B, Hofmann K, Boulton S, Gartner A. 2001. The C. elegans homolog of the
1285 p53 tumor suppressor is required for DNA damage-induced apoptosis. *Curr Biol*.
1286 doi:10.1016/S0960-9822(01)00534-6
1287 Shirayama M, Seth M, Lee HC, Gu W, Ishidate T, Conte D, Mello CC. 2012. PiRNAs
1288 initiate an epigenetic memory of nonself RNA in the C. elegans germline. *Cell*.
1289 doi:10.1016/j.cell.2012.06.015
1290 Spike CA, Huelgas-Morales G, Tsukamoto T, Greenstein D. 2018. Multiple mechanisms
1291 inactivate the LIN-41 RNA-binding protein to ensure a robust oocyte-to-embryo
1292 transition in caenorhabditis elegans. *Genetics* **210**:1011–1037.
1293 doi:10.1534/genetics.118.301421
1294 Sun Y, Li M, Zhao D, Li X, Yang C, Wang X. 2020. Lysosome activity is modulated by
1295 multiple longevity pathways and is important for lifespan extension in C. elegans.
1296 *Elife*. doi:10.7554/eLife.55745
1297 Taylor RC, Dillin A. 2011. Aging as an event of proteostasis collapse. *Cold Spring Harb*
1298 *Perspect Biol*. doi:10.1101/cshperspect.a004440
1299 Ünal E, Kinde B, Amon A. 2011. Gametogenesis eliminates age-induced cellular damage
1300 and resets life span in yeast. *Science (80-)* **332**:1554–1557.
1301 doi:10.1126/science.1204349
1302 Walther DM, Kasturi P, Zheng M, Pinkert S, Vecchi G, Ciryam P, Morimoto RI, Dobson
1303 CM, Vendruscolo M, Mann M, Hartl FU. 2015. Widespread proteome remodeling and
1304 aggregation in aging C. elegans. *Cell*. doi:10.1016/j.cell.2015.03.032
1305 Wasserman WJ, Richter JD, Smith LD. 1982. Protein synthesis during maturation
1306 promoting factor- and progesterone-induced maturation in Xenopus oocytes. *Dev Biol*.
1307 doi:10.1016/0012-1606(82)90303-7
1308 Williams RL, Urbé S. 2007. The emerging shape of the ESCRT machinery. *Nat Rev Mol*
1309 *Cell Biol*. doi:10.1038/nrm2162

1310 Wright JE, Gaidatzis D, Senften M, Farley BM, Westhof E, Ryder SP, Ciosk R. 2011. A
1311 quantitative RNA code for mRNA target selection by the germline fate determinant
1312 GLD-1. *EMBO J* **30**:533–545. doi:10.1038/emboj.2010.334
1313 Yamashita YM. 2018. Subcellular specialization and organelle behavior in germ cells.
1314 *Genetics* **208**:19–51. doi:10.1534/genetics.117.300184
1315 Zhang H, Alsaleh G, Feltham J, Sun Y, Napolitano G, Riffelmacher T, Charles P, Frau L,
1316 Hublitz P, Yu Z, Mohammed S, Ballabio A, Balabanov S, Mellor J, Simon AK. 2019.
1317 Polyamines Control eIF5A Hypusination, TFEB Translation, and Autophagy to
1318 Reverse B Cell Senescence. *Mol Cell* **76**:110-125.e9.
1319 doi:10.1016/j.molcel.2019.08.005
1320 Zou L, Wu D, Zang X, Wang Z, Wu Z, Chen D. 2019. Construction of a germline-specific
1321 RNAi tool in C. elegans. *Sci Rep* **9**:1–10. doi:10.1038/s41598-019-38950-8

Figure S1

A

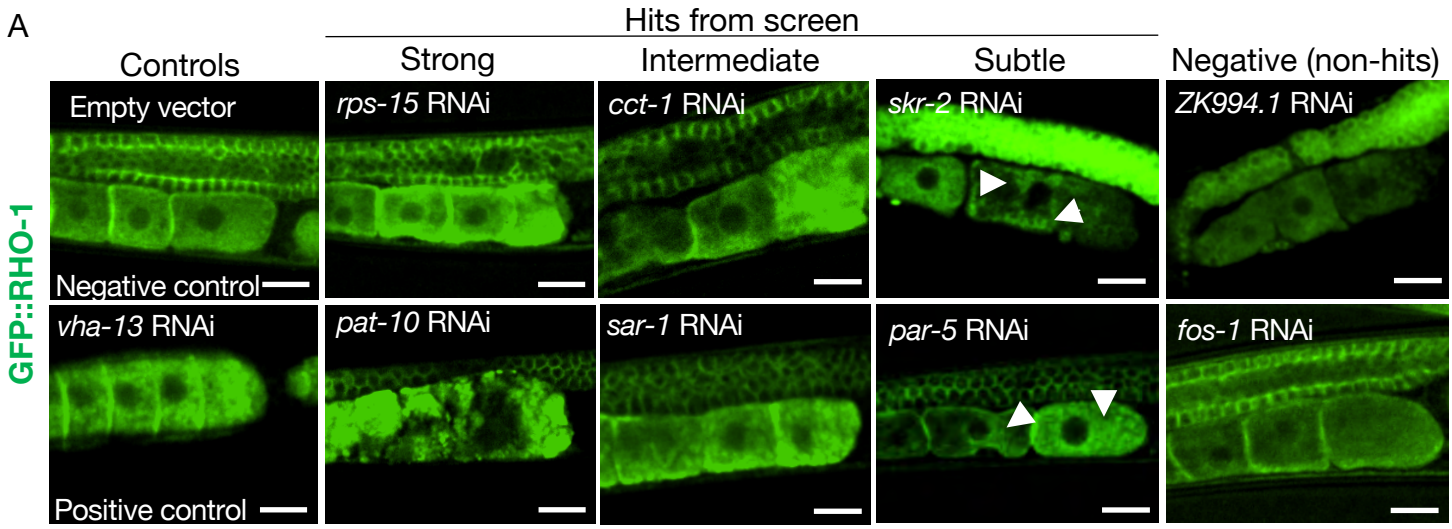

B

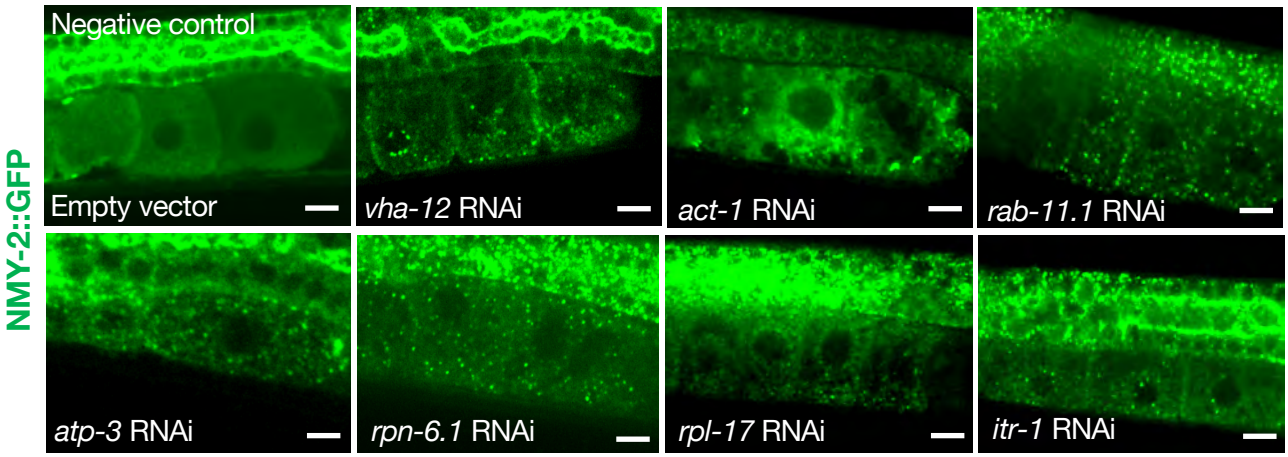

C

GO biological process	Fold enrichment	P-value
Translation	5.01	5.53E-08
ATP-hydrolysis coupled proton transport	27.17	3.76E-08
Ovulation	13.66	6.19E-05
RNA processing	3.26	3.22E-05
Cortical actin cytoskeleton organization	20.11	7.73E-04
Vacuolar acidification	24.58	4.77E-04

Figure S1.

(A) RNAi clones causing GFP::RHO-1 aggregates in hermaphrodite oocytes (SA115), visualized at low magnification (20X objective) during primary screening. Scale bars, 20 μm; white arrows, GFP::RHO-1 aggregates in subtle hits. (B) Examples of NMY-2::GFP aggregates in oocytes of hermaphrodites (JJ1473) undergoing orthogonal verification with a different aggregation-prone protein. Scale bars,10 μm. (C) The highest enriched gene-ontology (GO) process categories represented by the validated genes identified in the screen.

Figure S2

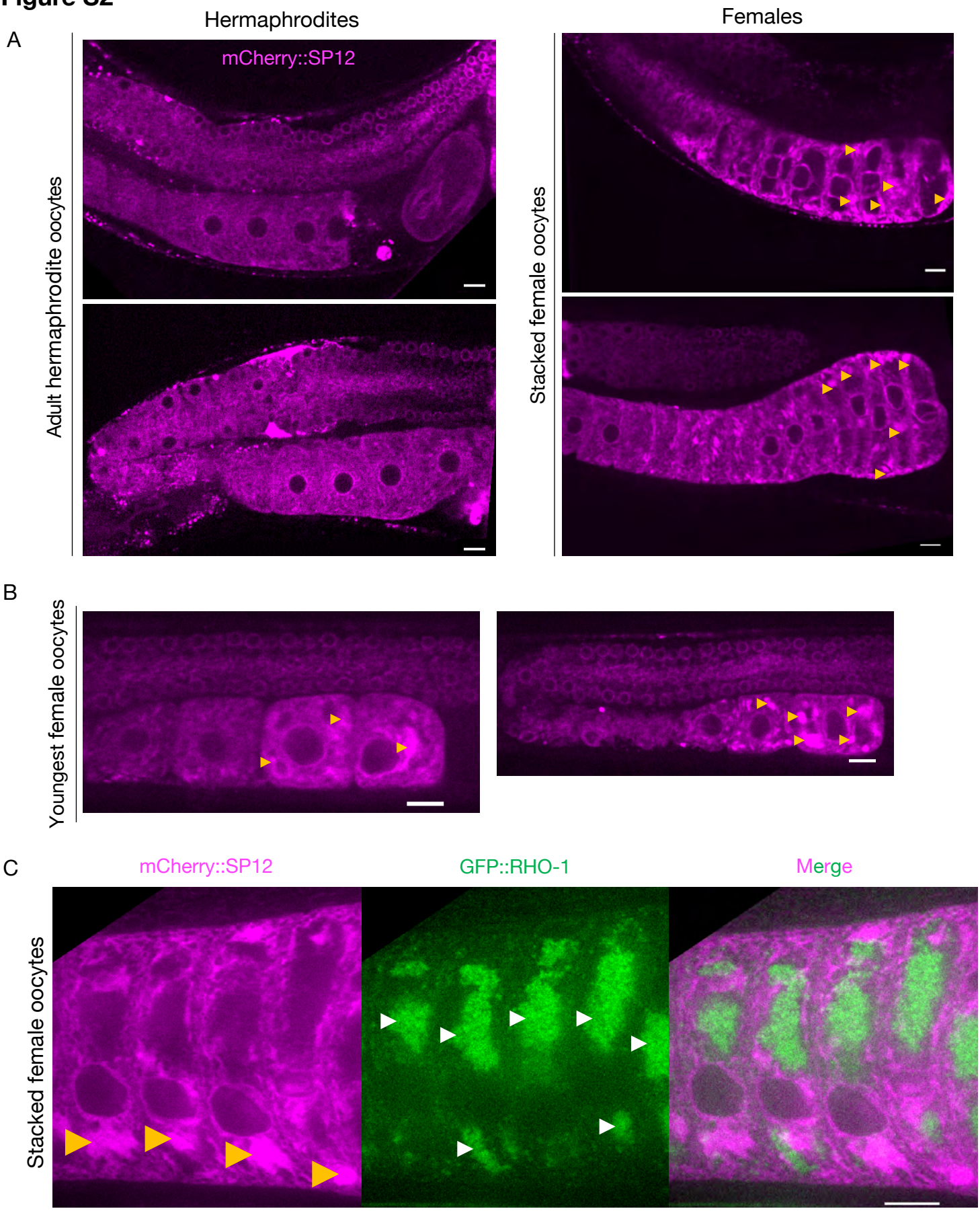
A
Hermaphrodites
Females
mCherry::SP12
Adult hermaphrodite oocytes
Stacked female oocytes
B
Youngest female oocytes
C
mCherry::SP12
GFP::RHO-1
Merge
Stacked female oocytes

Figure S2.

(A) Comparison of ER morphology in oocytes from hermaphrodites (OCF15) and females (CF4542) expressing the ER reporter mCherry::SP12 in the germline. Oocytes in the female gonad stack over time, as new meiotic cells make their way down towards the spermatheca, but mature ones pass less readily into the uterus. Orange arrows, ER patches. (B) Visualization of ER patches in young oocytes of female animals, staged to capture the earliest oocytes. (C) Simultaneous visualization of GFP::RHO-1 aggregates and the ER in females (CF4557) at high magnification (100X objective). Orange arrows: ER patches; white arrows: GFP::RHO-1 aggregates. Scale bars (A-C), 10 μm.

Figure S3

Hermaphrodites (Very first oocytes)

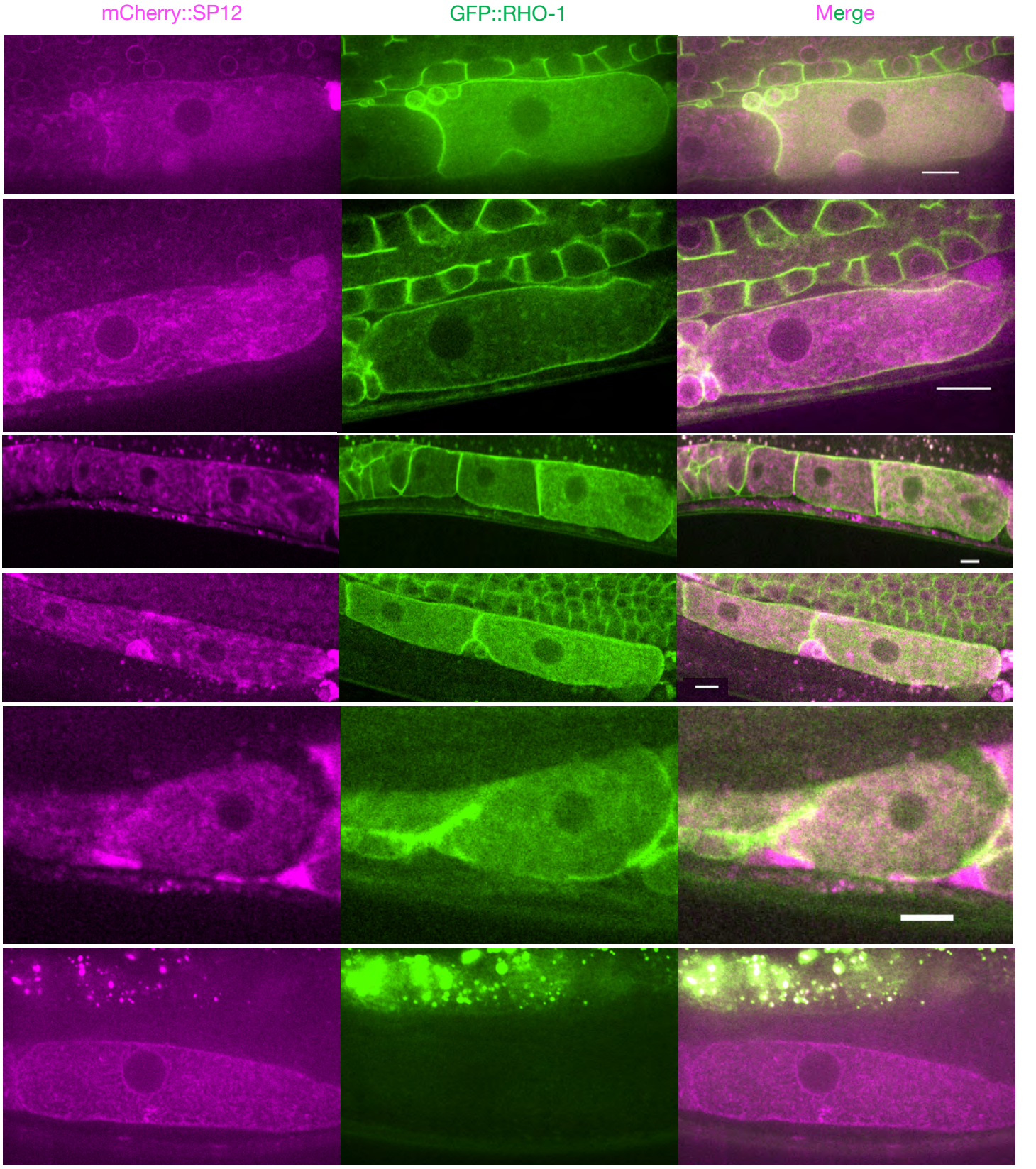

Figure S3.

Extended data related to Figure 2B.

ER morphology and GFP::RHO-1 localization in the first, newly-formed oocytes from mCherry::SP12-expressing hermaphrodites (CF4552). Scale bars,10 μm. Note that the GFP::RHO-1 image from the 1st row is also displayed in figure 1E.

Figure S4

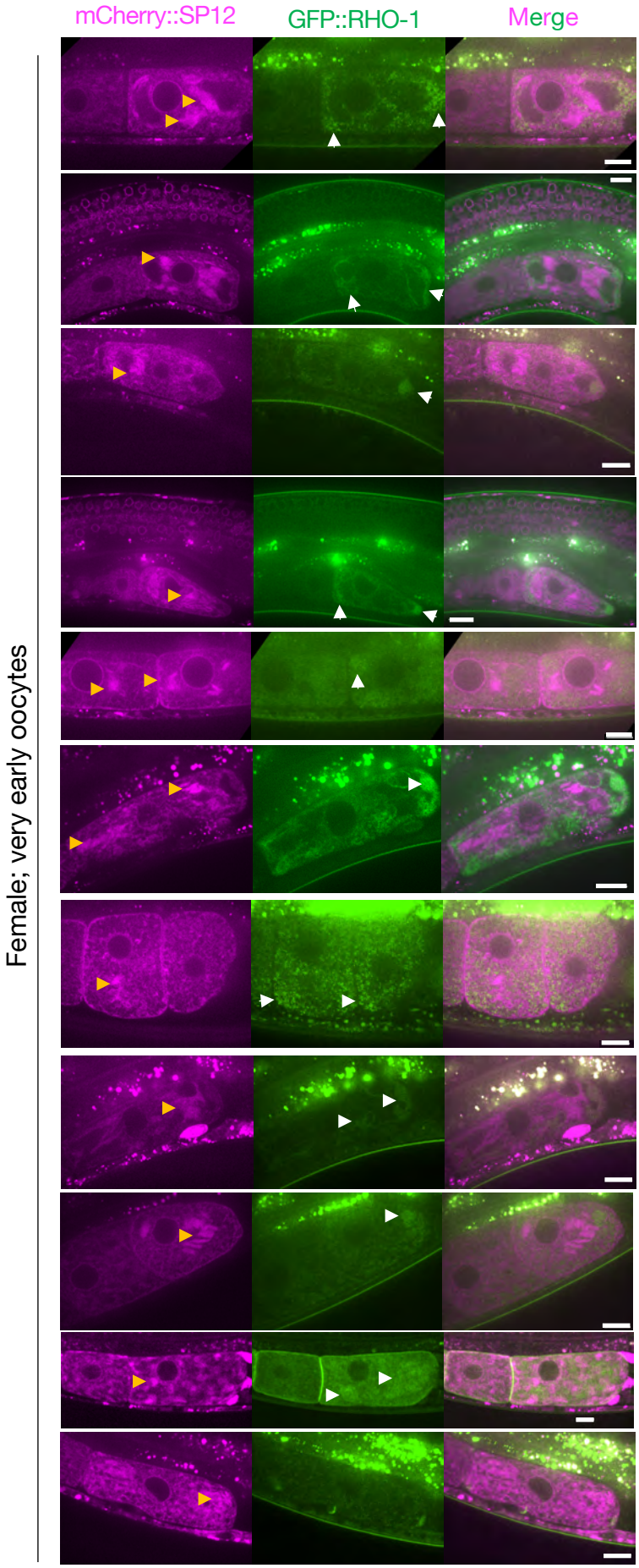

Figure S4.
Extended data related to Figure 2B.

ER morphology and GFP::RHO-1 localization in the first, newly-formed oocytes from mCherry::SP12 expressing females (CF4557). Orange arrows: ER patches; white arrows: GFP::RHO-1 aggregates. Scale bars, 10 μm. Note that the GFP::RHO-1 image from the 6th row is also displayed in Figure 1E.

Figure S5

Females

A

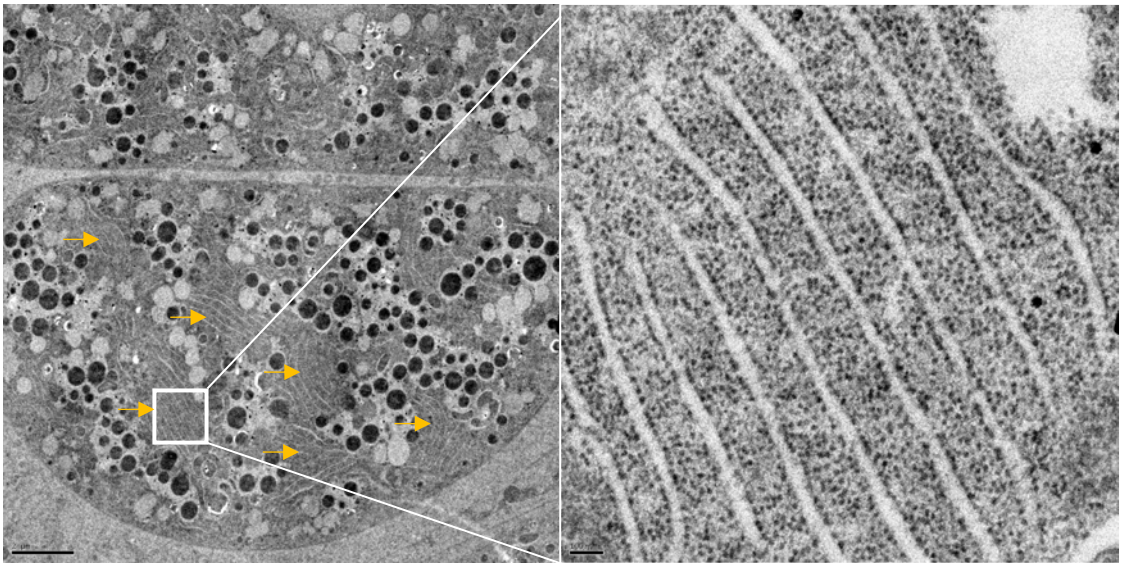

B

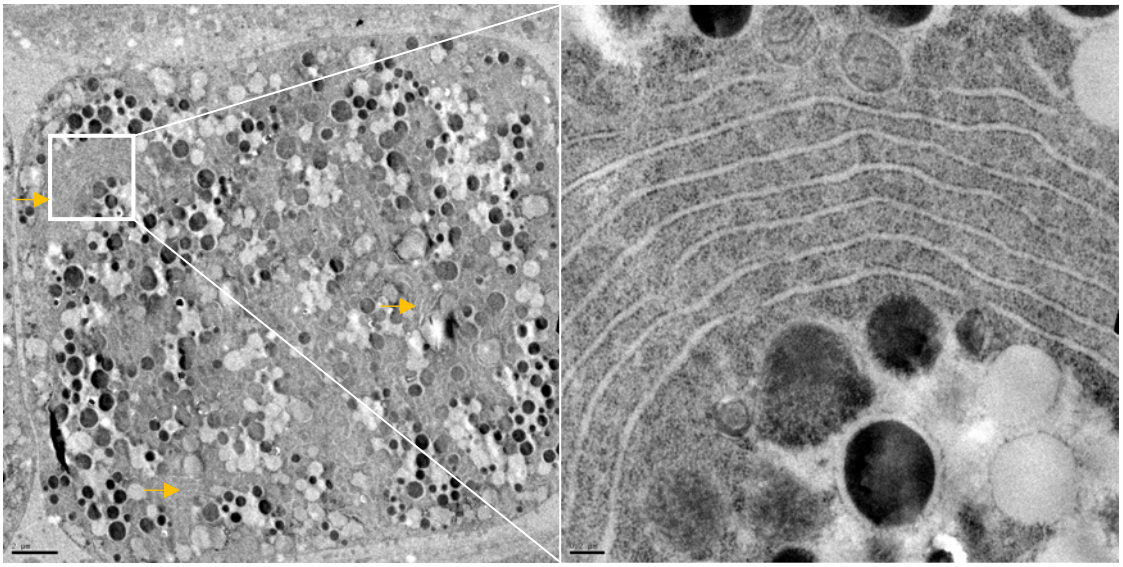

Hermaphrodite

C

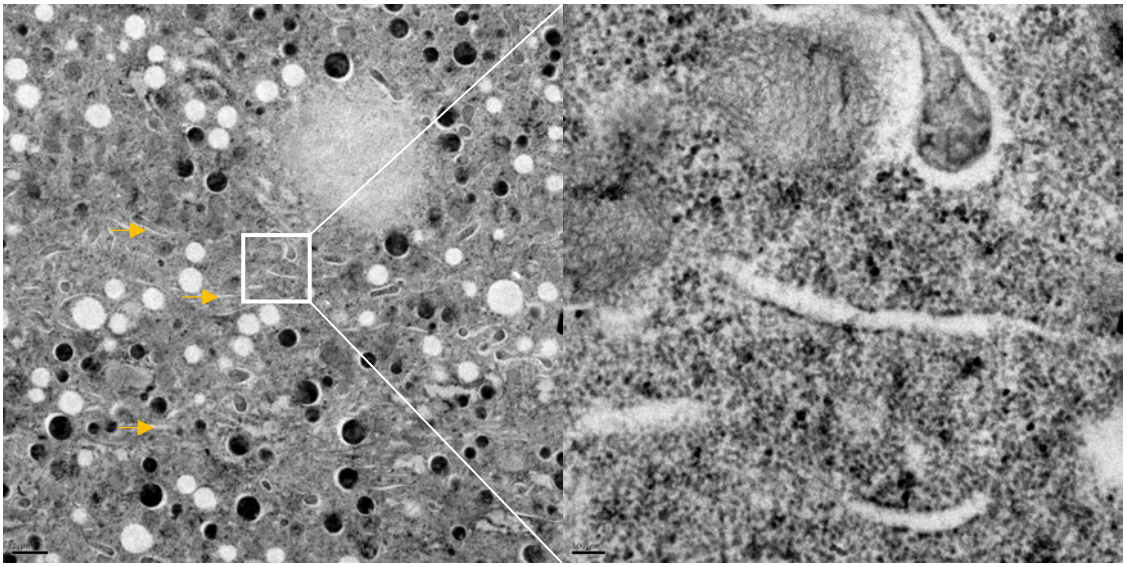

Figure S5.

Extended data related to Figure 2D.

Transmission electron micrographs from hermaphrodite (N2E) and female (CF4101) oocytes. (A) Female oocyte. Arrows, ER stacks. Left panel, magnification: 1,200X, scale bar, 2 μm. Right panel, magnification: 13,000X, scale bar, 100 nm. (B) Female oocyte. Arrows, ER stacks. Left panel, magnification: 890X, scale bar, 2 μm. Right panel, magnification: 6,800X, scale bar, 200 nm. (C) Hermaphrodite oocyte. Arrow, ER. Left panel, magnification: 1,400X, scale bar, 1 μm. Right panel, magnification: 13,000X, scale bar, 100 nm.

Figure S6A

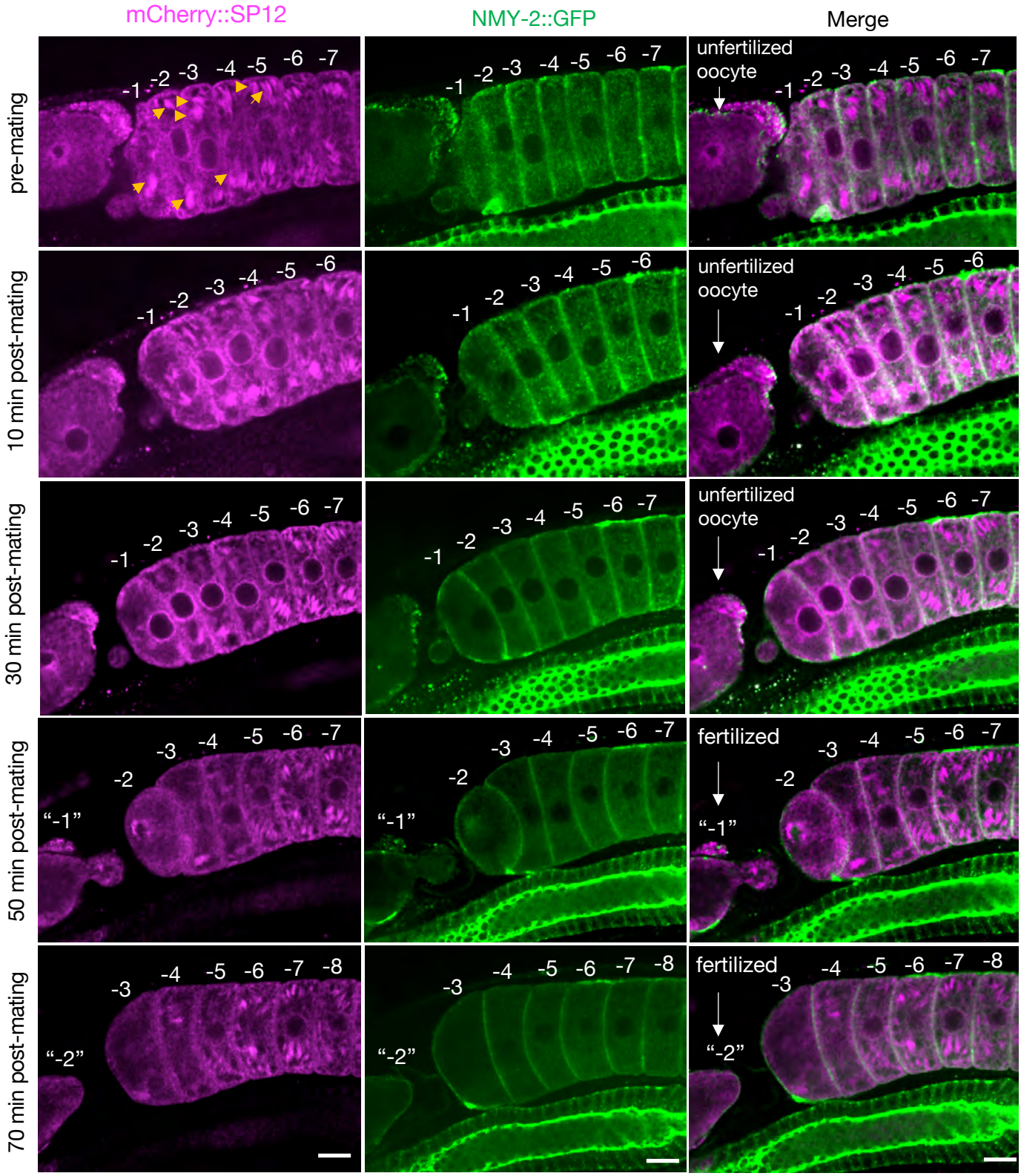
mCherry::SP12
NMY-2::GFP
Merge
pre-mating
10 min post-mating
30 min post-mating
50 min post-mating
70 min post-mating
unfertilized oocyte
fertilized
"-1"
"-2"

Figure S6B

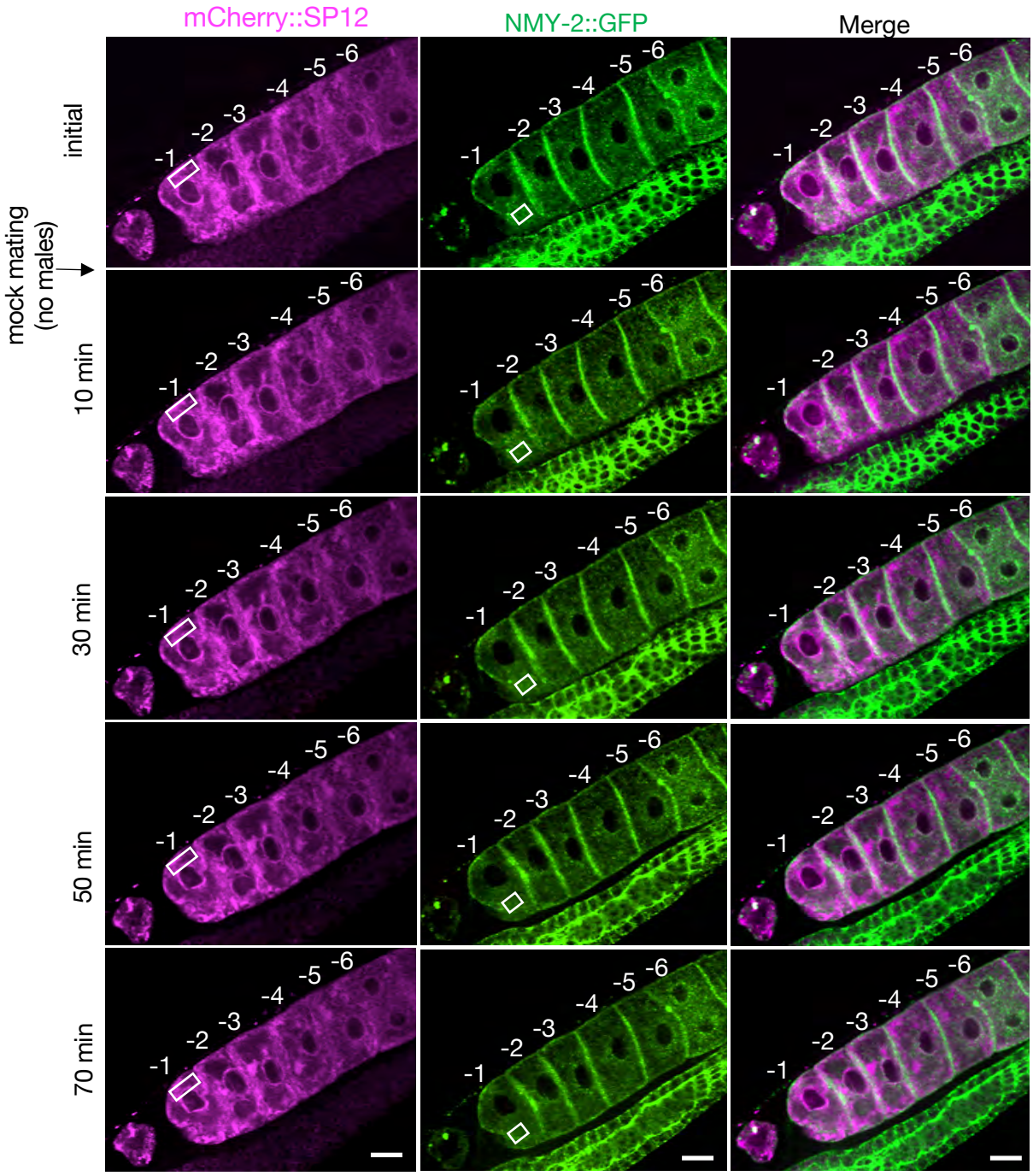
mCherry::SP12
NMY-2::GFP
Merge
initial
mock mating
(no males)
10 min
30 min
50 min
70 min
-1
-2
-3
-4
-5
-6

C

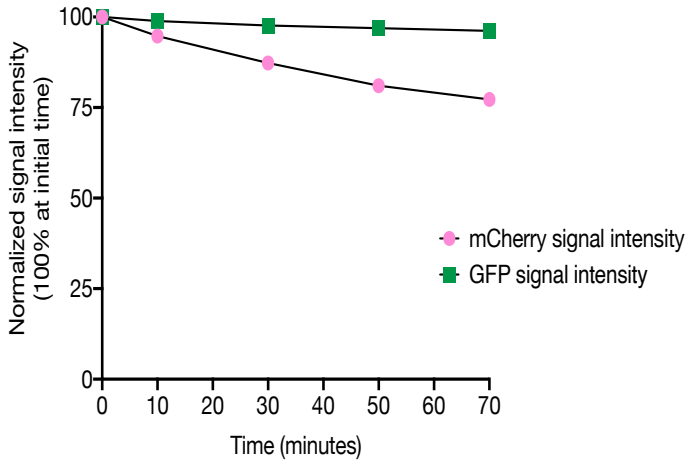
Normalized signal intensity
(100% at initial time)
100
75
50
25
0
0
10
20
30
40
50
60
70
Time (minutes)
mCherry signal intensity
GFP signal intensity

Figure S6.

(A) Simultaneous visualization of the alteration in ER morphology and clearance of aggregates in female oocytes (CF4560) as a function of time, following mating. The earliest changes in the mCherry::SP12 signal (ER) were observed ~10 minutes after mating, whereas the first signs of aggregate (NMY-2::GFP) clearance appeared later, between 20 and 30 minutes. The ER morphology was significantly altered by 30 minutes. Orange arrows: Initial ER patches altered at ~10 minutes. The oocytes are numbered according to their initial positions relative to the spermatheca prior to mating, and the numbers are maintained as the oocytes enter the uterus following fertilization. The figure shows a single representative animal from 7 independent experiments. Scale bars, 10 μm. (B) The mCherry::SP12 and NMY-2::GFP signals in oocytes from CF4560 females visualized as in (A) but not subjected to mating, to control for photobleaching. A single individual is shown from a total of 4 independent experiments. Scale bars,10 μm. (C) Reduction in signal intensity of the two fluorophores with time due to photobleaching, without exposure to males (from Fig. S6B). The signal intensities from specified areas (white rectangles) of the most proximal oocyte were assessed for this purpose.

Figure S7

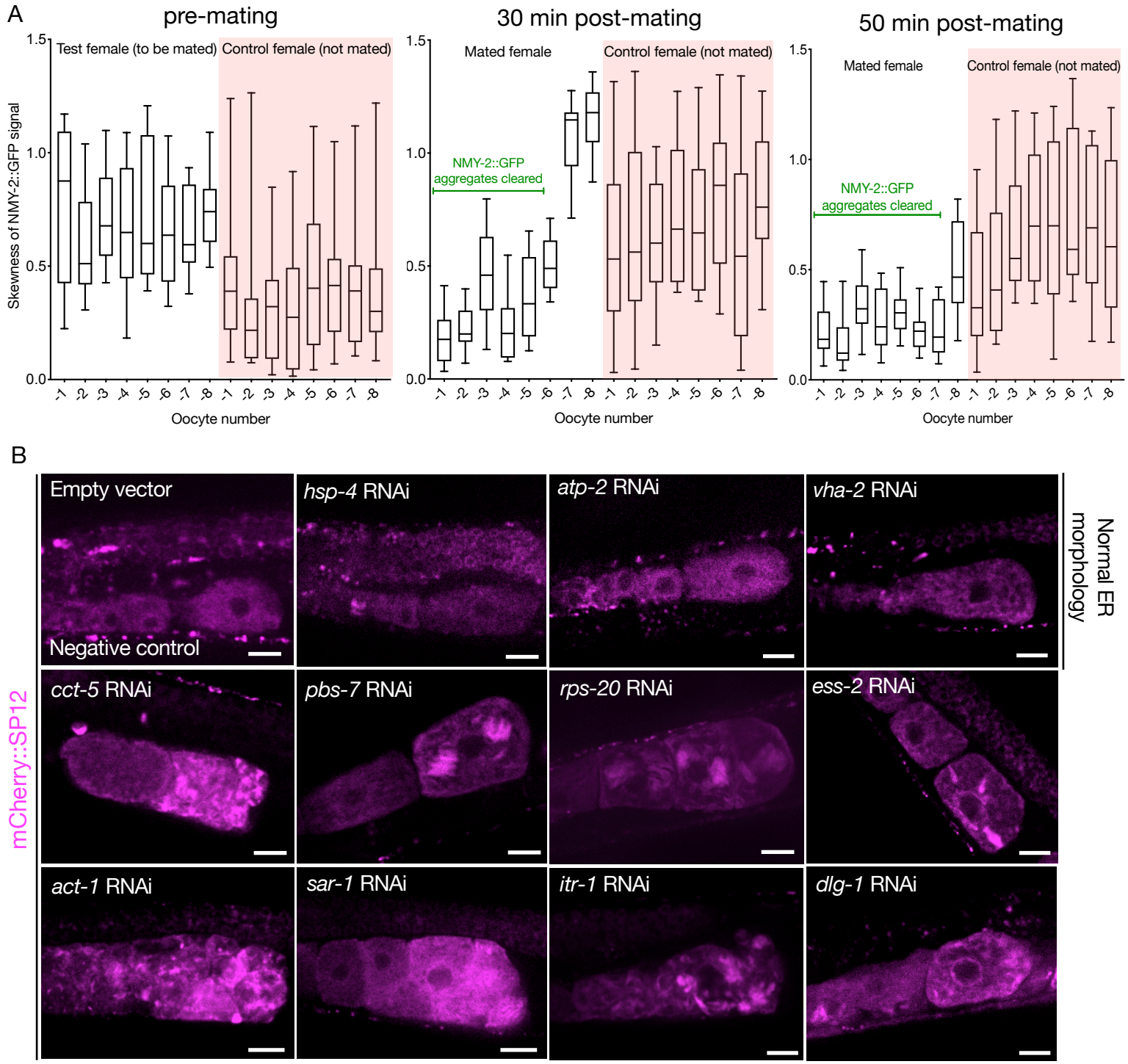
A
pre-mating
30 min post-mating
50 min post-mating
Test female (to be mated)
Control female (not mated)
Mated female
Control female (not mated)
NMY-2::GFP aggregates cleared
Skewness of NMY-2::GFP signal
Oocyte number
B
Empty vector
Negative control
hsp-4 RNAi
atp-2 RNAi
vha-2 RNAi
cct-5 RNAi
pbs-7 RNAi
rps-20 RNAi
ess-2 RNAi
act-1 RNAi
sar-1 RNAi
itr-1 RNAi
dlg-1 RNAi
mCherry::SP12
Normal ER morphology

Figure S7.

(A) NMY-2::GFP signal skewness as a function of time in the proximal oocytes of CF4560 females, either subjected to mating with CB1490 males (white), or not exposed to males (pink). The mated females exhibit a reduction in signal skewness with time, and in relation to the distance from spermatheca, indicative of aggregate clearance. (B) Examples of oocyte ER morphology in CF4552 hermaphrodites subjected to assay-pool RNAi treatment, demonstrating the range of morphologies we observed. GFP::RHO-1 aggregation in the same animals was used as a control to verify successful gene knockdown (not shown). Scale bars, 20 μm.

Figure S8

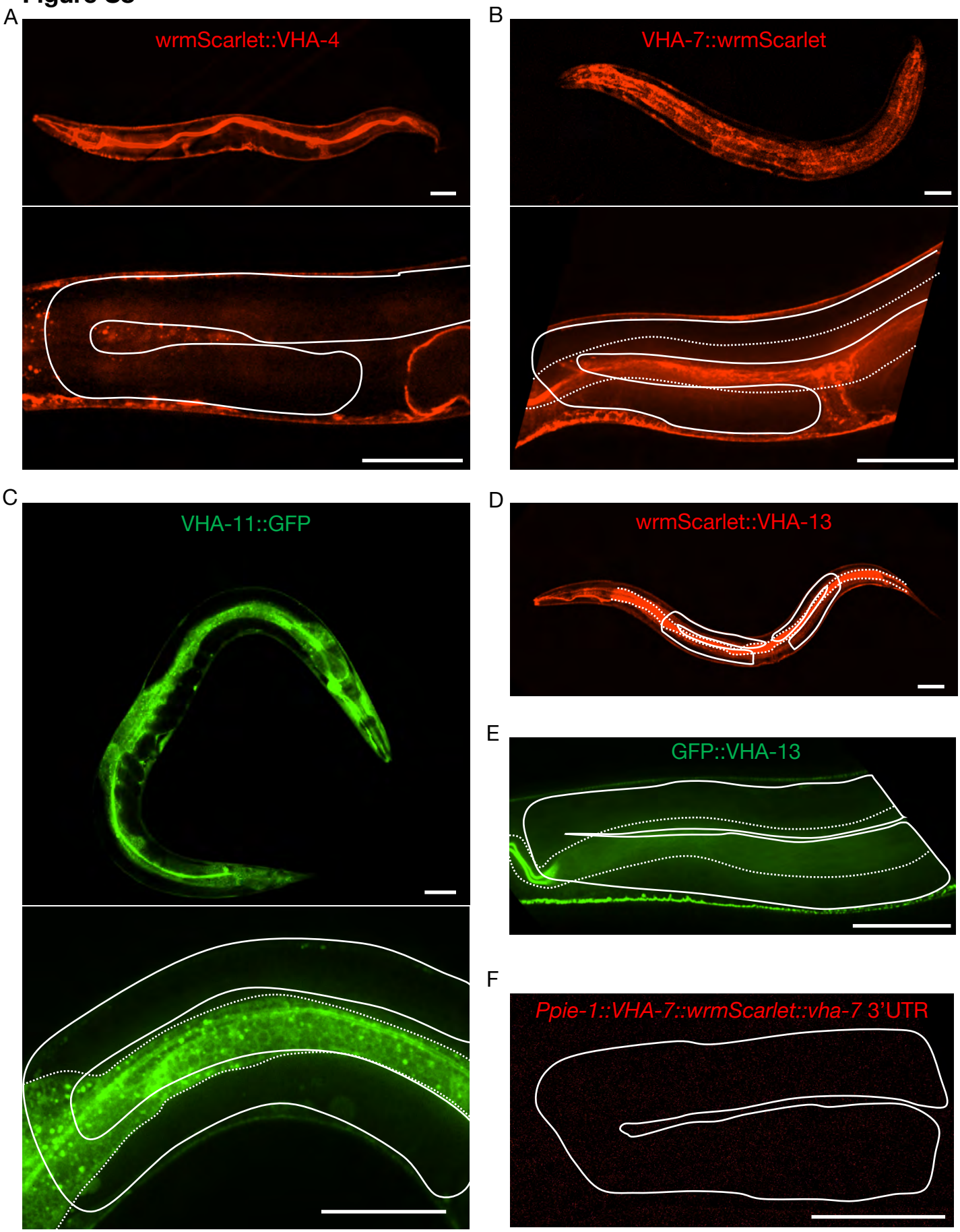
A
wrmScarlet::VHA-4
B
VHA-7::wrmScarlet
C
VHA-11::GFP
D
wrmScarlet::VHA-13
E
GFP::VHA-13
F
Ppie-1::VHA-7::wrmScarlet::vha-7 3'UTR

Figure S8.

Expression of endogenously tagged V-ATPase subunits from the V_0 domain (A and B) and the V_1 domain (C, D and E), and of a single-copy integrated germline transgene (F). None of the strains exhibited detectable signal in the gonad. (A) wrmScarlet::VHA-4, PHX1363 *vha-4(syb1363[wrmScarlet::vha-4]/+) II*, (B) VHA-7::wrmScarlet, PHX1317 *vha-7(syb1317[vha-7::wrmScarlet]) IV*, (C) VHA-11::GFP*,* PHX1198 *ieSi65[sun-1p::TIR1::sun-1 3'UTR Cbr-unc-119(+)] II; unc-119(ed3) III; vha-11(syb1198[vha-11::gfp::degron]/+) IV*, (D) wrmScarlet::VHA-13, PHX731 *vha-13(syb731[wrmScarlet::vha-13]) V*, (E) GFP::VHA-13, PHX1049 *vha-13(syb1049[gfp::vha-13]) V,* (F) *Ppie-1::vha-7::wrmScarlet::vha-7* 3'UTR, PHX2690 *sybIs2690[Ppie-1::vha-7::wrmScarlet::vha-7 3'UTR Cbr-unc-119(+)] I; unc-119(ed3) III.* Solid line; gonad and dotted line; intestine. Scale bars, 50 µm. For each strain, a minimum of 50 animals were first analyzed under a fluorescent stereo microscope. At least 3 animals were then imaged for each strain, by confocal microscopy. Strains were generated by SunyBiotech for the Kenyon lab.

Figure S9

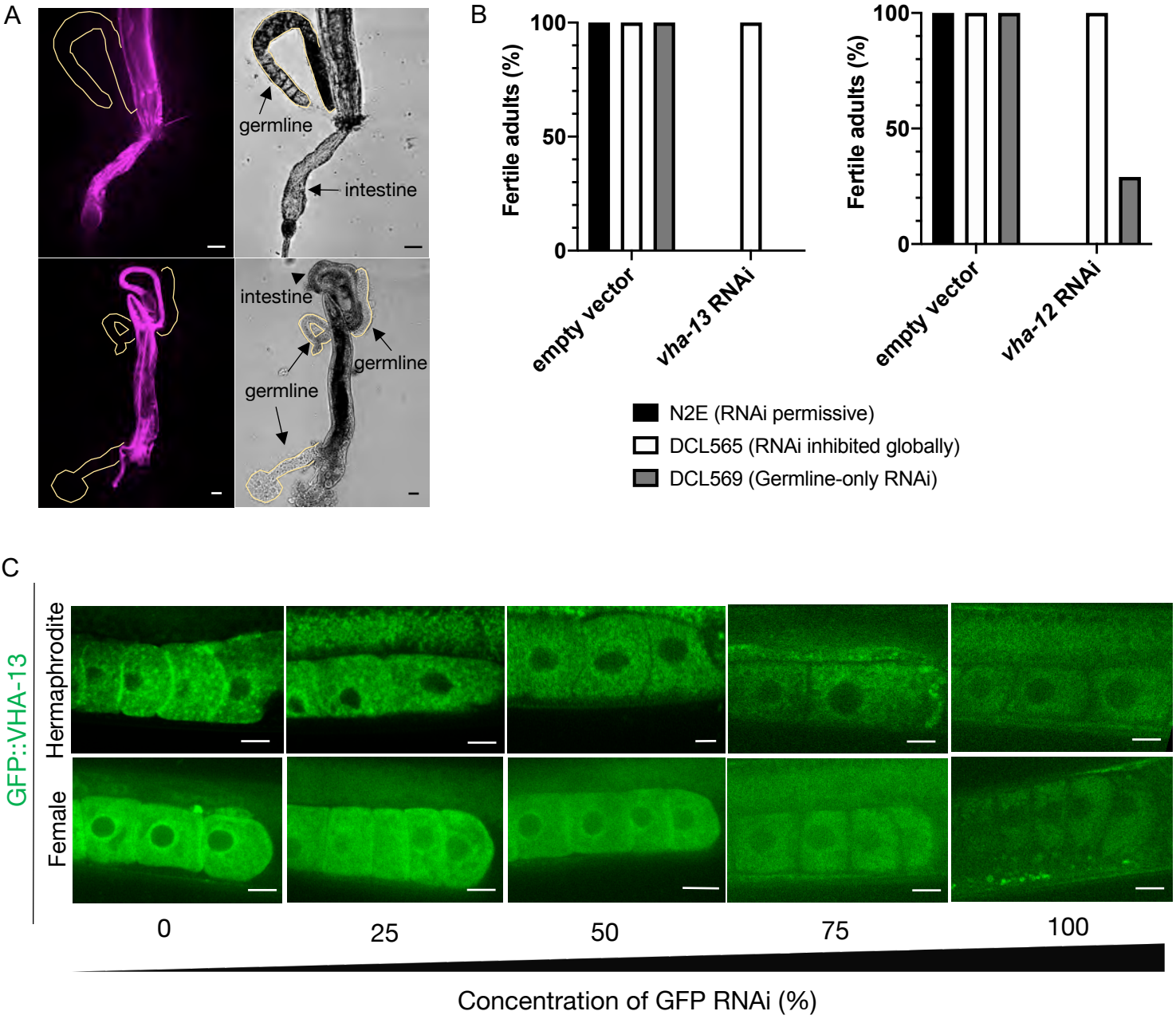
A
germline
intestine
intestine
germline
germline
B
Fertile adults (%)
100
50
0
empty vector
vha-13 RNAi
Fertile adults (%)
100
50
0
empty vector
vha-12 RNAi
N2E (RNAi permissive)
DCL565 (RNAi inhibited globally)
DCL569 (Germline-only RNAi)
C
GFP::VHA-13
Hermaphrodite
Female
0
25
50
75
100
Concentration of GFP RNAi (%)

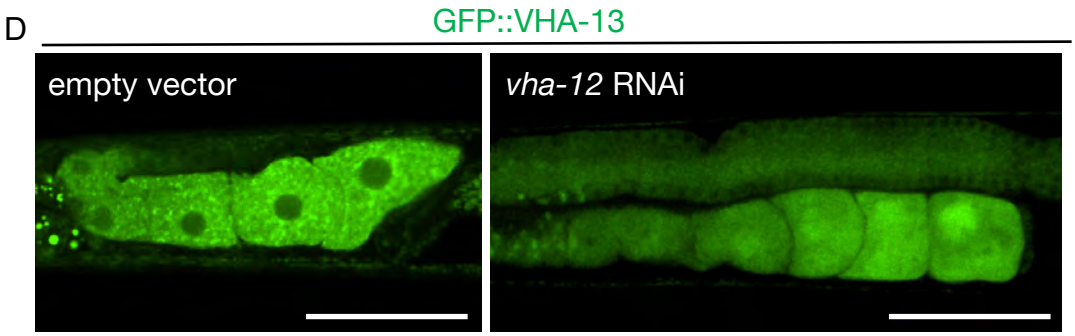
D
GFP::VHA-13
empty vector
vha-12 RNAi

Figure S9.

(A) Attempts to visualize endogenously-tagged wrmScarlet::VHA-13 expression in the germline of PHX731 animals by dissecting gonads (n = 10 worms), to distance them from somatic tissues where it is highly expressed. Scale bars, 25 μm. (B) Percentage of fertile adults in N2E, DCL565 *rde-1(mkc36)*, and DCL569 *rde-1(mkc36); Psun-1::rde-1(+)* strains upon exposure to empty vector RNAi control, *vha-13* RNAi or *vha-12* RNAi, from hatching. Results are averaged from 3 biological replicates with each n>10. (C) Reduction of GFP::VHA-13 expression by serial dilution of *gfp* RNAi bacteria. Even at the limit of fluorescence detection, hermaphrodites (PHX1414) exhibit discrete GFP::VHA-13 foci, whereas females (CF4599) exhibit a diffuse distribution. Scale bars, 10 μm. (D) Expression of GFP::VHA-13 in the germline of hermaphrodites exposed to empty vector RNAi (left) or *vha-12* RNAi (right). Scale bars, 50 μm.

Figure S10

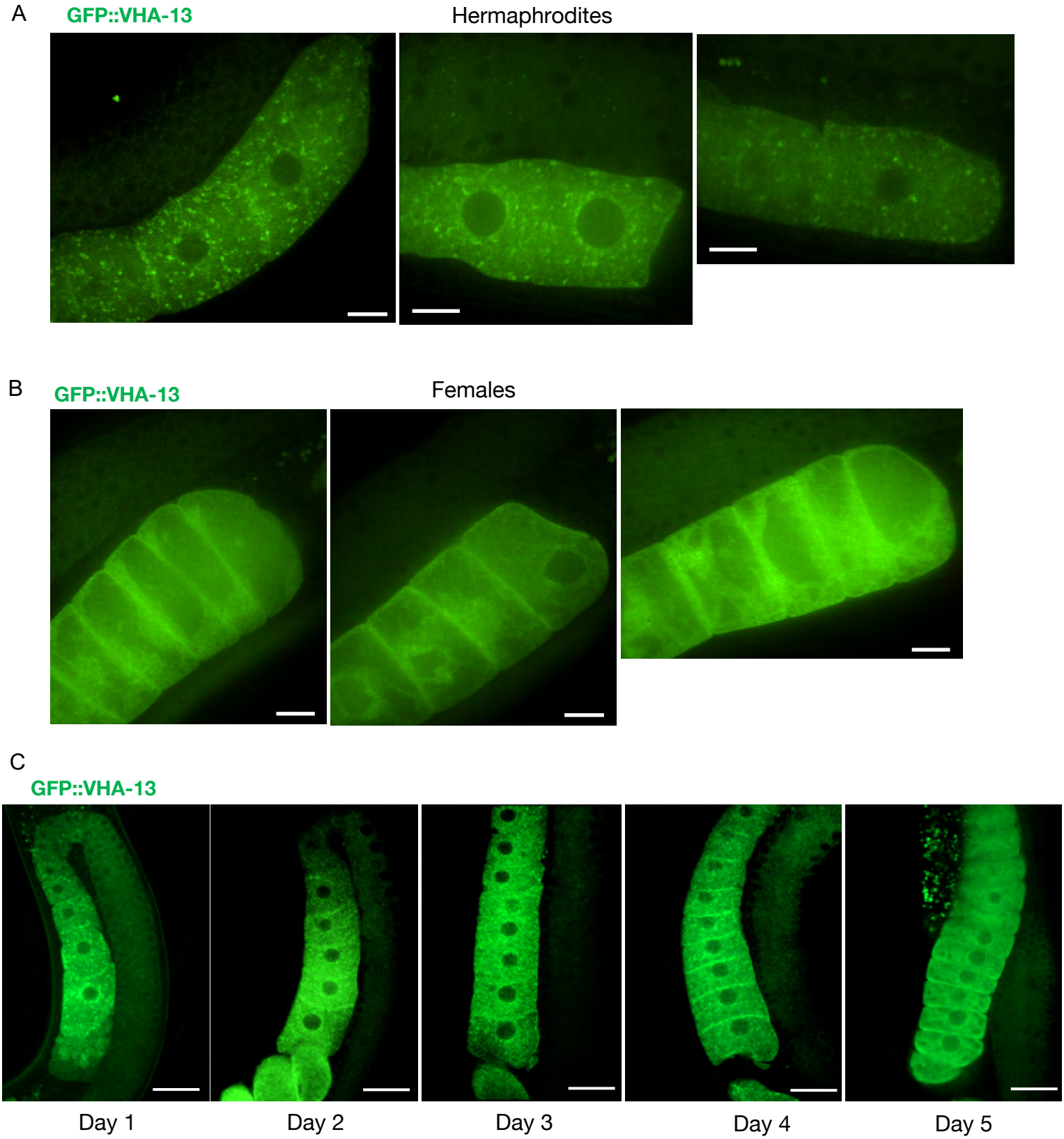
A
GFP::VHA-13
Hermaphrodites
B
GFP::VHA-13
Females
C
GFP::VHA-13
Day 1
Day 2
Day 3
Day 4
Day 5

Figure S10.

Extended data related to Figure 3A.

Additional images showing the distribution of GFP::VHA-13 in proximal oocytes of (A) hermaphrodites (PHX1414) and (B) females (CF4599). Scale bars, 10 μm. (C) Changes in oocyte GFP::VHA-13 localization, from punctate to diffuse, in hermaphrodites (PHX1414) imaged daily from day-1 to day-5 of adulthood, when sperm are depleted. Scale bars, 20 μm.

Figure S11

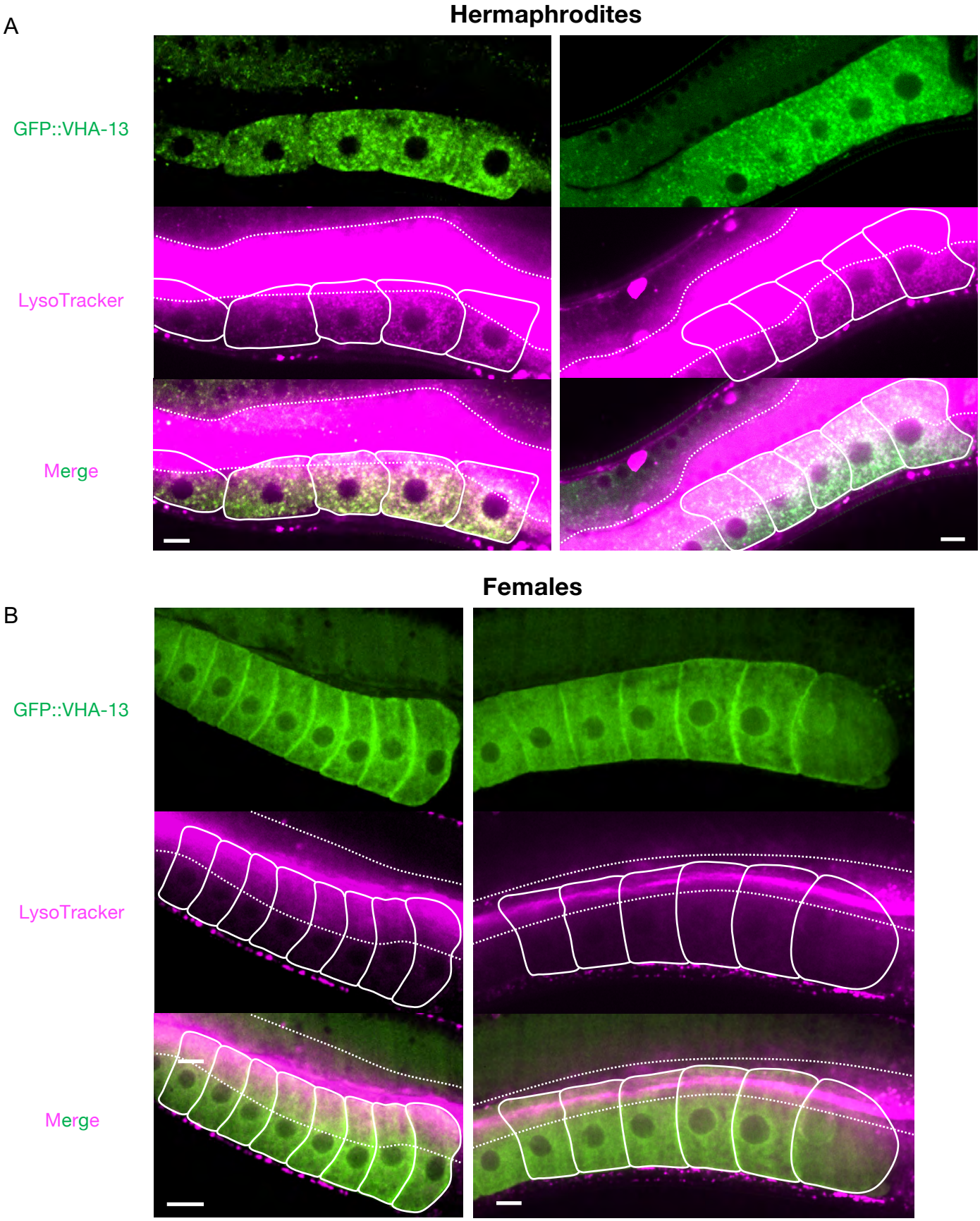
A
Hermaphrodites
GFP::VHA-13
LysoTracker
Merge
B
Females
GFP::VHA-13
LysoTracker
Merge

Figure S11.

Extended data related to Figure 3B.

Additional images of the LysoTracker-stained oocytes from GFP::VHA-13-expressing (A) hermaphrodites (PHX1414) and (B) females (CF4599), for visualization of acidic lysosomes. The two signals colocalize in hermaphrodite oocytes. Dotted line; intestinal boundary, and solid line; oocytes. Scale bars, 10 μm.

Figure S12

A

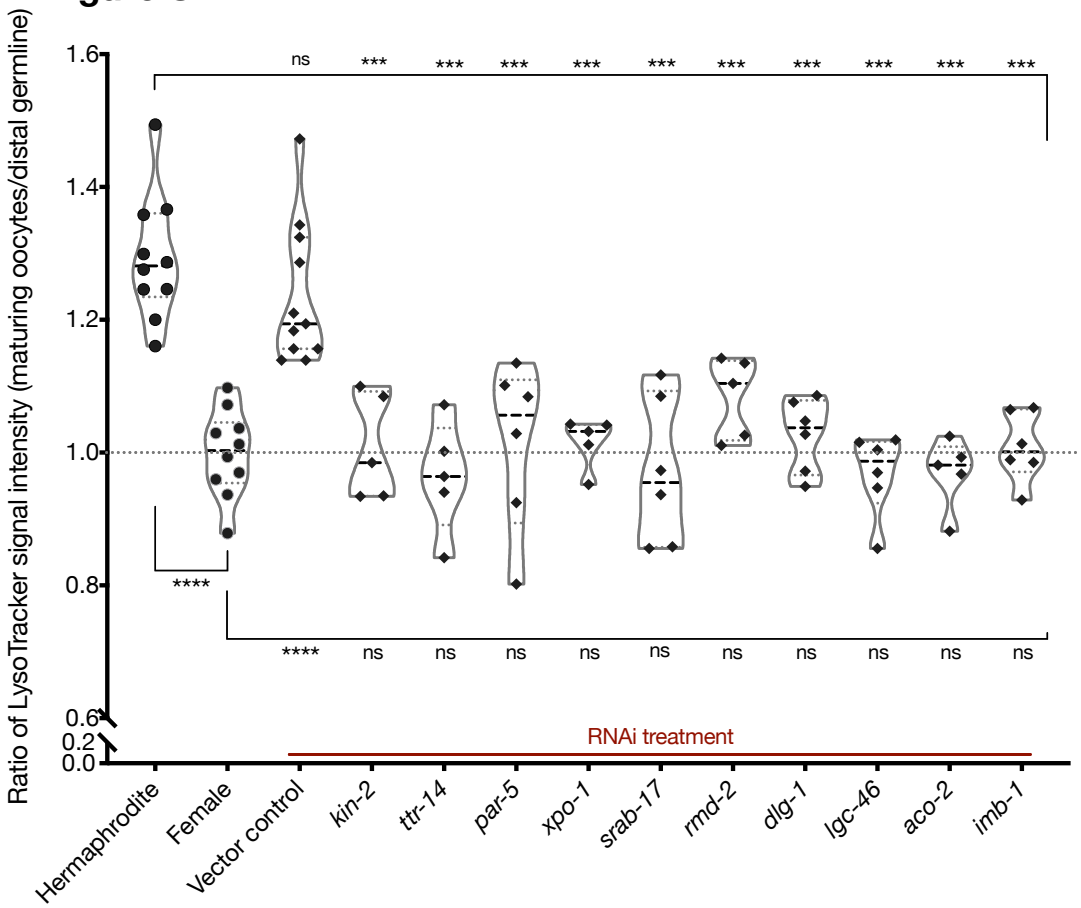

B

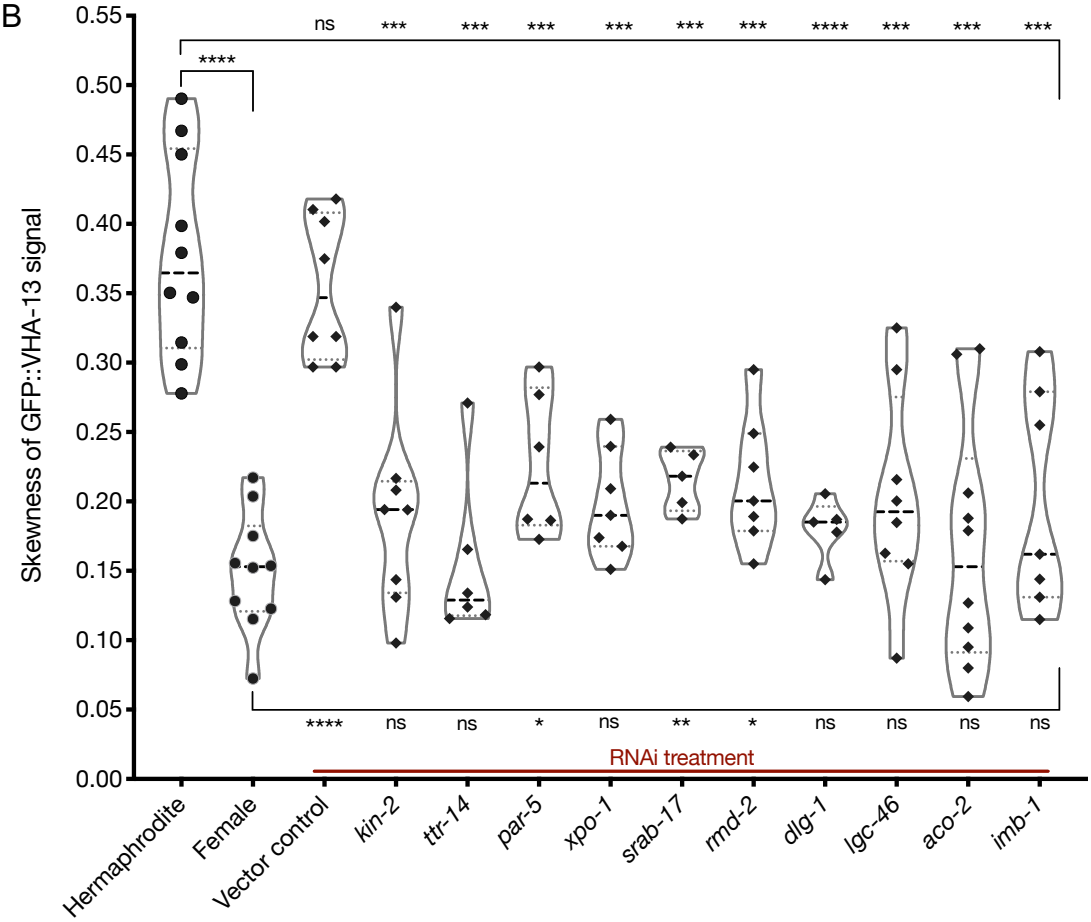

C

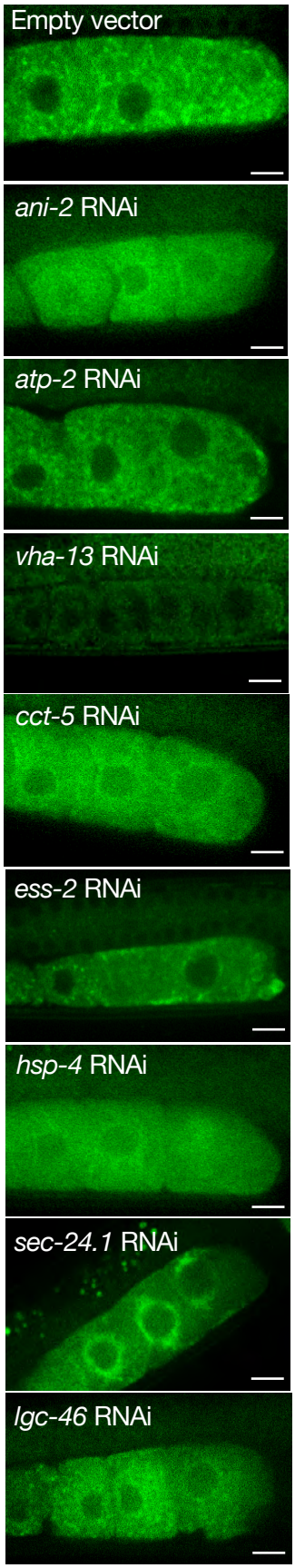

Figure S12.

(A) Analysis of germline LysoTracker staining in hermaphrodites (SA115) subjected to RNAi for the orphan genes. The LysoTracker signal is represented as the ratio of proximal oocyte to distal germline staining, and the values obtained from hermaphrodites (N2E) and females (CF4101) were used as controls (~1.3 and ~1.0, respectively). Each data point represents the average of values from 3 different locations in the most proximal oocyte of a single animal. The presence of GFP::RHO-1 aggregates in the same animals was used as a control to determine successful gene knockdown (not shown). (B) Analysis of GFP::VHA-13 localization (in terms of signal skewness) in hermaphrodites (PHX1414) subjected to RNAi for the orphan genes, and compared to hermaphrodite and female animals (PHX1414 and CF4599). Each data point represents the average of 10 skewness values from independent regions within the first three oocytes of a single animal. The presence of GFP::RHO-1 aggregates in SA115 animals in a parallel experiment served as a control for successful gene knockdown (not shown). For (A) and (B), Mann-Whitney test was used to determine the statistical significance. The top and bottom rows of significance indicators in each experiment compare a specific RNAi condition to hermaphrodite and female animals respectively. P values: $P > 0.05$ = n.s., *$P \leq 0.05$, **$P \leq 0.01$, ***$P \leq 0.001$ and ****$P \leq 0.0001$. (C) Visualization of GFP::VHA-13 distribution and localization in PHX1414 hermaphrodites following RNAi. A few representative gene knockdowns from the assay pool are shown here to demonstrate the range of localization phenotypes observed. Scale bars, 10 μm.

Figure S13

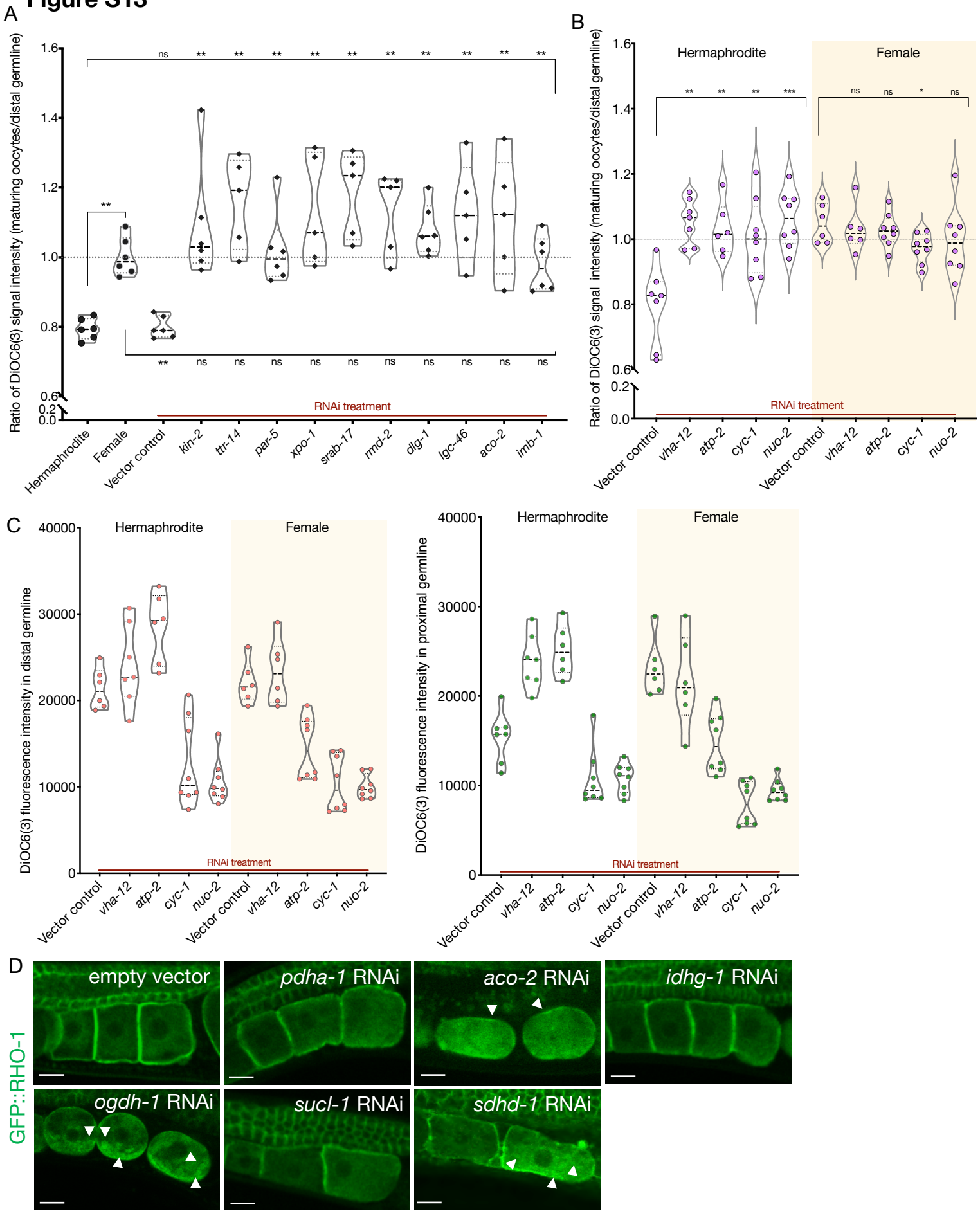
A
Ratio of DiOC6(3) signal intensity (maturing oocytes/distal germline)
RNAi treatment
Hermaphrodite
Female
Vector control
kin-2
ttr-14
par-5
xpo-1
srab-17
rmd-2
dlg-1
lgc-46
aco-2
imb-1
B
Hermaphrodite
Female
Ratio of DiOC6(3) signal intensity (maturing oocytes/distal germline)
RNAi treatment
Vector control
vha-12
atp-2
cyc-1
nuo-2
C
Hermaphrodite
Female
DiOC6(3) fluorescence intensity in distal germline
DiOC6(3) fluorescence intensity in proximal germline
RNAi treatment
D
GFP::RHO-1
empty vector
pdha-1 RNAi
aco-2 RNAi
idhg-1 RNAi
ogdh-1 RNAi
sucl-1 RNAi
sdhd-1 RNAi

Figure S13.

(A) Analysis of germline DiOC6(3) staining in hermaphrodite animals (OCF15) subjected to RNAi for the orphan genes, represented as the ratio of proximal oocyte to distal germline staining. Staining ratios obtained from N2E hermaphrodites (~0.8) and CF4101 females (~1) were used as controls for comparison. Each data point represents the average of values from 3 different locations within the most proximal oocyte of a single animal. When applicable, alteration in ER morphology was used as a control to determine successful gene knockdown in the same animals. The presence of aggregates in GFP::RHO-1 animals (SA115) treated in parallel was also used as a control to verify successful gene knockdown (not shown). The top and bottom rows of significance indicators compare a specific RNAi treatment to hermaphrodites and females, respectively. (B) DiOC6(3) staining expressed as the ratio between proximal oocytes and distal germline, in hermaphrodites (N2E; white) and females (CF4101; yellow) subjected to RNAi treatment for control (*vha-12* and *atp*-2) and electron transport chain (*cyc-1* and *nuo*-2) genes. Successful gene knockdown was determined by monitoring GFP::RHO-1 aggregation in parallel (shown in Figure 5B). (A-B) Mann-Whitney test was used to determine the statistical significance. P values: $P > 0.05$ = n.s., *$P \leq 0.05$, **$P \leq 0.01$ and ***$P \leq 0.001$. (C) For the animals in B, DiOC6(3) signal intensity following RNAi treatment for electron transport chain genes in the distal (left panel) and proximal (right panel) germlines, respectively. *vha-12*-RNAi was used an independent positive control. (D) Identification of Krebs cycle genes that, when knocked down in hermaphrodites (SA115), cause GFP::RHO-1 aggregates to accumulate in oocytes. Scale bars, 10 μm; white arrows, GFP::RHO-1 aggregates.

Figure S14

A

BioTracker ATP-Red staining

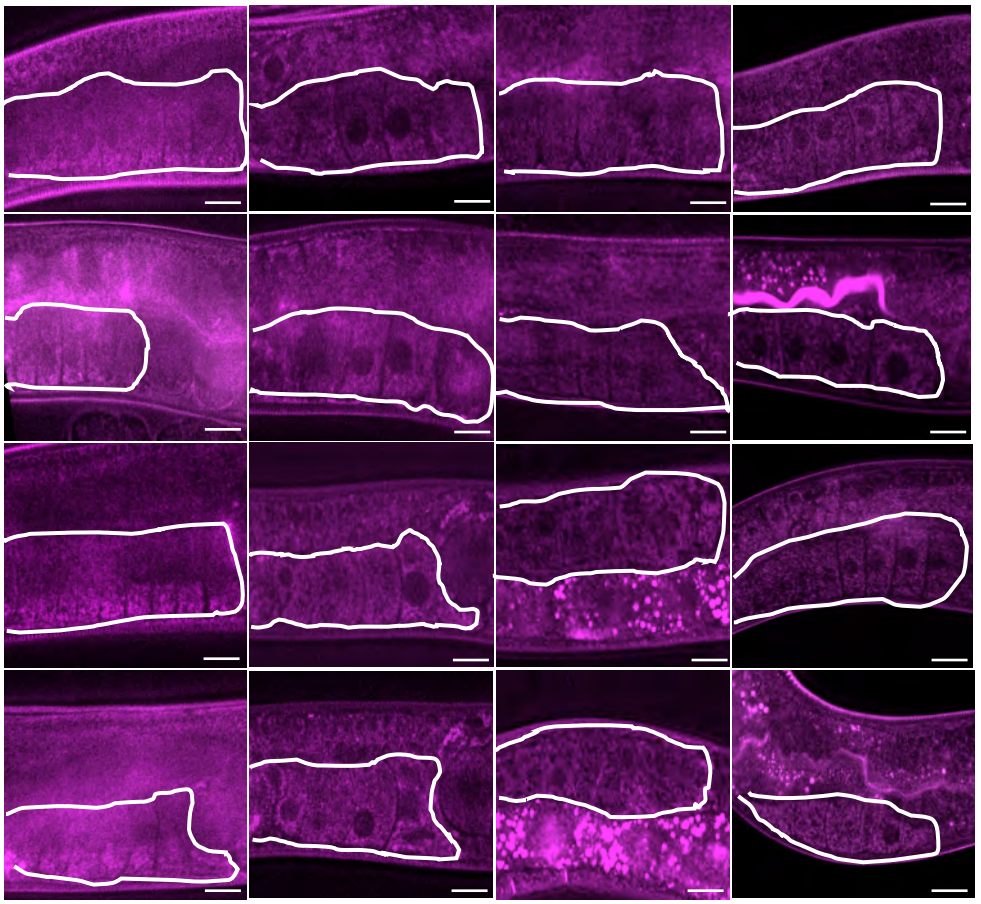

Empty vector *RNAi* | *atp-2 RNAi* | *cyc-1 RNAi* | *nuo-2 RNAi*

B

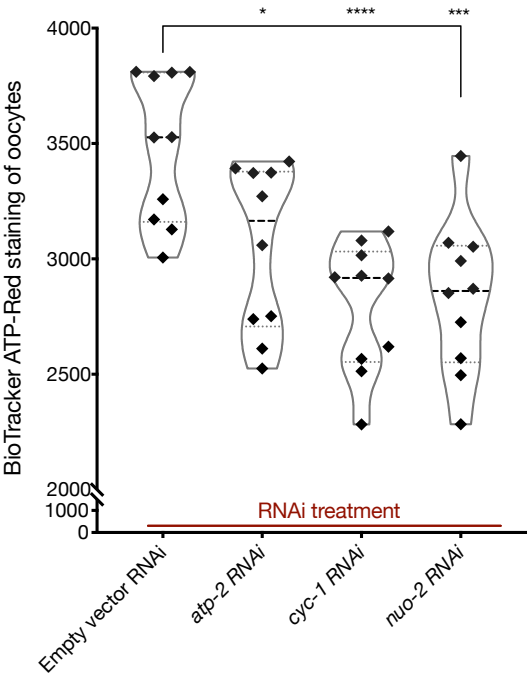

C

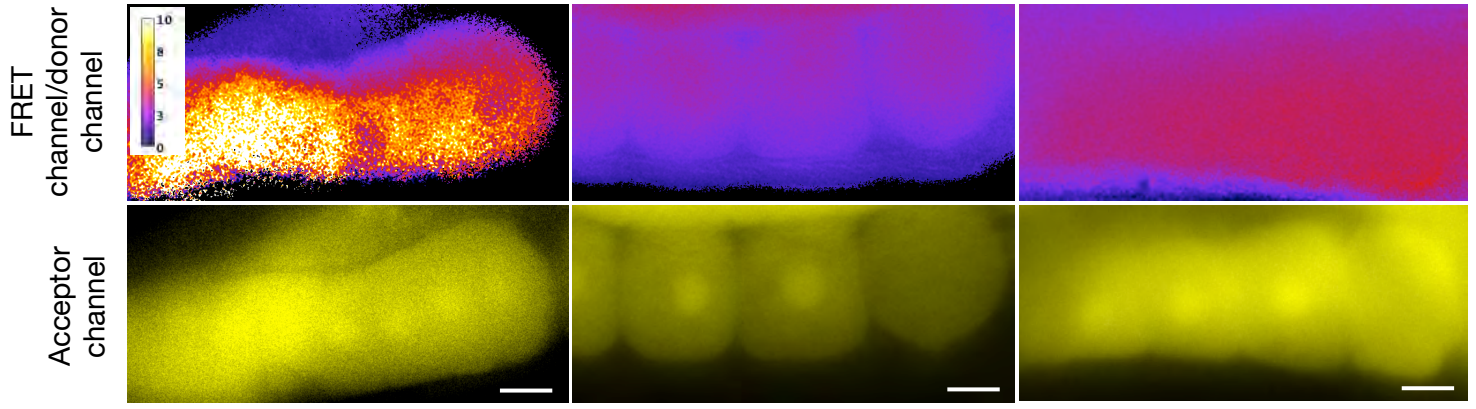

Empty vector *RNAi* | *cyc-1 RNAi* | *nuo-2 RNAi*

Figure S14.

(A) BioTracker ATP-Red stained germlines of dye-fed animals also subjected to knockdowns of ETC subunits; proximal germlines, white outlines. Scale bars, 20 μm. (B) Quantification of BioTracker ATP-Red staining. Each data point represents the average of fluorescence intensity values normalized to area, from 12 independent locations of the first three oocytes of a single animal. Mann-Whitney test was used to determine the statistical significance. P values: *P ≤ 0.05, ***P ≤ 0.001 and ****P ≤ 0.0001. (C) Comparison of oocyte ATP levels subjected to electron transport chain (ETC) knockdowns (*cyc-1* and *nuo-2*), using the Ateam sensor. Relative ATP levels estimated from the ratio of FRET channel to donor channel using an intensity scale (top panel); and fluorescence observed in the acceptor channel (bottom panel). Scale bars, 10 μm; Note: we examined very few animals in this experiment, due to transgene silencing: n= 2 animals per RNAi condition and n=1 for control. Therefore, support for our interpretation rests primarily on the BioTracker ATP-Red dye-staining experiment.

Figure S15

A

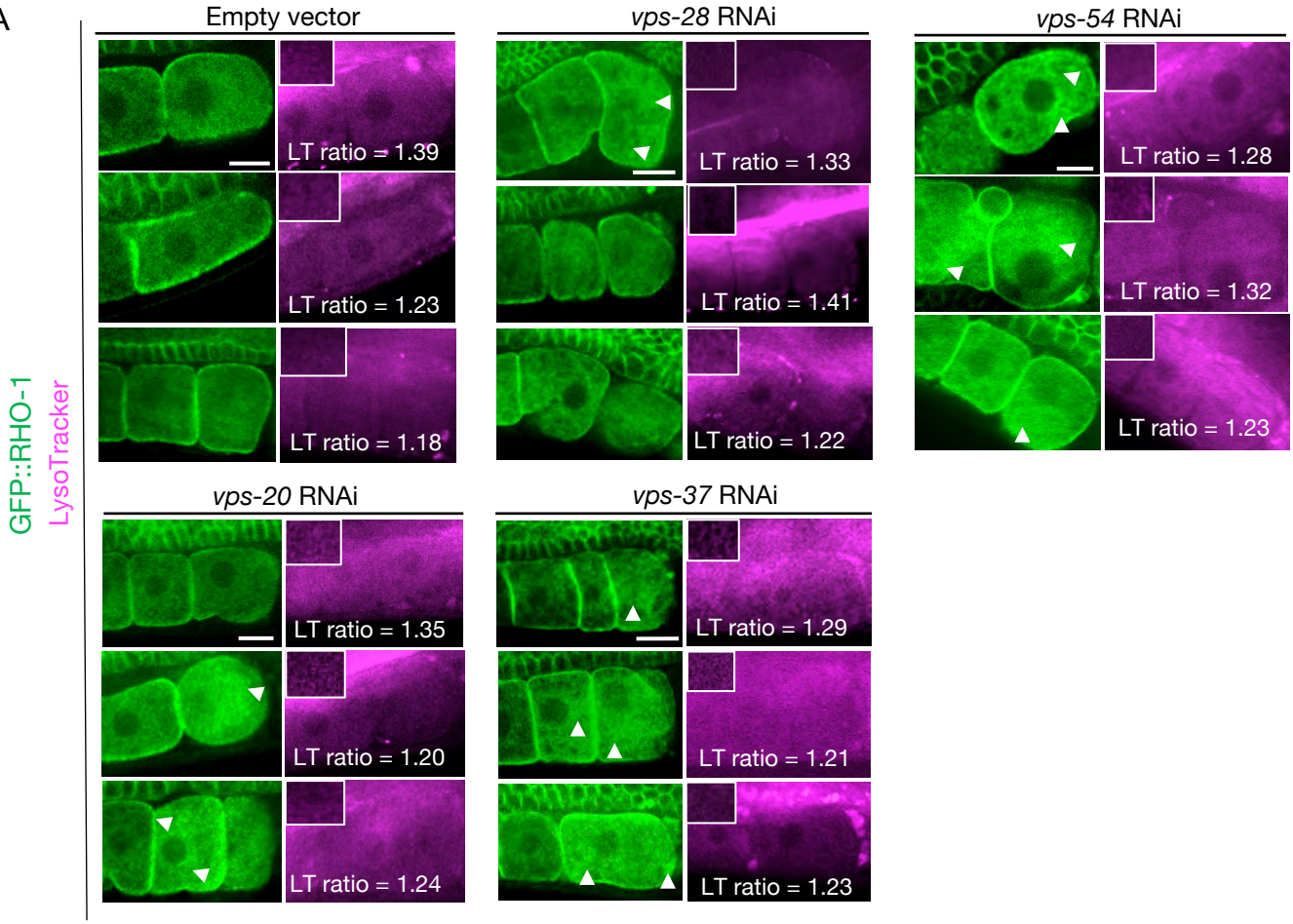

B

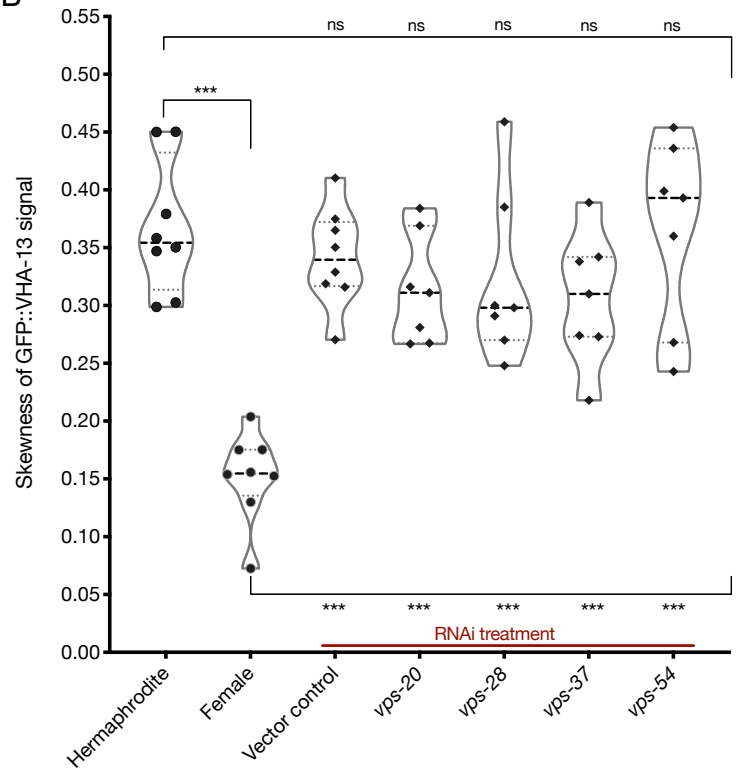

C

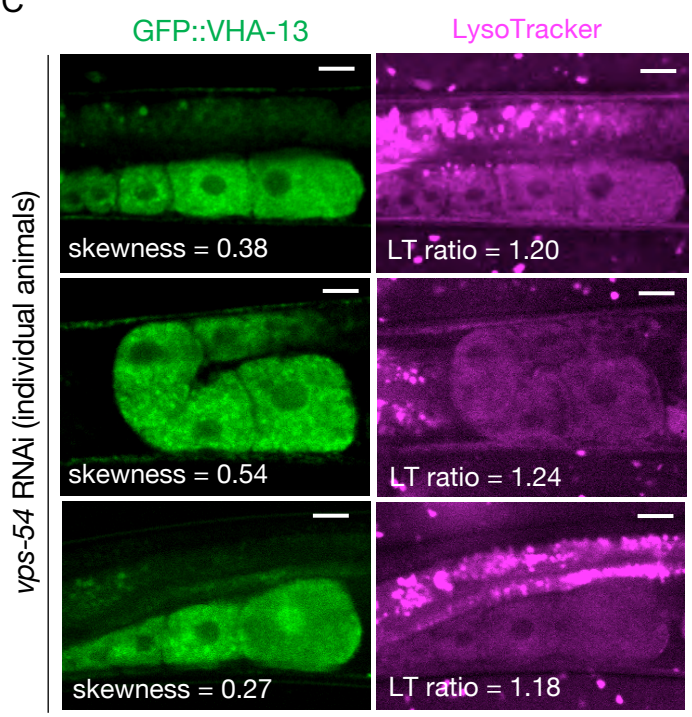

Figure S15.

(A) GFP::RHO-1 aggregation and LysoTracker signal in hermaphrodites (SA115) subjected to ESCRT-complex RNAi. The proximal oocyte/distal germline ratio of LysoTracker intensity is indicated for each animal. Distal germline images from the same animal are shown as insets in the LysoTracker panels. LysoTracker staining ratios ranged from 1.18-1.45 and 0.85-1.15 in control hermaphrodites (N2E) and females (CF4101), respectively, across multiple experiments (not shown in this figure). Oocyte GFP::RHO-1 aggregates (confirming knockdown) are indicated with white arrows, and only oocytes containing aggregates were selected for calculating lysosome acidification in Figure 5C. Scale bars, 10 μm. (B) GFP::VHA-13 localization (signal skewness) in hermaphrodites (PHX1414) subjected to RNAi for ESCRT subunits, and compared to hermaphrodites and females (PHX1414 and CF4599 respectively). Each data point represents the average of ten skewness values from different regions within the three most proximal oocytes of a single animal. Statistical significance was determined by Mann-Whitney test and the top and bottom rows of significance indicators compare a specific RNAi treatment to hermaphrodite and female animals respectively. P values: $P > 0.05$ = n.s. and ***$P \leq 0.001$. (C) Variability in GFP::VHA-13 localization and lysosome acidification phenotypes for individual PHX1414 animals treated with *vps-54* RNAi. The skewness value for the GFP::VHA-13 signal and LysoTracker staining ratio (proximal oocyte to distal germline) are indicated for each animal. Successful knockdown could not be verified in each animal (since VHA-13 and RHO-1 were both tagged with GFP). Instead, it was done in a parallel experiment with GFP::RHO-1-expressing animals (SA115) in which more than 75% of animals subjected to a specific RNAi treatment, exhibited detectable aggregation (not shown). Scale bars, 10 μm.

Figure S16

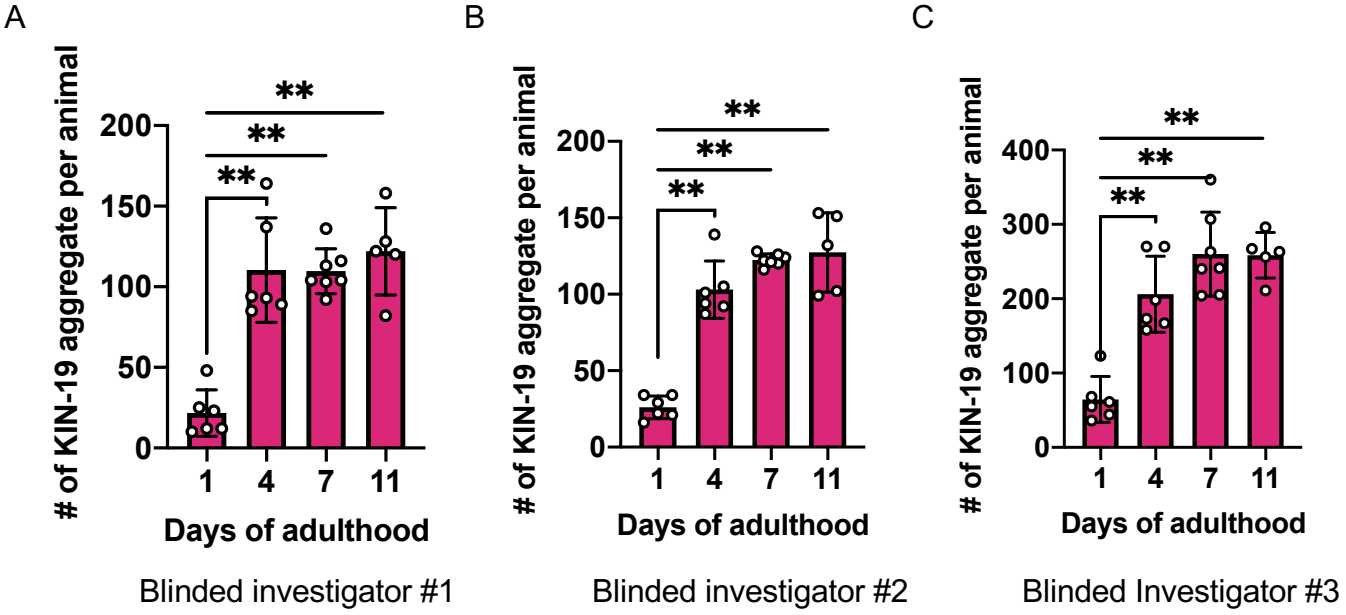
A
B
C
# of KIN-19 aggregate per animal
Days of adulthood
1
4
7
11
**
0
50
100
150
200
300
400
Blinded investigator #1
Blinded investigator #2
Blinded Investigator #3

Figure S16.

Extended data related to Figure 6B.

The same image sets of KIN-19 aggregates used in Figure 6B were scored again, blindly, by three additional investigators (A, B and C). Mann-Whitney test was used to calculate the statistical significance, $^{**}P \leq 0.01$.

Figure S17

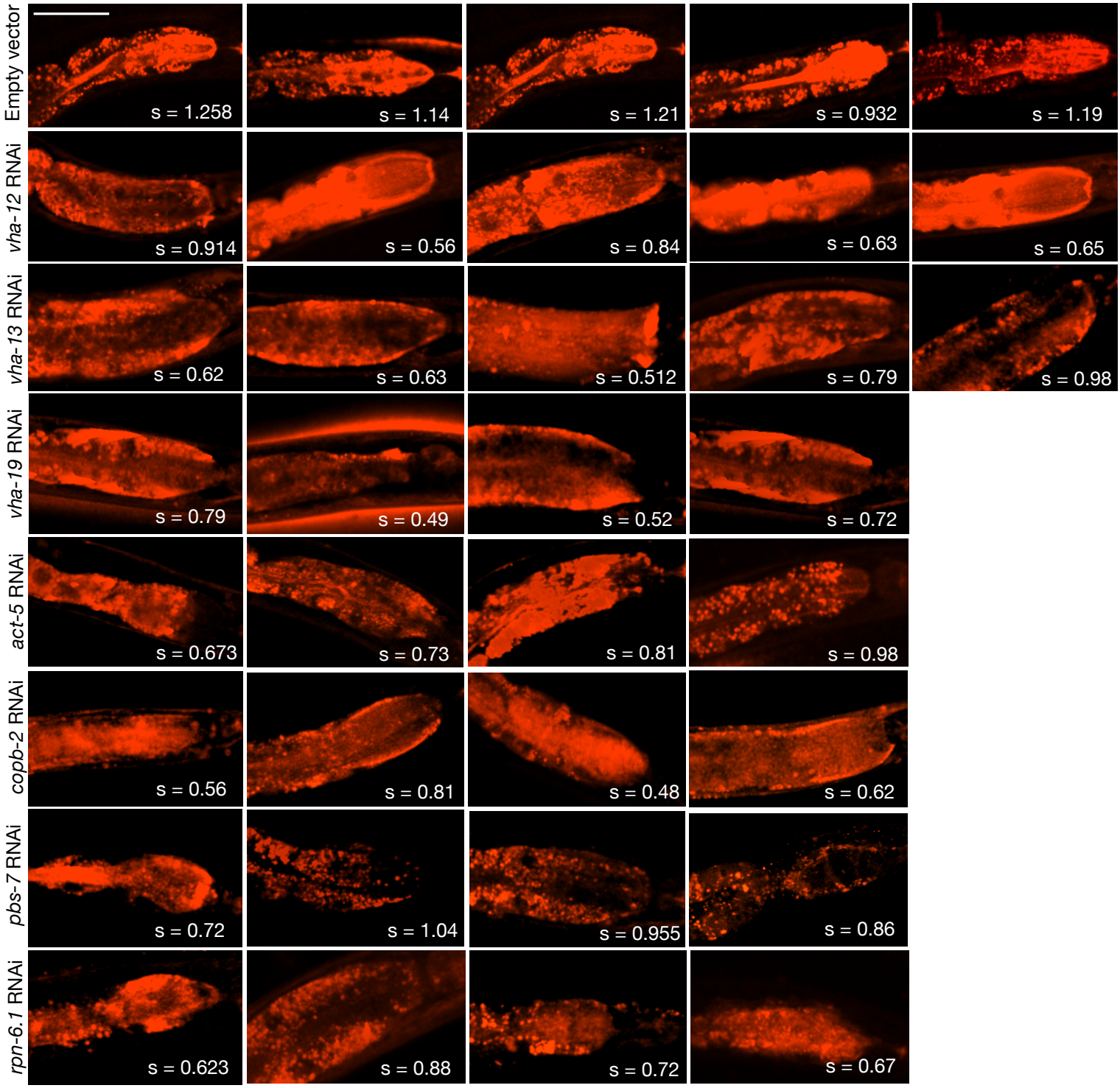
Empty vector
s = 1.258
s = 1.14
s = 1.21
s = 0.932
s = 1.19
vha-12 RNAi
s = 0.914
s = 0.56
s = 0.84
s = 0.63
s = 0.65
vha-13 RNAi
s = 0.62
s = 0.63
s = 0.512
s = 0.79
s = 0.98
vha-19 RNAi
s = 0.79
s = 0.49
s = 0.52
s = 0.72
act-5 RNAi
s = 0.673
s = 0.73
s = 0.81
s = 0.98
copb-2 RNAi
s = 0.56
s = 0.81
s = 0.48
s = 0.62
pbs-7 RNAi
s = 0.72
s = 1.04
s = 0.955
s = 0.86
rpn-6.1 RNAi
s = 0.623
s = 0.88
s = 0.72
s = 0.67

Figure S17.

LysoTracker staining in the intestines of animals subjected to gene knockdowns that caused KIN-19::split-wrmScarlet aggregation in the head. Due to variability in dye uptake and staining, the actual LysoTracker signal intensities within the intestines were not evaluated. Instead, the mean skewness values, s, indicative of inhomogeneity expected for acidic intestinal lysosomes (so-called “lysosome-related organelles”), are reported for each animal (compared in Figure 6E). Skewness values were derived from six different locations within the anterior intestinal region near the pharyngeal bulb. Scale bar, 50 μm.

Figure S18

A

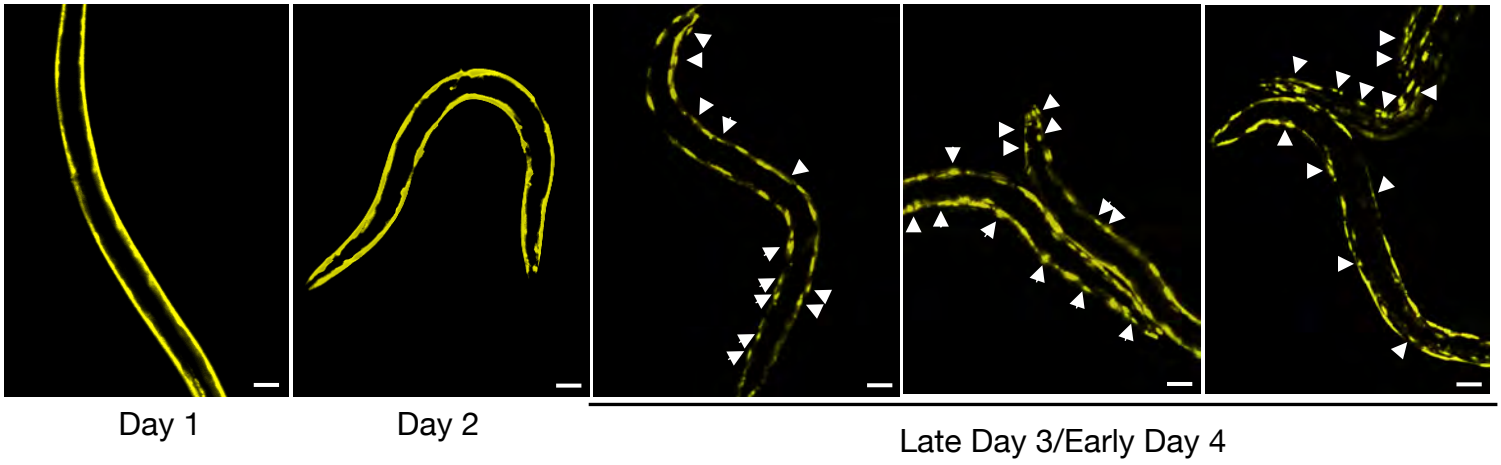

B

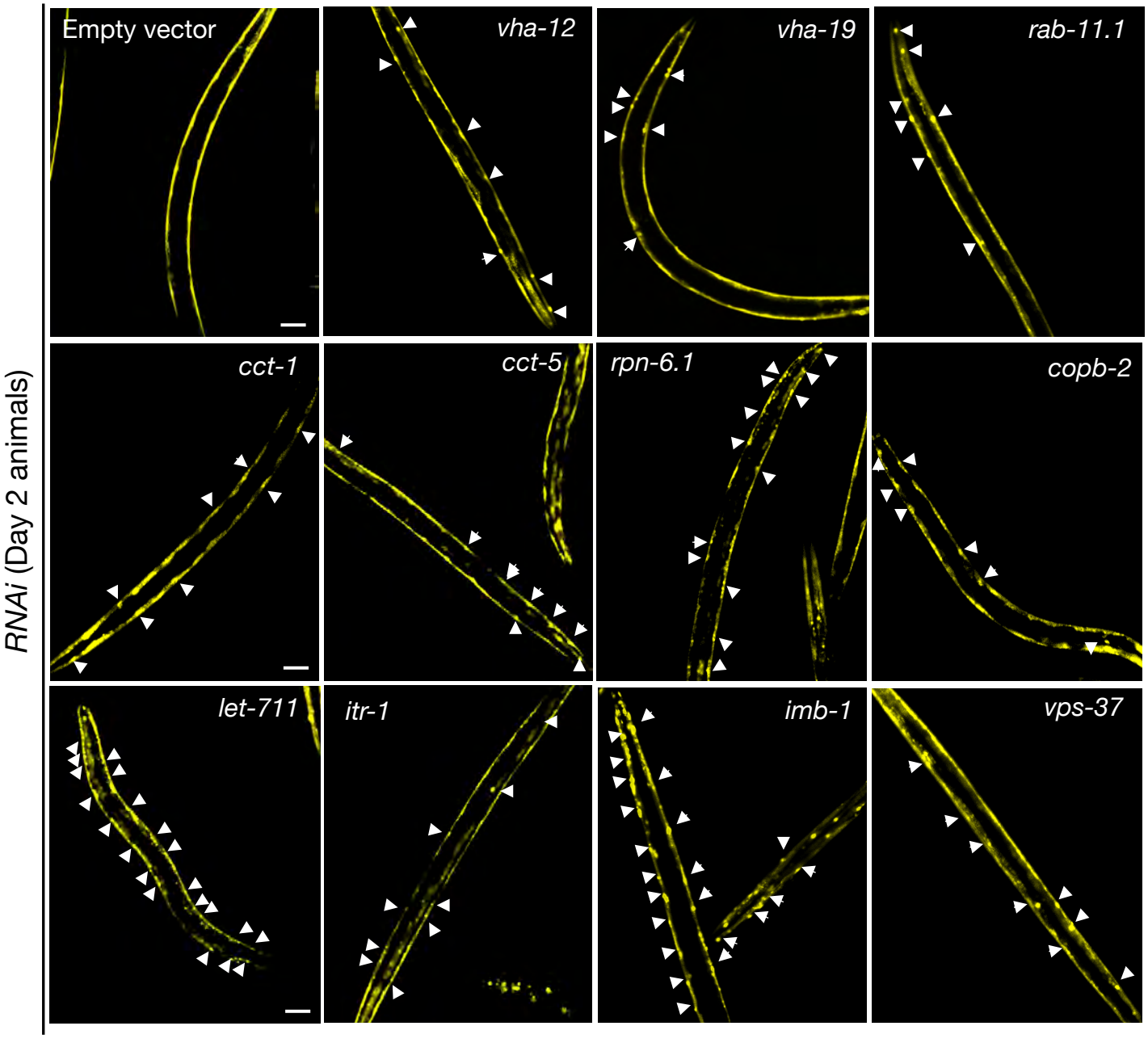

Figure S18.

(A) Representative images of AM140 animals expressing the polyQ reporter, Q35::YFP in body-wall muscle cells imaged at day-1, 2 and 3 of adulthood, with appearance of age-associated aggregates on day-3 of adulthood. (0/8 animals with aggregates were observed on day-2). Scale bars, 50 μm. (B) Q35::YFP aggregates in animals subjected to assay-pool RNAi or empty-vector negative control imaged for the presence of reporter aggregates on day-2 of adulthood. Successful gene knockdown was determined in a parallel experiment with GFP::RHO-1-expressing animals (SA115) subjected to RNAi treatment, and exhibiting aggregation in the germline (not shown). White arrows, representative locations of Q35::YFP aggregates. Scale bars, 50 μm.

Figure S19

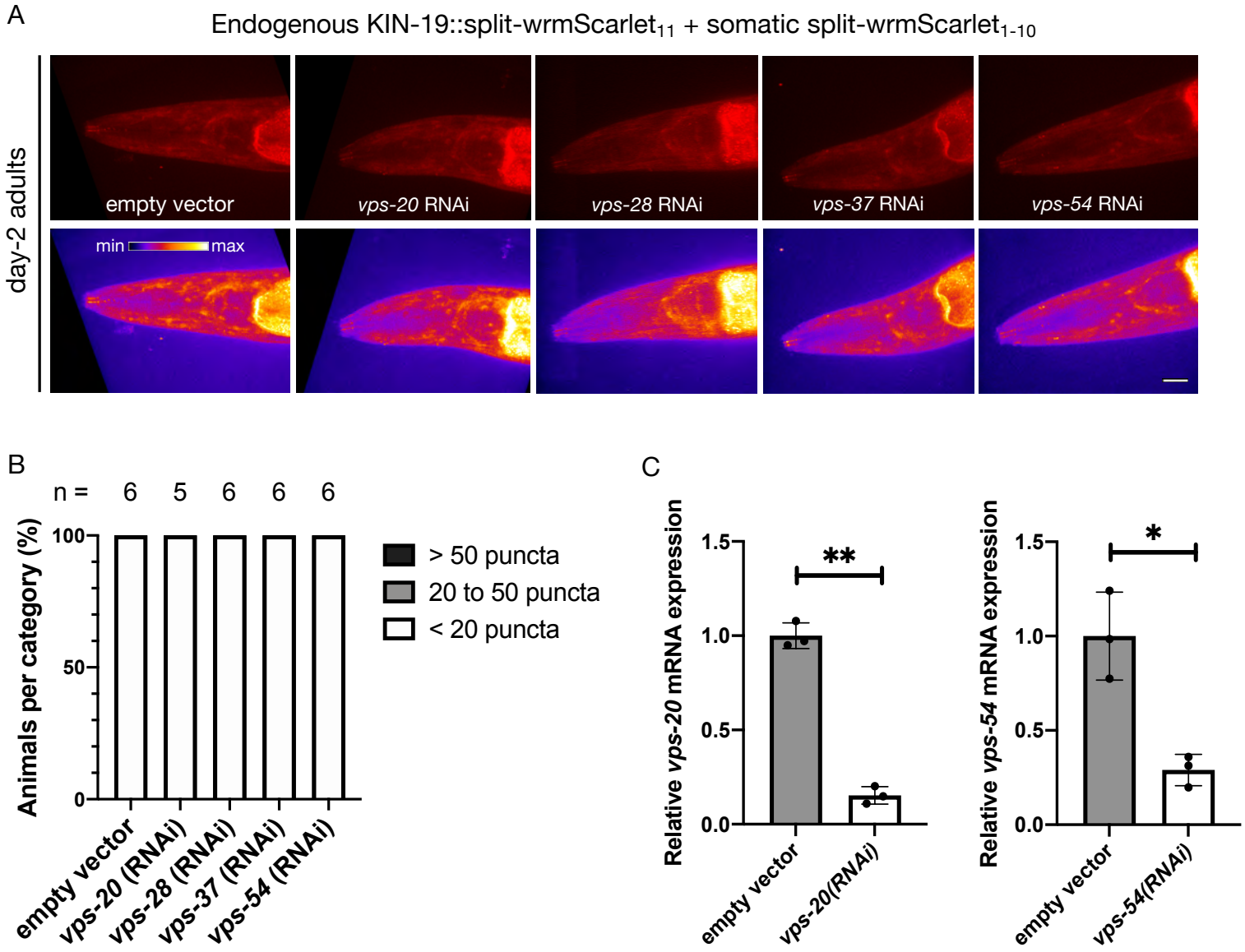
A
Endogenous KIN-19::split-wrmScarlet11 + somatic split-wrmScarlet1-10
day-2 adults
empty vector
vps-20 RNAi
vps-28 RNAi
vps-37 RNAi
vps-54 RNAi
min
max
B
n = 6 5 6 6 6
Animals per category (%)
100
50
0
> 50 puncta
20 to 50 puncta
< 20 puncta
empty vector
vps-20 (RNAi)
vps-28 (RNAi)
vps-37 (RNAi)
vps-54 (RNAi)
C
Relative vps-20 mRNA expression
1.5
1.0
0.5
0.0
**
empty vector
vps-20(RNAi)
Relative vps-54 mRNA expression
1.5
1.0
0.5
0.0
*
empty vector
vps-54(RNAi)

Figure S19

(A) Representative images of CF4609 animals expressing KIN-19::split-wrmScarlet$_{11}$ and somatic split-wrmScarlet$_{1-10}$ subjected to ESCRT-complex RNAi or empty-vector negative control from the L1 stage, imaged for presence of KIN-19::split-wrmScarlet aggregates at day-2 of adulthood. Maximum intensity projections of 3D stacks are shown in red (upper panels), and also using an intensity scale (lower panels). Scale bar, 10 μm. (B) Quantification of fluorescent KIN-19::split-wrmScarlet puncta (only from the head region) in CF4609 animals subjected to RNAi or empty-vector control, using the same scoring method as in Figure 6D. (C) Quantitative RT-PCR analysis of mRNA levels of *vps-20* and *vps-54*, in the set of animals imaged, compared to control empty-vector or treated with *vps-20* or *vps-54* RNAi, respectively. Two-way ANOVA test was used to determine statistical significance; P values; **$P < 0.01$, *$P < 0.05$.

Table S1. Germline proteostasis candidates captured in the screen.

List of candidates obtained from primary screening and validation rounds with GFP::RHO-1. The phenotypic strengths and fertility status are indicated for each. Candidates that were discarded on the basis of their known functions, possible off-target effects, or the failure to pass orthogonal verification with NMY-2::GFP are indicated accordingly.

Table S2. List of *C. elegans* strains

Description of all strains used in the study, including the corresponding genotypes and sources.

Table S3. Candidates from primary screen that did not pass validation

This list is included because some of these candidates could be false negatives, as was the case for the ESCRT-complex genes. Also included are the GO terms (biological process) they represent.